Atom probe tomography

Baptiste Gault[a,b, *], Ann Chiaramonti[c], François Vurpillot[d]

[a] Max-Planck-Institut für Eisenforschung, Max-Planck-Str. 1, 40237 Düsseldorf, Germany.
[b] Department of Materials, Royal School of Mines, Imperial College, Prince Consort Road, London SW7 2BP, United Kingdom.
b.gault@mpie.de | b.gault@imperial.ac.uk **** B. Gault is the corresponding author**
orcid: 0000-0002-4934-0458
[c] National Institute of Standards and Technology, Applied Chemicals and Materials Division, Boulder, CO 80305, United States
chiaramonti@nist.gov
orcid: 0000-0001-9933-3267
[d] Normandie Université, UNIROUEN, INSA Rouen, CNRS, Groupe de Physique des Matériaux, 76000 Rouen, France
francois.vurpillot@univ-rouen.fr

1 General introduction

Atom probe tomography (APT) has been rising in prominence since its inception. APT grew from field-ion microscopy (FIM)[1,2], which was the first technique to allow for directly imaging individual atoms on a surface, as early as the 1950s[3]. In FIM, a high voltage is applied to a specimen shaped as a sharp needle, with an end radius in the range of below 100 nm. This results in an intense electrostatic field which enables two distinct phenomena, field ionisation, which refers to the ionisation of atoms in the vicinity of the specimen's surface, and field evaporation, whereby the atoms from the surface itself self-detach from the surface, desorb and ionise. Following the formation of the ion near the specimen's surface, the ions are projected away from the highly curved surface, and, to paraphrase the inventor of the technique E.W. Müller, the specimen acts as the main projection optic of the entire microscope, which requires no additional lensing system. Müller also pioneered the first design of the so-called atom probe. It combined a FIM with a time-of-flight mass spectrometer[4], which provided the FIM with some capabilities to determine the elemental nature of the imaged atoms on the surface. Early implementations had a small field-of-view, allowing to image and select less than a only a handful of atoms on the surface and analyse them, and through field evaporation of successive layers, compositional depth profiling could be achieved[5].

The implementation of position-sensitive detectors by Cerezo et al. or Blavette et al. in the mid-to-late 1980s[6,7] led to the real breakthrough in instrument design[8,9], providing "three-dimensional" capabilities to atom probes – for historical perspectives, please refer to the thorough reviews in Ref. [10,11]. These new instruments would provide the three-dimensional distribution of each species in a small volume of material, typically of (10 x 10 x 50) nm^3, and used the term "tomographic" even though the analysis is performed point-by-point and not strictly speaking layer-by-layer. Miller in 2000 coined the term atom probe tomography, which is now commonly used – even if there are still remnants across the recent literature of older terms such as three-dimensional atom probe (3DAP), tomographic atom probe(TAP), or even three-dimensional atom probe tomograph (3DAPT).

Today, APT provides compositional mapping with sub-nanometre spatial resolution[12] across a range of mass that spans hydrogen to the heaviest elements [4]. Through successive instrument[13–15] and detector developments [16,17], the analysed volume has been increasing by several orders of magnitude, and, thanks to the implementation of laser-pulsing capabilities [14,18], the range of materials that can be analysed has widened[19]. These novel applications of APT would not have been possible without the development of protocols for the preparation of specimens by using the focused-ion beam (FIB) often in a dual-beam instrument with a scanning-electron microscope (SEM). All these aspects will be detailed in the following sections of this chapter. Information gained from APT is then used to relate the elemental distribution to physical properties, whether to better design novel materials, understand failure, or predict service lifetime.

Thanks to the wider range of materials amenable to APT analysis, the availability of FIBs for specimen preparation, and the higher throughput, the field has expanded. Over 100 commercial instruments have been sold in less than 20 years, and tens of academic and industry research groups are equipped or with direct access to an instrument in one of the several shared use facilities [20]. APT is hence now increasingly being used to provide complementary insights to maybe more conventional materials characterization techniques, such as scanning- and transmission-electron microscopies (SEM, TEM, and STEM) and their derivative including diffraction-based approaches – e.g. selected-area diffraction (SAED), electron backscattered diffraction (EBSD) or transmission Kikuchi diffraction (TKD). On average, APT provides a more precise measurement of the composition than X-ray energy-dispersive spectroscopy (EDS) and is more sensitive – i.e. can detect elements in lower concentration. Its intrinsically three-dimensional nature makes it perfectly suited for the analysis of nanostructured materials, complex semiconductor devices, as well as for the analysis of nanoscale microstructures that would otherwise go undetected by techniques analysing signals based on volume average as secondary-ion mass spectrometry (SIMS) or EDS.

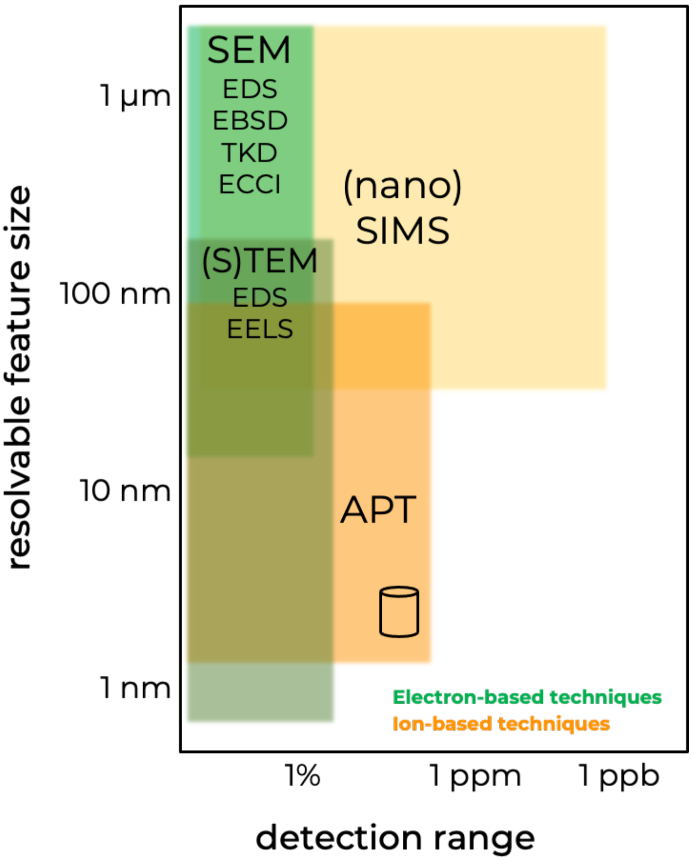

Figure 1: Detection range, i.e. chemical sensitivity, and typical resolvable feature size for selected materials characterization techniques often combined with APT. Note that these are typically electron- or ion-based techniques, as denoted by the different colours. The acronyms correspond to scanning-electron microscopy (SEM), energy-dispersive spectroscopy (EDS), electron backscattered diffraction (EBSD), transmission-Kikuchi diffraction (TKD), (scanning) transmission-electron microscopy ((S)TEM), electron-energy loss spectroscopy (EELS), secondary-ion mass spectrometry (SIMS).

These considerations and complementarities are schematically shown in Figure 1. Although sometimes considered a microscopy technique, APT should likely be considered a spatially resolved mass-spectrometry technique. Conversely to S/TEM for example, the imaging process in APT is only moderately related to the instrument used. The ion optic is the specimen itself, which makes the performance limits both difficult to assess and varying from specimen to specimen, and even over the course of a single experiment. For instance, the spatial resolution is directly related to the distribution of the electric field across length scales ranging from the near-atomic scale to tens of microns or even millimetres, which combined with complex aspects of the field evaporation process that remain still poorly understood, to modify the ion trajectories in unpredictable ways. There are hence no known ways to implement optical devices that may correct or compensate for the aberrations in the ion trajectories that limit APT's spatial resolution.

These aspects will be discussed in detail below in this Chapter. First, let us introduce the instrument itself, the conventional protocols used for the preparation of suitable specimen from a range of materials, discuss the main data reconstruction and extraction approaches, progress in the simulation of the imaging process, and, finally, we will discuss the performance limits and intrinsic limitations of APT. Note that because of the relatively limited progress strictly speaking in the theory of field evaporation, we refer the interested reader to existing review articles [21–23] and textbooks [24–27]. We detail some novel insights into the theoretical aspects in the extensive simulation section below.

2 Instrumentation

2.1 Basic elements

An atom probe microscope is minimally comprised of the following parts: the main experimental chamber, specimen stage (including cryogenic and electronic components), remote electrode, detector, and sets of primary- and turbo- or ion- pumps [4,8,13,28]. FIM microscopes will additionally have a manifold for introduction of the imaging gas [2]. With regards to field-ion microscopes, early designs included a dedicated phosphor screen [2,29], which was later fitted with microchannel plates for amplification [30,31]. FIM can also be performed using the APT detector and recalculated [32–34]. Some instruments are fitted with additional ion-optics, including electrostatic lenses and reflectrons[35–38]. Laser optics are now most often housed inside the main chamber, but in some cases may be placed outside [14,19,39]. Ancillary chambers are often used in order to keep the main chamber as clean as possible and facilitate sample loading, transfer, and storage as well as environmental exposure or reactive atmospheres [40–45]. Recently, various inert atmosphere and cryogenic transfer schemes have been developed in order to facilitate specimen loading and transfer from controlled atmosphere glove boxes, plunge freezing, or cryo-FIB [46–48].

While the exact details of the numerous different configurations of APT and FIM instruments can vary, one thing that they all have in common is that the main experimental chamber housing the specimen is designed to operate under ultrahigh vacuum (UHV) conditions, typically with a base pressure less than 10^{-8} Pa. During FIM operation, the use of an imaging gas increases the pressure to around 10^{-3} Pa - 10^{-5} Pa; the exact pressure depends on whether a phosphor screen or digital particle detector is used. UHV pressures must be maintained during APT experiments to reduce noise in the mass spectral data that comes from unintentional field ionization of residual chamber gas. Since the ionization is due to the static DC standing voltage, it is uncorrelated with the transient voltage or laser trigger pulse and therefore contributes to the time-independent background noise signal. Residual chamber gas and gas adsorbed onto the detector itself can also contribute to noise through ion feedback mechanisms. Finally, another reason that UHV conditions are maintained in the chamber housing the specimen is that since the specimen is held at cryogenic temperatures (typically 25 K to 150 K), it can act as a getter for residual gas and other chamber contaminants. These contaminate the sample, can cause spurious peaks in the mass spectrum, or even potentially change the energetic landscape of the atomic-scale specimen surface.

2.2 Single-particle detectors

The current generation of atom probes uses sophisticated position-sensitive single particle delay line detector (DLD) to simultaneously provide 2D position and TOF information [49,50]. A DLD typically consists of a multi-channel plate (MCP) assembly combined with impedance-matched serpentine delay line anodes (DLA) mounted orthogonal to each other.

An MCP is a charge-to-electron conversion system that is made from a thin insulating plate perforated with a close packed array of small (~ 10 um diameter) tubular microchannels whose inner surface has a high secondary electron yield. MCPs are effectively insensitive to the type or chemical identity of the of incoming particle long as the energy is above ~ 1 keV to 2 keV. In this case, the electron conversion efficiency is dependent only on the bias between the two faces of the MCP plate. Two MCPs mounted back-to-back in a chevron configuration are used in order to increase the signal pulse. Ions hit the active area (the microchannels, or pores) of the MCP and initiate a secondary electron cascade signal pulse on the order of 10^6 electrons/ion with a ~ 5 ns duration. The electron cascade reaches the DLA, and the x,y position of the "hit" can be triangulated based on the propagation time of the signal to the ends of the delay line(s). The signal from the DLA is captured by constant fraction discriminators and digitized. This is sometimes also referred to as a CDL detector or crossed delay line detector. Often, a third wire is mounted at a 60° or 45° angle; three anodes are used for redundancy and to improve multiple hit performance [50].

The detection efficiency of the MCP array is limited primarily by the open pore area and the angle of incidence. The active area on a commercial straight flight path instrument is nominally 75 mm, and the detector efficiency is in the range of ~ 50 % to ~ 80 %. Instruments equipped with electrostatic energy compensation devices (e.g. reflectrons) have a limited acceptance angle due to the field-defining mesh at the entrance/exit to the energy-compensating reflectron lens and the detector has a smaller active area of nominally 37 mm. These instruments reach up to about 50 % detector efficiency.

The performance of the detector (and hence, the atom probe itself) can be described in terms of its time and spatial resolution, both of which derive from the ability of the DLD to extract precise timing information from an analog signal. Spatial resolution is generally very good due to the inherent "center of gravity" averaging of the electron cascade signal pulse created in the MCP stack as well as the fine winding of the anode wires. Position resolution below 50 µm (on the detector itself) has been reported [50]. Time resolution is typically under 50 ps. With magnifications of the point projection on the order of 10^6, the spatial resolution achievable in an atom probe reconstruction 3D image is therefore in the sub-nm range in *x,y*.

There are some drawbacks to DLD detectors, particularly for the quantification of multiple hits and resolving isobaric overlaps. A DLD will have an electronic deadtime due to the inability to deconvolute overlapping signals on the delay lines [49]. The electronic deadtime depends on the exact details of the detector and is on the order of 3 ns with partial loss of information extending slightly beyond that [51,52]. This means that during this dead time window after an ion hit, additional ion impacts cannot be registered if they arrive at the same location. However, the signal can be recovered if the second ion hit is sufficiently separated in distance on the detector. The dead time is better described as a dead zone. Within the detector dead zone, additional ions cannot be detected within the dead time. Thus, the signal from multiple hits can often be recovered as long as the ions do not arrive at the same position and at the same time.

Another drawback to the DLD detector is the inability to measure the kinetic energy of an ion, which would allow for the discrimination of isobaric overlaps. Isobaric overlaps (e.g. $^{54}Fe^{+}$ and ^{54}Cr, $^{28}Si^{2+}$ and $^{14}N^{+}$, $^{16}O^{+}$ and $^{16}O_2^{2+}$) occur when two ions have nearly or exactly the same mass-to-charge-state ratio. In the case of $^{54}Fe^{+}$ and ^{54}Cr almost two orders of magnitude increase in mass resolution would be required to resolve the peaks, which is not physically possible without sacrificing efficiency or field of view (FOV) [53]. In some cases, isotopic ratios can be used to infer the relative contribution of the species. However, this method must be used with care. In elements that tend to multi-hit (e.g. B, C), or under experimental conditions where multiple counts are high, the most common isotope of an element can be significantly undercounted [51] and the method may lead to error in measured composition. There are some cases, like $^{28}Si^{2+}$ and $^{14}N^{+}$, where isotopic ratios cannot be used because neither element has isotopes in sufficient number to enable a robust deconvolution.

Kinetic-Energy discriminating position sensitive single particle detectors would in principle solve some isobaric overlap problems [54]. Besides being able to distinguish ions with isobaric overlap, they would also allow filtering of ions that evaporate with the voltage pulse versus those that evaporate from the DC standing voltage or random field ionization. Ions such as $^{16}O^{+}$ and $^{16}O_2^{2+}$, which overlap at 16 Da, could be distinguished based on their kinetic energy. Several potential detector technologies were suggested in 2011 including alternative electron-multipliers and superconducting delay line detectors [54,55]. This is currently an active area of research and the first proof of concept experimental results on a position-energy sensitive detector based on a carbon foil ion-induced secondary electron emission mechanism have been demonstrated [56].

2.3 Counter-electrodes

The most common commercial atom probe microscope as of this writing uses a ~ 40 µm diameter conical-shaped counter electrode (CE) placed within about one aperture diameter of the specimen apex. While in principle the detector itself could serve as the cathode, in practice this is never done. This design concept was introduced by Nishikawa et al. [57], and further developed by Cerezo et al. [58], before being commercialised as the local-electrode atom probe under the leadership of Kelly et al. [13].

This “local electrode” serves several purposes. First, it significantly enhances the field at the specimen apex thereby decreasing the voltage required to achieve the surface field necessary to trigger field ion evaporation by approximately half as compared to traditional FIM or 3DAP instruments [27]. Both the accelerating distance and accelerating time of the ion are significantly shorter in the presence of an LE, thus reducing dynamic contributions due to the time varying field in voltage mode [59]. The LE also allows for the use of shorter, larger radius specimens and multiple specimen arrays as compared to a remote, planar electrode. Thus, the FOV is greatly increased. The specimen array is mounted on a stage, and if an individual specimen fractures, one can simply translate quickly over to the next one rather than having to load a new sample. In voltage pulsing mode, the specimen remains at ground potential and a negative electrical pulse is applied to the LE to trigger ion emission. In laser pulsing mode, the LE is held at ground potential relative to a positively biased specimen. There is also an additional post-acceleration voltage applied between the grounded LE and the detector in laser pulsed instruments and the overall applied voltage is the sum of these two [60]. The newest commercial atom probe instruments use a planar electrode with an aperture placed close to the specimen apex. They help contribute to a wider FOV, but the downside is that only single specimen needles can be used.

2.4 Pulsing modes

Field evaporation can be triggered by voltage pulsing, laser pulsing, or by combining the two. Voltage pulsing works by modulating (increasing) the applied surface field, which decreases the activation energy barrier to field ion emission. The sample must be of sufficient conductivity to transmit the field to the specimen apex and in practice this limits its use to metals and some semiconductors. In a voltage pulsing experiment, the sample is held at a constant standing (DC) voltage, and a high voltage pulse is superimposed at a frequency between 25 kHz and 200 kHz. The pulse fraction, defined as the percent increase above the DC standing voltage, is typically in the range of 10 % to 30 %. High amplitude solid state pulse generators are used to ensure a rise time of less than 1 ns and a very narrow pulse width [60], which minimizes energy deficits and the increases mass resolving power of the instrument.

Laser pulsing, at least in the visible and near ultraviolet (NUV) regimes, is generally accepted to work through a bulk heating mechanism. It can be applied successfully to a wide variety of materials including metals, semiconductors, insulators, organic and biological materials, and even water ice. Early attempts (1976-1984) at integrating pulsed lasers into FIM and atom probe instruments were met with limited success [61–63] due to the reliability and cost of the pulsed lasers available at the time. In the early 2000s, the technology had improved and several groups again pursued the idea of laser pulsing for atom probe [14,18,64,65]. Initially pulsed lasers with fundamental frequencies in the near infrared (NIR; 1064 nm < λ < 780 nm) were used. These were then frequency doubled and tripled into the visible (515 nm < λ < 532 nm) and near ultraviolet range (343 nm < λ < 355 nm), as it was observed that the variety of materials to be analysed, the quality of APT data, and the specimen survivability increased as the wavelength decreased. The newest commercial atom probe instruments use the 4th harmonic of a 1028 nm fundamental and operate in the deep ultraviolet regime (λ = 257 nm) [66].

While the near ultraviolet instruments are currently the most numerous and deep ultraviolet are steadily increasing in number, several groups have developed instruments operating well outside this range. In 2019 a wavelength-tuneable femtosecond pulsed coherent extreme ultraviolet (EUV) microscope was developed [67,68]. The mechanism for generation of the EUV pulse is through high harmonic generation in a noble gas-filled capillary [69]. This atom probe operates with < 10 fs pulse duration and wavelengths discretely tuneable in the range of ~ 28 nm < λ < ~ 50 nm. Wavelengths in this range ensure higher and more uniform absorption across the periodic table and open the potential to photoionization-based ion emission mechanisms.

A terahertz-driven atom probe [70] was recently developed. In this microscope, ultrashort terahertz pulses generated from a two-colour air plasma are focused on metallic samples and trigger field ion emission through the generation of extremely localized, high-intensity electric fields at the specimen apex. A NIR (800 nm, 45 fs) pulse can be combined with the terahertz pulse and colinearly focused on the sample with a variable time delay in order to probe the dynamics and mechanism. This dual-frequency excitation provided experimental evidence that field ion emission the terahertz regime proceeds through an athermal ionization and desorption mechanism.

2.5 Ion optics

Although an atom probe microscope is a point-projection microscope where the specimen itself serves as the main ion optic, additional lenses or optics are sometimes used to enhance the performance in various ways. The most widely used ion optic in APT is the reflectron [Mamyrin Sov. Phys. JETP 37 1973, Drachsel J Phys Colloques 50 C8 1989, Cerezo Rev Sci Inst 69 1998, Payani UK Patent 050963.8 US 60/682,863]. In voltage mode, the reflectron is used to compensate for the facts that the voltage pulse is not a perfect delta function and ion emission is a probabilistic process. Ions depart the surface at slightly different times and therefore have small differences in their kinetic energy. This leads to so-called tails in the mass spectrum histogram that are the result of the initial energy spread and manifest on the high m/q side of a mass peak. These degrade the mass resolving power of the instrument.

The reflectron is an electrostatic device that acts as a spherical mirror for ions and works by focusing the ions in time. It is comprised of two concentric spherical electrodes defined by a high-transparency mesh at the entrance and exit that serve as electrostatic ground. Ions with a given m/q entering the reflectron see an increasing field and are initially retarded, reflected, and then accelerated out again. Less energetic ions are deflected first, experience a shorter total flight path, and exit first. More energetic ions penetrate further into the field before deflection. Their flight path is effectively lengthened, and the result is that both ions arrive at the detector at the same time. This curved spherical electrode design also compensates for so-called chromatic aberration. Ions entering the reflectron with the same angle but slight differences in energy are focused spatially on the detector. In laser-pulsed mode the energy spread of the ions is governed by the energy spread intrinsic to the complex field evaporation process and not by the thermal energy of the emitted ions [Larson book]. However, by significantly increasing the length of the flight path the reflectron also increases the mass resolving power in this mode as well. There are trade-offs, however, as instruments with a reflectron have a more complicated reconstruction process and decreased detection efficiency due to the presence of the high-transparency mesh. Another drawback is that correlation histograms cannot be used to study molecular dissociations since any energy discrepancies between daughter ions would be compensated by the change in flight path length [Saxey Ultramicroscopy 111 2011].

Another ion optic employed in atom probe tomography is the Einzel lens. It is an electrostatic lens that focuses charged particles without changing their energy. Three individual electrostatic elements make up a “single” Einzel lens, with a geometry consisting of either a series of three coaxial cylinders or concentric apertures. The first and last electrode are typically held at the same potential and focusing is achieved by varying the potential of the center electrode. Electrostatic Einzel lenses have been historically used in APT to time- and spatially-focus ions in both straight flight path and toroidal sector energy compensated 1-D instruments [Cerezo Surf Sci 246 1991]. In the straight flight path case several geometrical designs of a single Einzel lens were evaluated resulting in varying degrees of focusing power depending on how far the lens was placed from the specimen object. For instruments with toroidal energy compensation, the Einzel lens improved the time focusing of a sub-optimally aligned toroidal sector, but the spatial focusing was degraded. For a well aligned energy compensator, time resolution was degraded.

Recently, the Einzel lens has made a resurgence, and the newest commercial 3D instruments employ advanced ion optics including multiple Einzel lenses that increase the FOV substantially over previous instruments [Y. Chen et al. Microsc Microanal 29 S1 2023]. For an Al 6062 alloy tip the FOV was increased from approximately 60° to nominally 90° as measured using the Al crystallographic poles present in the field of view [Tegg Ultramicroscopy 253 2023]. When this alloy specimen was run sequentially in a conventional straight flight path instrument and then transferred via vacuum to an instrument with advanced ion optics, the diameter of the specimen in the FOV increased by a factor of two and the cross-sectional area increased by a factor of 4. The increased FOV does come at a price, however. Spatial distortions resulting from chromatic aberration altered the shape of the β” precipitates in Al 2026 and were primarily observed on the outer edges of the reconstruction with the wider FOV.

2.6 And beyond…

As emphasized in Figure 1, the capabilities of APT overlap in spatial resolution and analytical sensitivity with other nanoscale characterization techniques while offering many unique benefits. Combining these techniques into a single instrument would provide many advantages. One benefit is the possibility of achieving the lofty goal of so-called atomic scale analytical tomography [71,72] which is where the chemical (indeed, isotopic) identity and spatial location of every atom in a specimen is known with a high degree of certainty.

A combined APT/spherical aberration-corrected scanning transmission electron microscope (STEM) was designed and is expected to be installed at the Ernst Ruska Centre in Jülich in 2025 [73,74]. The STEM provides pm spatial resolution, diffraction/crystallographic information, access to bonding information through electron energy loss, accurate measurement of the specimen apex radius and shape over time, and direct mapping of the electrostatic field surrounding the specimen apex through use of electron holography or differential phase contrast methods. The APT will provide unrivalled spatially resolved analytical sensitivity to every isotope in the periodic table.

In another example of functional integration, a modular APT-FIB/SEM has been developed [75] that provides fast and direct specimen transfer with capability for flexible chamber component design. Such an instrument enables new specimen geometry configurations as well as the capability for direct transfer of cryo-FIB prepared specimens, negating the need for expensive proprietary ancillary vacuum/cryo transfer equipment on both the FIB/SEM and APT. It also facilitates the preparation and examination of air-sensitive samples such as battery materials.

There are also a flurry of other singular instruments, with e.g. spectroscopic capabilities [76], or chambers made of Ti-based materials targeting analysis of hydrogen [77] along with those with deposition or gas-charging capabilities [41,78,79]. And we invite the interested reader to consult these articles directly.

3 Specimen preparation

As for most microscopy techniques, the first step in performing APT is the preparation of specimens suitable for examination. The primary requirement for a specimen is that it must be shaped as a sharp needle with a circular cross-section. How sharp depends on the material and the instrument. With the evaporation field of most species in the range of 10 V·nm^{-1}–60 V·nm^{-1}, and power supplies on atom probes limited to 12 kV–15 kV, the specimen's end radius must typically be in the range of 20 nm–100 nm. During the analysis, the specimen is eroded, and hence the end of the specimen progressively blunts – i.e. the radius of curvature increases. To compensate for this, the high voltage is increased at a rate that depends on the shank angle. Ideally, the shank angle should be low – approximately 5˚ or less. However, in laser-pulsing mode, the shank angle also influences heat transfer and therefore the achievable mass resolution. For this reason, it may need to be maintained higher (above 15˚). The surface along the shank should be as smooth as possible. Asperities can lead to stress concentration and increased fragility. Finally, the preparation protocol should not lead to additional undesired or uncontrolled microstructural modification or introduction of foreign species and should leave the specimens in a state suitable for being introduced in the ultra-high vacuum chamber of the atom probe. These considerations are illustrated in the image of a pure-Al specimen, prepared by electrochemical polishing, and imaged by transmission-electron microscopy, displayed in Figure 2a. It should be kept in mind that the field-of-view (FOV) of the resulting APT data varies with the specimen radius through the magnification[80,81] and depends on the diameter of the active area of the detector, the effective specimen-to-detector distance, and the trajectories of the ions.

Specimens for APT have historically been prepared by using electrochemical polishing, using a range of solutions or molten salts depending on the material of interest. These will be discussed in the following. Electrochemical polishing works very well for metals and is still routinely being used for APT specimen preparation of bulk specimens. However, SEMs equipped with a FIB have proved more versatile even for metals, where particular microstructural features or phases can be intentionally targeted. These microscopes are also superior for the preparation of non-metallic samples and are routinely used for the preparation of specimens from a wide range of materials systems. Alternative approaches involving for instance a broad ion beam, laser, or mechanical polishing have also been proposed, and will be briefly discussed in the following. The most recent developments in the preparation of specimens at low temperature will also be discussed. Finally, we will discuss complete specimen preparation and imaging workflows, involving multiple microscopy techniques correlated together.

3.1 From bulk materials

3.1.1 Electrochemical polishing

There have been many extensive reviews and book chapters on the preparation of APT specimens by electrochemical polishing, and we will herein simply brush over the main principles. We invite the interested reader to refer to the books by Miller et al. for instance[27,82], and will only provide here some general aspects of the methodology.

First, for preparing specimens from bulk metallic materials, a small match-stick-shaped blank is first cut with electric-discharge machining (EDM) or a saw. The dimensions are typically 400 µm–600 µm in length with a square cross section. If the material is already available in wire form, this step can be skipped. To turn the blank into a needle as required to perform atom probe, it is dipped into a beaker containing a counter electrode and an electrochemical etching solution. It is repeatedly dipped either manually or via a lift stand until it gets sufficiently sharp – in the range of a micron or so at the apex. The solution and voltage applied between the blank and the counter-electrode located in the solution depends on the material to be electropolished. The use of various alkaline or acidic solutions have been reported [82,83]. To obtain two separate needles from a single blank, a heavy and inert solvent was sometimes placed at the bottom of the beaker and the active solution was placed on top – this approach is called the double layer. For noble metals, molten salts at higher temperature were used [82].

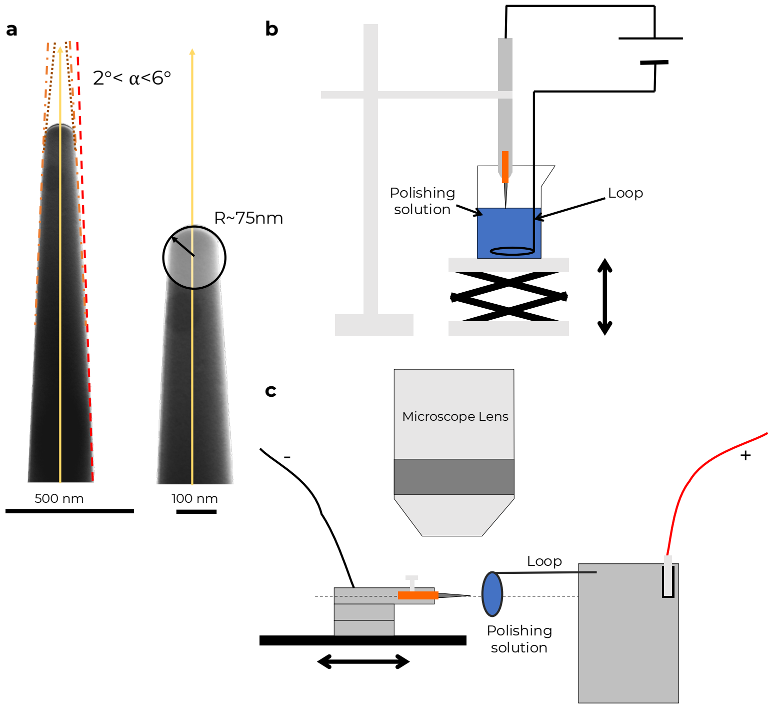

*Figure 2: **a** Transmission-electron (TEM) micrographs of a single, electropolished pure-Al specimen at two magnifications highlighting the smooth exterior surface, the low shank angle, and the small radius of curvature. **b** and **c** are schematics of the rough and fine electropolishing rigs, respectively.*

To finalise the specimen, the roughly sharpened blank is typically moved through a thin layer of a solution (often similar but with a different concentration of the active components) held by a loop located under an optical or a binocular microscope. The loop acts as counter electrode. The solution voltage applied depends on the considered material. There are multiple approaches, depending on the material: either by a progressive thinning of the specimen's the cross section until it is sufficiently sharp, or the creation of a neck as a certain distance from the apex i.e. by having the tip of the needle through the entire droplet and electropolishing along the shank of the needle. By thinning down this neck to the point of rupture, a single needle can be made typically with dimensions in the required range. The length of the neck and the rate at which the electropolishing is performed can help control the specimen's shank angle.

Using electrochemical polishing for the preparation of APT specimens suffer from a range of limitations: materials containing multiple phases can be subject to preferential polishing of one or more of these phases, leading to uneven surfaces and specimen shapes that will lead to reduced yield; there is a need for the material to be electroconductive, limiting the application of the approach for the preparation of e.g. semiconductors or insulators; the analysis of specific microstructural features, e.g. a grain or a phase boundary requires that it is placed within the first 100 nm form the tip of the needle-shaped specimen, which remains challenging by electrochemical polishing and often requires sequential use of TEM and pulsed electrochemical polishing [84–86]; finally, the analysis of thin films deposited on a flat substrate is extremely challenging through electrochemical polishing.

3.1.2 Focused-ion beam milling

These limitations have been addressed – at least for the most part – by the use of dual-beam SEM/FIB systems for the preparation of APT specimens. FIBs most often include a liquid metal gallium source, with an increase in the availability of plasma-based sources in recent years [87–90]. With the preparation taking place inside an SEM, complementary microstructural information about the sample can be gathered by using electron imaging, including backscattered imaging or electron-channelling contrast imaging (ECCI) [91] along with electron backscattered diffraction (EBSD) [92,93]. This allows for the preparation of specimens from selected regions-of-interest. Following the pioneering work of Larson et al. [94,95], various workflows have been introduced over the past 20 years for the preparation of individual or series of specimens [96–98], with the protocol detailed by Thompson et al. having become a *de facto* prevailing route for specimen preparation [99]. This protocol is schematically depicted in Figure 3: (1) a wedge-shaped cantilever is first cut from three sides, it is 15 µm–20 µm long and 3 µm wide; (2) the micromanipulator is inserted and brought in contact with the end of the cantilever, and the gas-injection system (GIS) is used to weld, in situ, the micromanipulator to the cantilever by depositing a metal-carbon composite; the cantilever is subsequently cut free and the stage is lowered; (3) the cantilever is brought in contact with a support, welded with the same metal-carbon composite from the GIS, and sliced; (4) lastly, the slice is subjected to annular milling to turn it into a sharp needle suitable for APT analysis. The final specimen milling is performed with ions a low acceleration voltage of 2 kV–5 kV, which helps remove the subsurface regions of the specimen that have been severely damaged by the incoming high-energy ions [99].

Note that the composite deposited by the GIS is most often Pt-based but can also sometimes be W-based. It is believed that the deposition occurs primarily from the secondary electrons emitted by the surface that break the metal-containing organic precursor [100]. Deposition can hence be done by using either the electron beam or the ion beam, with the former leading to denser metal deposits. This metal-composite is also often deposited on the region of interest before the lift-out is performed in order to protect the surface from the incoming beam of energetic ions that are known to cause structural damage from the implantation of heavy ions [100]. Computation through e.g. the Stopping Range of Ions in Matter (SRIM) [101] can provide indication of the depth of material affects. The nature damage will depend on the target material as well the nature and energy of the incoming ions. Xe-PFIBs are sometimes expected to cause damage more confined to the surface than Ga, but gas-bubbles can be observed to form [87]. Ga is a reactive metal that is known to embrittle several metallic materials and particularly aluminium and its alloys [102]. Xe is inert and has enabled site specific preparation of specimens from several Al-alloys [103–105].

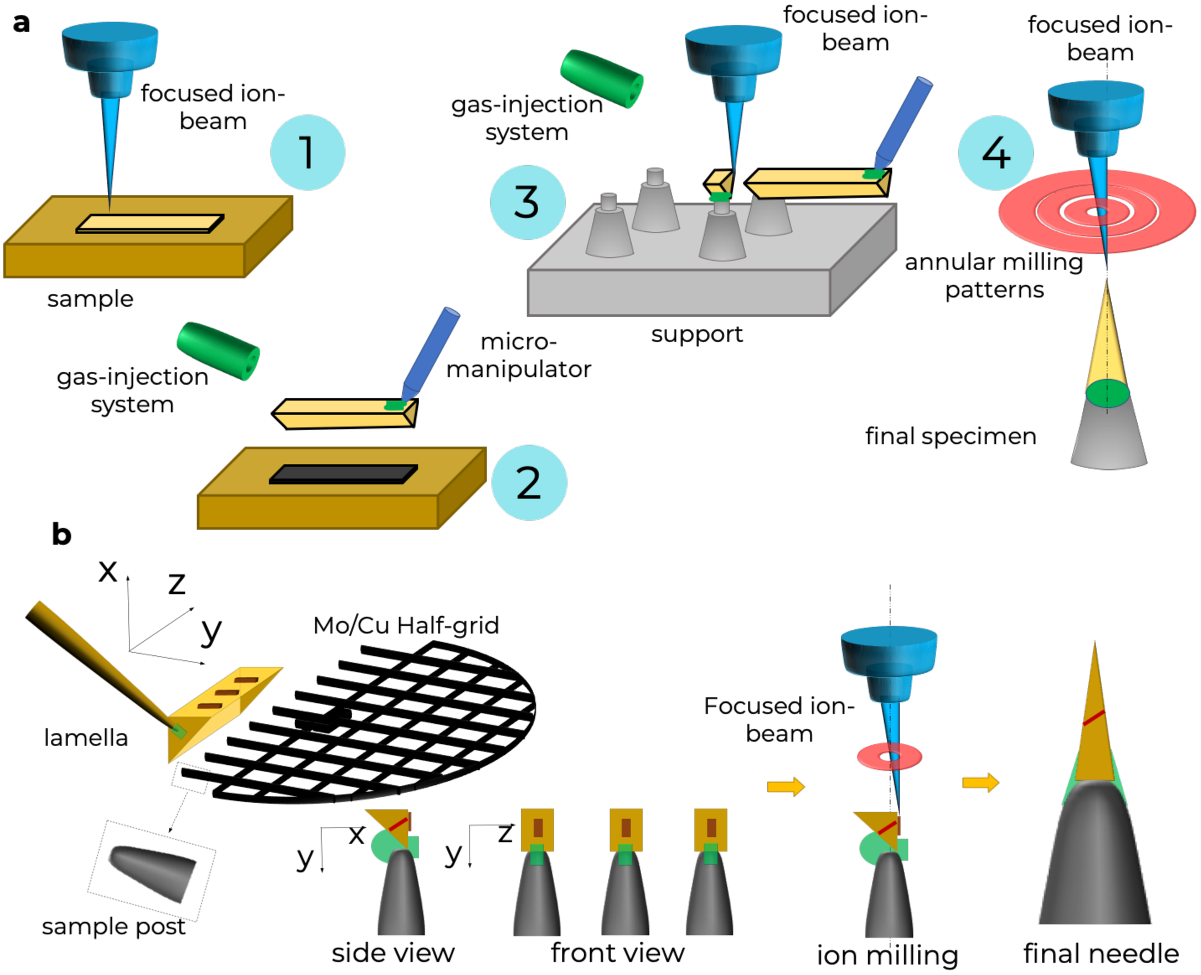

*Figure 3: **FIB-lift-out specimen preparation: a** Four-step protocol for FIB lift-out based specimen preparation deposited on a support. **b** Protocol adapted for in-plane lift-out of targeted features to facilitate correlative analysis by transmission electron microscopy.*

3.1.3 Alternative approaches

There have been attempts in the past decade to explore alternative routes for specimen preparation. For instance, Halpin et al. [90] made use of the higher currents offered by Xe-PFIBs to revisit the possibility of using a moat approach [97], whereby a large volume of material is removed around a pillar that is finally turned into a sharp needle. This has successfully been used for analysing Ti-alloys as well as Al-alloys, including for site-specific analysis [106].

The use of FIBs has a number of drawbacks, in particular the unavoidable damage from the ion beam and the reactivity of the Ga. For instance, there have been reports of using broad Ar+-beam milling and using beads or masks to locally change the sputter yield and leave tips standing out [107,108]. Laser-beams for ablation of the surface have also been used, primarily to prepare pre-shapes that will accelerate the fabrication of specimens by FIB afterwards either in a standalone laser-instrument [109] or as part of three-beam systems. In a three-beam system, a laser is attached to a SEM/FIB for ablating large material volume [110] and can facilitate the preparation of multiple specimens from a flat substrate akin to the microtip coupons used for lift out support [111,112]. These could facilitate high throughput specimen preparation, provided that the heat-affected zone is not interfering with the region of interest targeted for the analysis. Finally, high-precision mechanical polishing has also been proposed as an alternative method [113], but the limited reports on this approach hinders establishing an accurate perspective on its usefulness.

3.2 From nanostructures

Since the early days of the atom probe there has been a vivid interest in using it to probe the chemistry of reactive surfaces, in particular catalysts, since the end of the specimen could be considered as an individual nanoparticle [114]. Beyond these applications, using APT to analyse active nanoparticles or other nanoscale materials such as nanosheets or nanowires has required targeted strategies for specimen preparation [115]. For instance, nanoparticles have been deposited onto sharp needles through electrophoresis in solution[116,117], but the uneven coverage and relatively weak strength of the bond to the substrate limits the yield. Single or agglomerated nanoparticles or nanowires can be picked and deposited directly onto the support using a micromanipulator or a microgripper [118–120].

Drop casting nanoparticles on a substrate and then covering them by a thin layer of metal or metal-carbon composite in the FIB [115,120] allows for subsequently using a standard FIB lift-out protocol. The protective metal film (e.g. Cr, Pt) assists with the adhesion of the articles during preparation and analysis[118,121] and helps prevent damage from the incoming Ga-ion beam.

Kim et al. proposed to embed nanoparticles in an electrodeposited metallic matrix and then prepare specimens by FIB lift-out [122]. This approach was successfully used to analyse a range of nanoparticles, nano aerogels, nanowires, and nanosheets [123–129]. This methodology avoids issues with films from sputtering or electron-beam deposition that are non-conformal and often contain voids at the nanoparticle-substrate interface that lead to trajectory aberrations [130] and limit the yield. Larson *et al.*[130] achieved similar results by using atomic layer deposition (ALD) to produce a void-free and highly conformal coating over assemblies of nanoparticles from which a lift-out was performed to prepare specimens. This alleviates possible issues with the solution and potentials used for electrodeposition, which can react with the nanoparticles' surface or cause corrosion. An added benefit is that the composition of the metallic matrix is often simple, leading to fewer peaks in the analysis of the matrix itself compared to most oxides. The solution and film composition can also be adjusted to have an evaporation field close to that of the particles of interest to limit aberrations in the data.

3.3 Correlative approaches

The main differences between the workflows in Figure 3 a and 3b is the support, which is either a commercial microtip coupon [131] or a pre-sharpened half TEM-grid [132,133]. For this latter case, a specific microstructural feature identified by SEM was marked by using the GIS, in order to keep track of its location over the entire specimen preparation process and ensure that it is present in the final specimen [91]. The key interest of using a TEM-type grid as support is that it facilitates observations of the specimen in the TEM prior to APT analysis. Ever since the early days of FIM and APT, the compatibility and complimentary nature of TEM has been highlighted and exploited [134]; APT samples are usually small (thin) enough to be electron transparent for most materials at commonly used accelerating voltages. Even if some partial crystallographic information can sometimes be extracted and exploited [135], the spatial resolution of APT [12,136,137] does not generally allow for studying the crystal structure or orientation. This information is accessible through TEM.

Figure 4, from the perspective article by Herbig [138], showcases various electron imaging modes along with the use of energy-dispersive X-ray spectroscopy (EDS) directly on APT specimens. This reveals grain structures, various precipitates and defects, and the atomic organisation at atomic-column resolution. This form of correlative electron microscopy with APT provides a comprehensive set of microstructural information including structure and composition from the same region-of-interest. Over the past decade, numerous examples of application of this TEM-APT approach have been reported in metallic systems [139–143], semiconductors [144,145], and oxides [146]. Note that during electron imaging, particularly in STEM because of the highly focused beam, carbon-containing species normally deposit on the specimen's surface and prior to APT analysis the surface must be cleaned: either in the FIB by using low acceleration (2 kV – 5 kV) ion milling or by using the a low-energy, broad ion milling system [147]. This cleaning step was reported to increase the success rate and data quality.

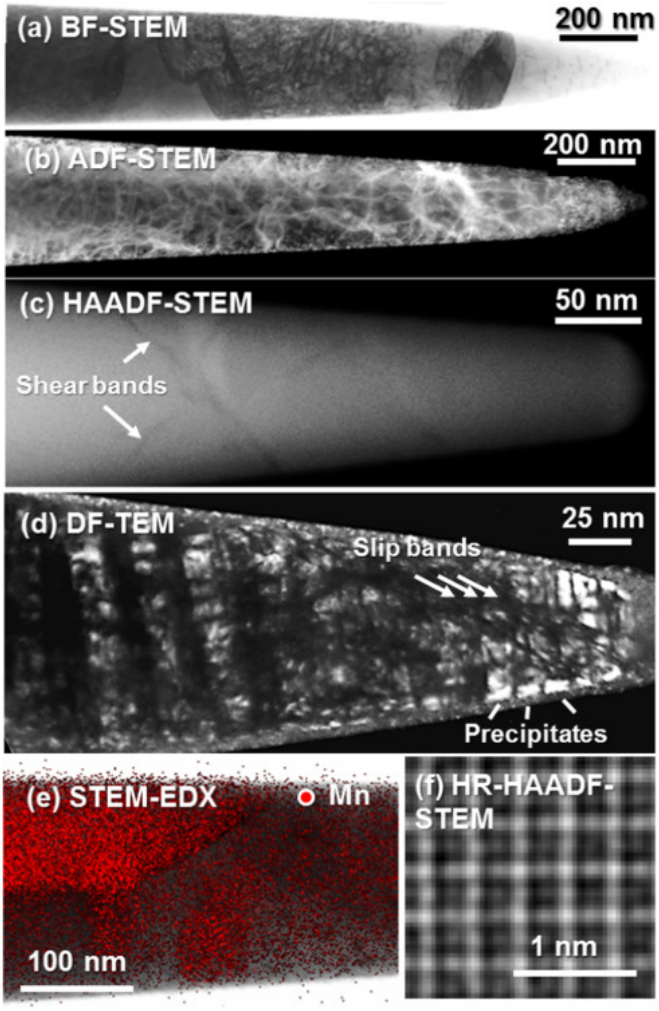

Figure 4: TEM micrographs of APT specimens. (a) Bright-field STEM of a martensitic/austenitic steel. (b) Annular dark-field STEM of a network of dislocations (bright lines) in martensitic steel. (c) High angle annular dark-field STEM of shear bands in a plastically deformed metallic glass. (d) Dark-field conventional TEM of sheared kappa carbides in austenitic steel. (e) STEM energy-dispersive X-ray spectroscopy of martensitic steel with Mn-rich precipitates. (f) High-resolution high angle annular dark-field STEM of a kappa carbide in austenite. (From [138])

Beyond TEM, there have been efforts to make the use of TKD during or at the end of the specimen preparation process in order to characterise the crystallographic orientation [148–

150]. TKD provides details on the misorientation between grains for and can ensure that a grain boundary of interest is located inside the specimen itself. There have been recent reports of possible damage [151] induced by implantation of surface species accelerated under the electron beam [100]. There have been also attempts at correlating with optical spectroscopy [152] in situ. Another approach employs ex-situ experiments using X-Rays or electron spectroscopy[153,154] often on similar, representative samples but sometimes also directly performed on the specimen itself.

3.4 Cryogenic specimen preparations by FIB

The latest developments in vacuum and cryogenic transfers [42] have triggered a lot of interest in the recent past, in part motivated by the study of hydrogen in metals [155] but also by liquid-solid interfaces [156–158] and frozen liquids [159]. These have required dedicated and targeted specimen preparation approaches. Without the need for a full cryogenic chain, using a cryogenic stage for sharpening specimens has been reported to lead to improved yield and data quality for the analysis of organic-inorganic perovskite [160], a reduction in the Ga-induced fracture of Al-specimens [161], and a dramatic reduction in the ingress of H and the formation of spurious hydrides in the preparation of specimens from Ti- and Zr-alloys [162,163].

El-Zoka et al. [157] adapted the "moat“ approach proposed by Halpin et al. [90] using a PFIB equipped with a cryogenic stage, allowing for the preparation of APT from flat films of frozen aqueous solutions [157], liquid metals [164] and organic electrolytes [158]. Schwarz et al. used a Ga-FIB to reduce a larger droplet (tens of µm) held onto the rough surface of a cryo-fractured W-wire into individual needles [159]. This same approach was employed for pure water and various aqueous solutions [165,166].

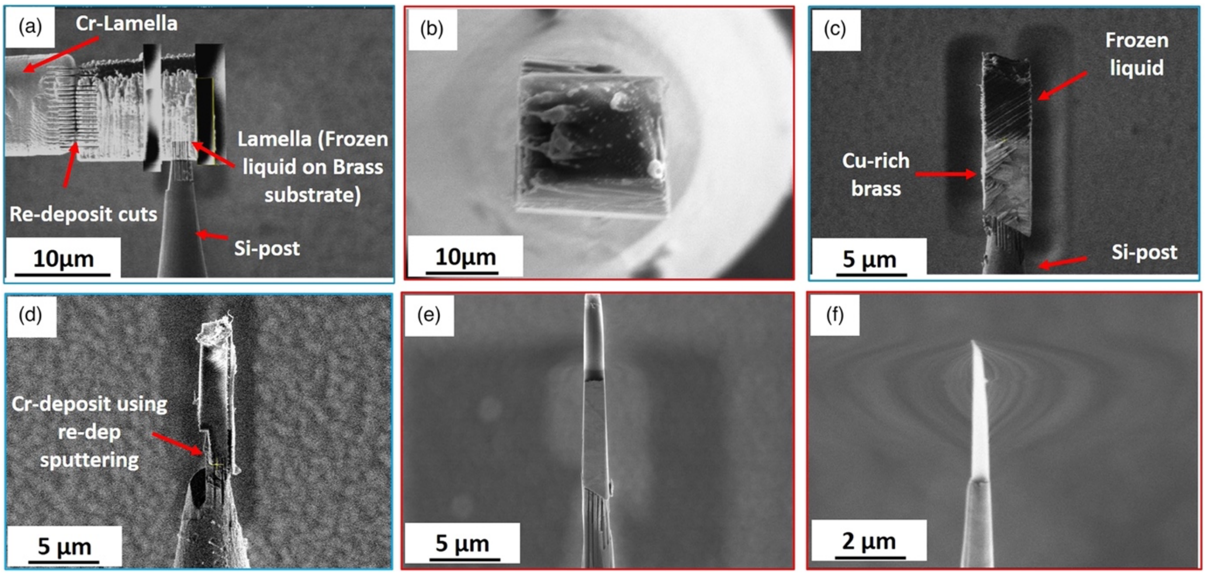

Figure 5: Cryogenic APT specimen preparation procedure for a 0.1 M arginine HCl solution in type I ultrapure water on nanoporous Cu. (a) FIB view, mounting ice on brass on Si microtip. (b) SEM view of mounted ice sample. (c) FIB cross-section view of ice APT specimen (figure and caption from Woods et al. [167]).

In 2018, Schreiber et al. demonstrated an extension of the lift-out protocol at cryogenic temperature [168]. This was based on the use of redeposition to weld the lifted-out cantilever instead of the deposited metal-carbon composite. This was necessary because the cold specimen, manipulator, and sample stage gettered the metal-carbon gas and prevented its deposition only in the intended area. The ion beam is used to form a series of thin lines across the interface between the support and the lifted out sample, in Figure 5a, causing intermixing between the two materials, thereby creating a weld. Similar approaches are commonly used for TEM lamella preparation, yet the strength and conductivity requirements for APT specimens are more stringent. Douglas et al. [169] proposed to strengthen this interface by depositing metal locally. They achieved this by rastering the ion beam onto the end of the W-micromanipulator placed into a gap made on the side of the sample where the ejected sputtered metallic atoms fill this gap. This process was then adapted by Woods et al. for other metals than W [167], as indicated in Figure 5d. This approach for specimen preparation allows for complete workflows for site-specific analysis at cryogenic temperature and was used for e.g. metallic materials, ceramics, and frozen liquids.

3.5 Specimen capping

Capping APT specimens has long been reported to lead to improvement on several aspects of APT performance, particularly the mass resolution and yield [170,171]. The latter is attributed to the filling of pores that can act as stress concentrator[121,172,173]. Capping has so far been performed by taking pre-shaped specimens into a separate preparation chamber. They are then exposed to ambient atmosphere, and capped using sputtering[171,174] (Taylor et al., 2018), physical- and chemical-vapor deposition [175,176], or atomic-layer deposition [130,177]. Graphene conductive coatings have also been reported to facilitate analysis from poor conductors and to allow for encapsulation of small volumes of liquid [178,179].

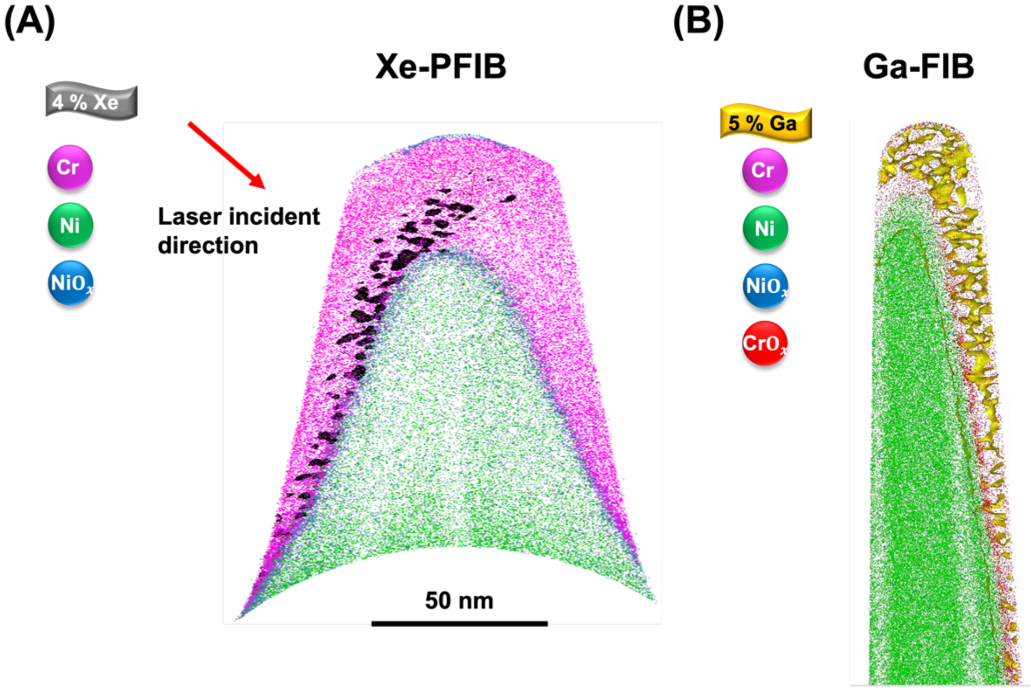

Figure 6: Comparison of the structure of the Cr layer produced with a Xe+ and Ga+ FIB. In (A) the Xe clusters with an iso-surface concentration of 4 at. % and in (B) the Ga distribution with an iso-surface concentration of 5 at. % are visualised.

The idea of using redeposition to coat specimens from a metal target placed inside the SEM-FIB was introduced by Kölling et al. [180] in 2009. This method allows for precise control over the region that is coated, the thickness of the deposited film, is versatile with respect to the metal to be deposited and can be used also on flat substrates, including at cryogenic temperature [167]. This was revisited by Schwarz et al. [181] who used a semi-circular cut inside a metal target held by the micromanipulator to form a conformal coating on a range of different materials. They showcased improved yield from better mechanical stability, improved mass resolution from better thermal conductivity, and how the increase in the specimen's radius helps enhance the field-of-view of APT and allows for analysis of the outer surface of the initial specimen. For specimens prepared by FIB, this method requires no transfer into a separate chamber. Capping was demonstrated with Cr, Co, Mg, and a range of other metals, using with a Ga or Xe ion beam, at room temperature under cryogenic conditions. In all cases the coating was conformal and acts as a capping layer over the length of the APT specimen, Figure 6.

3.6 Remaining challenges

Over the past 20 years progress in the preparation of specimens for APT has been tremendous, primarily driven by the availability of FIBs and the development of capabilities for cryo-vacuum transfer. However, there remain some challenges that should not be overlooked. The structural damage caused by illumination from the electron- or ion-beam may not always be visible in APT, especially since the spatial resolution is insufficient to resolve point defects in the lattice, and extend beyond the region where Ga or Xe implantation can be measured [87,99]. This is well reported in the radiation damage community and can be, to a first approximation, modelled by using the stopping range of ions in matter [101]. As part of efforts for charging specimens with hydrogen, there have been recent reports of damage more extensive than maybe expected arising from the use of Ga-FIB. This includes simply during the deposition of the Pt-C composite as well from exposure to the convergent electron beam, especially during TKD analysis over the course of the preparation of specimen [151,182]. For the analysis of light and mobile species, i.e. H or Li, APT has a critical role to play. These species cannot typically be resolved by other techniques at the length scales accessible by APT, yet these interact strongly with structural defects and their distribution can easily be affected by such structural damage.

Li-containing materials have been notoriously challenging to investigate by APT. Beyond possible challenges associated with specimen preparation and handling(i.e. they are reactive and cannot be exposed to air [183]), Li de-intercalation can be caused by the intense electrostatic field [184,185]. Kim et al. [176] proposed that metallic coatings prevent the penetration of the field [186] and offer a means to mitigate these issues an facilitate routine analysis of Li-containing oxides. This was recently demonstrated for NMC811 [187].

Specimen capping is poised to play a critical role in the analysis of such materials. It can also potentially prevent outward diffusion of H from specimens or offer vast improvement in yield and data quality for e.g. frozen liquids or other biomaterials. For soft matter in general, specimen preparation remains extremely challenging since they tend to be highly sensitive to exposure to the beam. Frozen biological materials are sensitive to the freezing rate in order to avoid the formation of crystalline ice that is accompanied by a volume change that can damage the structure of interest [188]. There is currently no easy path for performing APT from these samples.

4 APT from data acquisition to processing and reconstruction

Following specimen preparation and introduction into the instrument, the data is collected by field evaporating the specimen. The main parameters that are adjusted prior to the start or over the course of the analysis are the base temperature, the pulsing mode (HV vs. laser), the relative pulse amplitude or laser pulse energy, and the detection rate set as an average number of ions detected per pulse. These parameters all have some degree of influence on the analytical performance, which will be discussed in the following section. The raw data from the atom probe is a sequence of times-of-flight, one recorded for each detected ion, along with the coordinates of the ion impact position on the detector. These two will be used to perform mass spectrometry and to build the reconstructed tomogram in the form of a 3D point cloud, from which compositional information can be extracted and related to the specimen's microstructure. This section reviews the key aspects of APT data processing and reconstruction.

4.1 Mass spectrometry

4.1.1 General considerations

APT is sometimes referred to as a microscopy technique; the atom probe was originally developed as a mass spectrometer to complement the imaging capabilities of FIM [4]. The concept is that at a given acceleration voltage, the ion's potential energy is converted into kinetic energy. This will be proportional to its charge, since a doubly charged ion has twice the potential energy of a singly-charge ion. Its terminal velocity and hence the time it takes the ion to fly from the specimen to the detector will also be proportional to its mass, since a light ion travels faster than a heavier ion. Over the course of a typical APT experiment, ions are emitted and collected by the position-sensitive detector, and their time of flight measured by assuming that they departed at the top of the last emitted pulse. This latter hypothesis has a number of consequences on the performance of APT as a mass spectrometer, which will be discussed in Section 6. Following some simple calibration [189], along with a correction of the flight distance based on the impact position (a "bowl" correction, i.e. an ion detected on the edge of the planar detector has flown a longer distance than an ion striking the centre of the detector), each time-of-flight is converted into a mass-to-charge-state ratio.

The mass-to-charge data is typically represented as a histogram and referred to as a mass spectrum. Figure 7 a–b shows examples for a steel in which each individual peak, or series of peaks, can be related to a specific atomic or molecular ion with a given charge state. The charge states are most often 1^+ or 2^+, but depending on the considered element's ionisation energies and electrostatic field conditions during the experiment, higher charge states can also appear [190]. For metals, molecular or cluster ions may be uncommon [191], but as shown they are most common in the analysis of alloys containing C or N. Figure 7a contains $^{12}C_2^{2+}$ and $^{56}Fe^{14}N^+$ cluster ions for instance, in which are also common in the analysis of oxides [192,193], nitrides [194] or carbides [195].

4.1.2 Ranging

The association of a peak to a certain ionic and/or isotopic identity is referred to as 'ranging', which consists in defining the lower and higher bounds of series of a range of mass-to-charge ratios, which are recorded into a so-called range file. Each range can be associated with a single or a combination of elements (due to peak overlaps) [196]. At this stage, and despite efforts in this direction, there are no agreed upon standard method for ranging a mass spectrum, making the accuracy of the process rather user-dependent [196–198]. Each defined species is also attributed an “atomic volume” that will be used during the 3D reconstruction process.

From the definition of ranges, for the entire dataset or a defined region-of-interest, the composition can be reported – i.e. as the ratio of ions of each individual species over the total number of ions ranged. In the case where molecular or cluster ions are detected, the composition can also be reported by separating into their atomic constituents. Up to now, the definition of ranges does not usually include information on the charge state or on the isotopic identity of the considered ion, despite APT’s spectral resolution often sufficient to separate peaks of individual isotopes of each element, Figure 7 a–b. Analysis of isotopic ratios can help with identifying specific ions, especially where overlaps exist, but can also be used to date geological materials[199] or better understand radiation-induced transmutations in nuclear reactors [200,201].

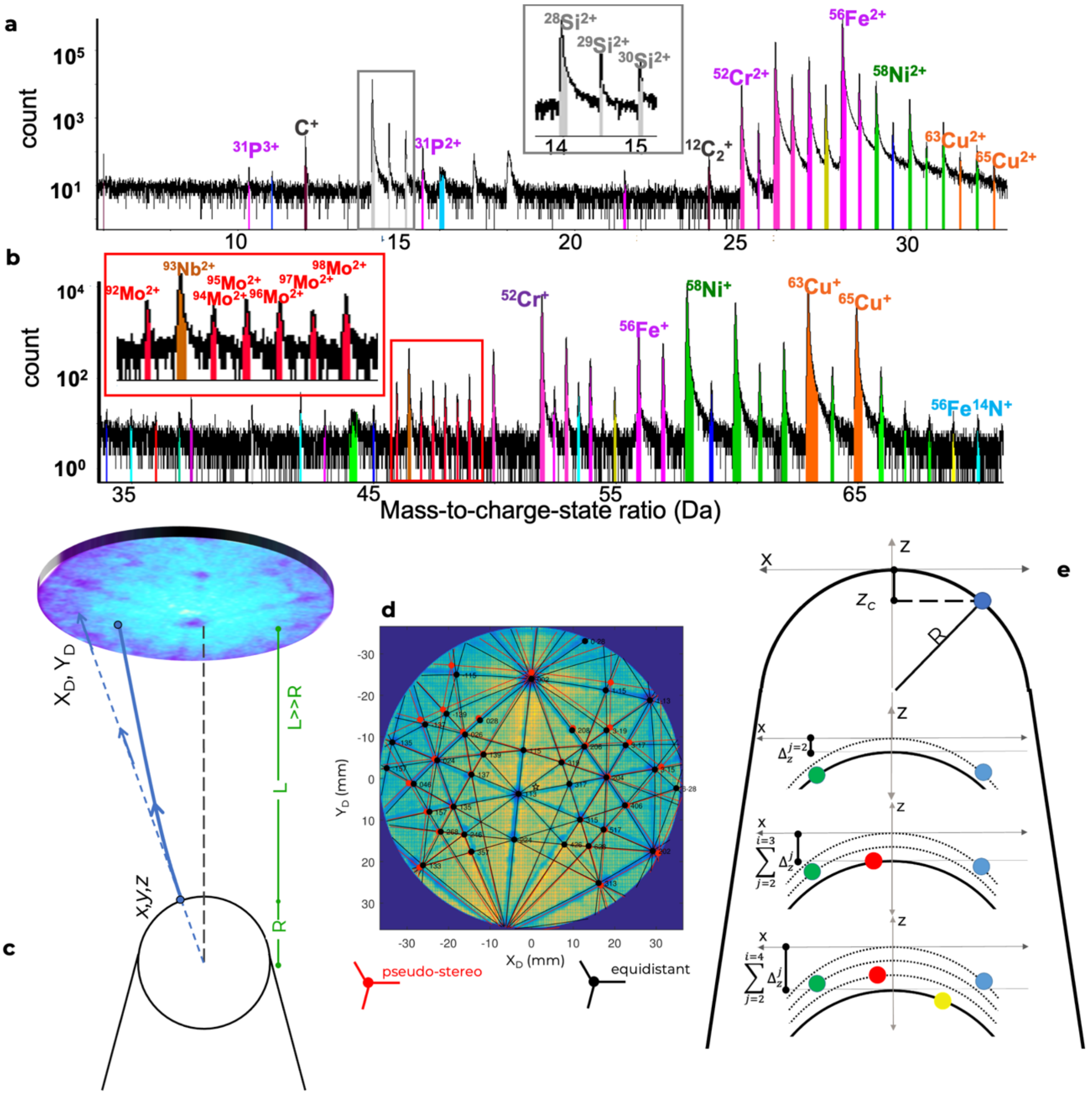

*Figure 7 –**a-b** Mass spectrum from the APT analysis of a 17-4PH steel sample (data courtesy of G. Yeli, University of Oxford), in which ranges have been defined and are highlighted in colour for the different species considered. **c** Simplified schematic of the ion projection from the specimen to detector in a straight flight path atom probe instrument. **d** Comparison between projection models on an experimental pure Al dataset. **e** Simple schematic of procedure to reconstruct real-space depth, i.e., z-coordinate, from top to bottom: the ion detected is assumed to be projected from a hemispherical surface, and for each*

subsequently detected ion an additional increment is added to the z-coordinate calculation to account for all preceding ions (modified from Ref. [202]).

Complexities can arise in the identification of the peaks when there are isobars for different isotopes of different elements, e.g. ^{54}Fe and ^{54}Cr, but also because of the limited precision in the measurement of the time-of-flight. For example, APT does not allow for distinguishing between $^{14}N^+$ from $^{28}Si^{2+}$ both of which will have a mass-to-charge ratio of 14 Da. In Figure 7, the corresponding peak at 14 Da could hence be assigned to either of these two species, however Si has a different isotopic distribution (with peaks at 14.5 Da and 15 Da respectively for $^{29}Si^{2+}$ and $^{30}Si^{2+}$), with amplitudes that correspond to their natural isotopic abundances. This isotopic fingerprinting can help with accurately ranging peaks, allows for correction of the composition [203,204], and has been used to help with automatically identifying peaks [198,205] in the mass spectrum.

4.2 Three-dimensional reconstruction

On modern instruments, the flight distance between the specimen and the detector is in the range 80 mm–200 mm for straight flight path instruments and 400 mm–500 mm for reflectron fitted instruments. Here we will focus on the reconstruction process for the former case. The 3D point cloud is built point-by-point by assuming a simple reverse-projection from the detector impact position onto a ‘virtual’ emitting surface located at the end of an APT specimen. With a specimen radius below 100 nm the projected image of the surface on the detector, Figure 7c, has a magnification that is in the range of 10^6. This arises from the highly curved surface of the specimen, since the ions fly near-radially initially. The trajectory progressively curves towards the detector forming a highly compressed imaged on the surface on the detector. Bas et al [81] proposed to simply 'de-magnify' the detector coordinates (X_D^i,Y_D^i) into the real-space location of each ion within the specimen (x^i,y^i,z^i) by dividing by a magnification estimated based on an assumed specimen geometry in the form of a spherical cap on a truncated cone using a simple back projection law [80,206].

Although the real trajectories of the ions are determined by the distribution of the electrostatic field, making them independent on the ion’s charge and mass, and of the applied voltage[207], the projection laws used ignore the complexities of the actual trajectories to establish a bijective relationship between a point on the emitting surface and a point on the detector. Multiple other projections models have been proposed [206,208,209], with the most commonly implemented is a quasi-stereographic point-projection [81,210,211], Figure 7d, leading to slight distortions at higher angles. The angular compression of the trajectory is typically between 1.4 and 2 [80,81,212,213], and depends on the specimen geometry, i.e. radius of curvature and shank angle. Hence, it varies over the course of the analysis [214,215].

The reverse-projection of each ion on the emitting spherical cap provides a set of x,y coordinates. As each ion is processed, this emitting surface will be moved down by an increment Δ_z^i, meant to account for the progressive erosion of the specimen, as depicted in Figure 7e. This increment is proportional to the volume assigned to each ion during the ranging process discussed in Section 4.1.2. Ultimately, the reconstructed n^th^ ion’s z-coordinate is the sum of the z-position from the reverse-projection and the sum of the successive depth increments $\sum \Delta_z^{i=1\ to\ n}$.

Finally, the assumptions in this reconstruction paradigm require knowledge of the specimen’s radius to determine both the magnification and the reconstructed position. Since it is not measured directly in the atom probe, it is indirectly estimated: from the measurement of the voltage, assuming a simple proportionality between the two [81], or imposed based on an expected geometry of the specimen (e.g. from an electron microscopy image)[210]. Both approaches suffer from limitations. Other ways to calibrate the reconstruction have been proposed and will be discussed in Section 4.3.2. Despite its simplicity, this method leads to impressive results, allowing for the reconstruction of atomic planes in the analysis of many materials [81,135,137]. It provides insights into the microstructure on the nanoscale as illustrated in Figure 8. The intrinsic limitations of the reconstruction protocol will be discussed in Section 6.4.

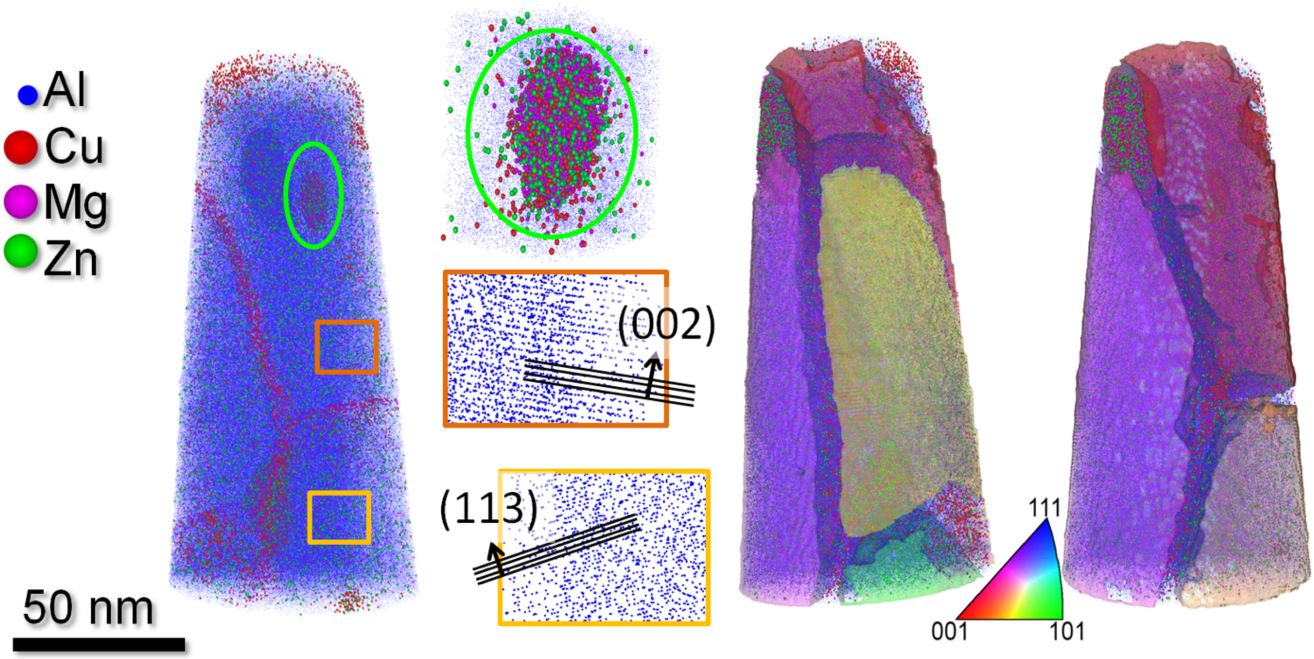

Figure 8: Point cloud showing the elemental distribution in the analysis of a nanocrystalline Al alloy. Segregation of solutes to the grain boundaries is readily visible (for more details on the materials & analysis, please refer to [216]), with a close up on a single precipitate and different families of atomic planes. Two projections of the same volume where individual grains are highlighted by isodensity surfaces are also displayed and coloured according to their orientation relative to the z-axis of the tomogram.

4.3 Data visualisation, segmentation and analysis

One of the appeals of APT is its capabilities for 3D visualisation of microstructural features in complex materials. This may also be one of its curses as quantitative analyses or limitations arising from limited resolution are not well understood by the lay user. Beyond the possibility to display the spatial distribution of each individual species, as defined during the ranging process (Section 4.1.2), Figure 8, there are numerous methods that have been developed for the visualisation and quantitative analysis of APT data. For instance, regions-of-interest of various shapes (cuboidal, cylindrical, spheroidal) can be defined, and the local composition can be measured within them. Profiles revealing the evolution of the composition along a specific axis of the region-of-interest can be calculated. In addition, there are numerous methods involving the calculations inter-atomic distances inside the point cloud or coarse graining, i.e. voxelization, to facilitate visualisation or analysis.

Some of these methods were deployed on a single dataset from the analysis of a corroded Ni-alloy, as shown in Figure 9.In Figure 9(a) the point cloud is displayed, and superimposed are isosurfaces built upon sets of (1x1x1) nm^3 voxels delineating regions within the point cloud containing above a certain threshold of an ionic of atomic species. In Figure 9(b) is a region of interest extracted from within one of the closed isosurfaces that was used to segment the data and allows for localised analysis. Figure 9(c) is a distribution of the distance to the first nearest neighbour of the same atomic-species – here Cr – Cr. Finally in Figure 9(d) is the variation of the composition as a function of the distance to an isosurface (in this case the one marked by the orange box), which allows for quantifying the distribution of species inside the selected particle and its surroundings. This approach is known as a proximity histogram or proxigram [217]. Below, these different tools are discussed in more detail.

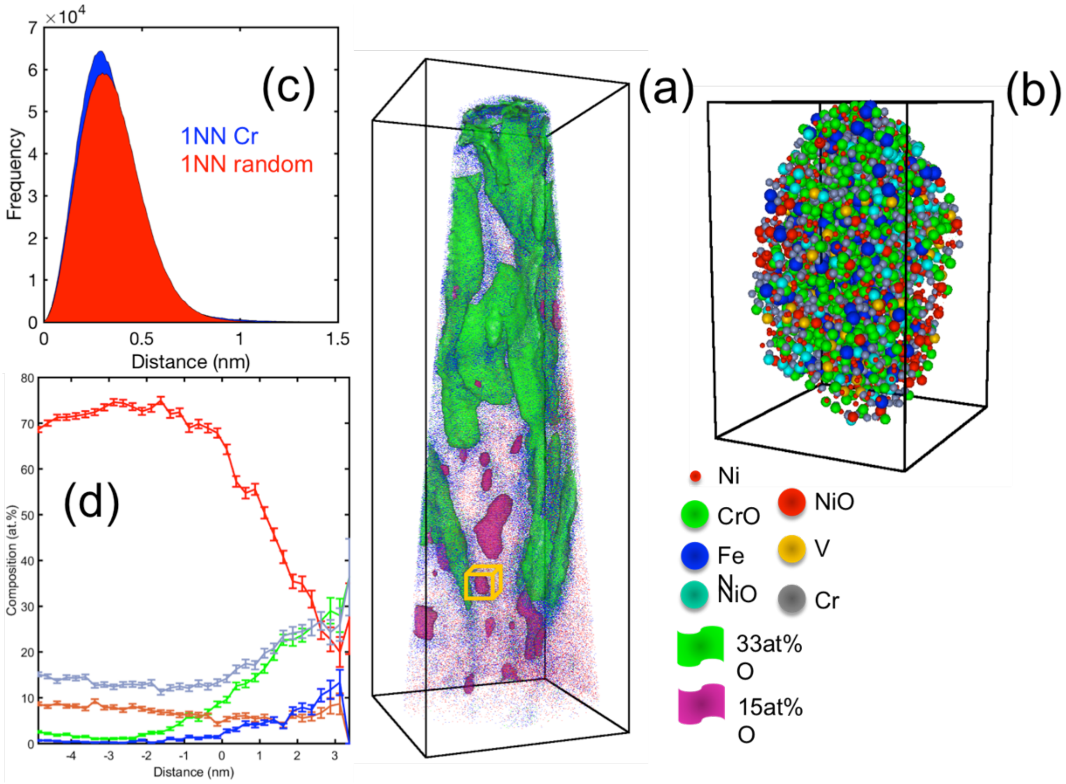

Figure 9: Visualisation and analysis of an APT dataset obtained from an oxidised Ni-based alloy (for details, refer to *[218]*). *(a) Point-cloud and isoconcentration surfaces highlighting the internal oxidation process coming from the surface as well as small oxide islands in the bulk of the sample. (b) An individual cluster isolated from within the data using a cluster-identification method, highlighted with the yellow cube in (a). (c) First nearest-neighbour distribution for Cr showing a slight clustering tendency. (d) Composition profile in the form of a proximity histogram from the isoconcentration surface within the yellow cube in (a) (from Ref. [219]).*

4.3.1 Interatomic-distance-based methods

A first set of methods for processing APT data is based on calculating distances between points of the same or different species.

The simplest is commonly referred to as Kth nearest neighbour (NN) analysis [220,221]. This method plots the distribution of distances between an atom and its successive shells of nearest neighbours, i.e. 1st, 2nd , … Kth. It is in the form of a histogram that can then be compared to a random distribution of points, allowing for assessing tendencies for clustering. The parts of the 1NN distribution at larger distances have been used to extract information regarding the composition of the matrix [222,223]. KNN analyses are now categorised as an unsupervised machine-leaning method, like most cluster-finding approaches. These also involve the measurement of interatomic distances, which are then used based on an array of criteria to segment the data between “clusters” and “matrix”. The most common criterion used is a maximum separation distance(d_{max}) between solute atoms that belong to a cluster, either to the first or higher-order NN [224,225].

The initial set of clustered atoms excludes the solvent atoms – so as to focus exclusively on the solutes. In a second step, atoms from the solvent are incorporated into clusters through approaches knows as 'enveloping'. These add a shell of atoms around each solute within the cluster, followed by an 'erosion' step where atoms at a certain distance from the shell of the solute cluster are removed [225,226]. Other flavours of similar approaches have been proposed [227,228], using e.g. higher-order nearest neighbour distances [220,221,229] or Gaussian mixture models[230]. In the end, each technique has strengths and weaknesses that have been discussed in extensive review articles [227,228].

Following cluster identification, their distribution can be assessed with respect to their composition, aspect ratio, shape, or size either in terms of number of atoms or their radius [231,232]. These can then be compared to what would be expected from random distributions of solutes inside of a matrix to gauge the physical meaning of the distribution, i.e. a tendency for cluster formation. The most employed approach is known as randomly-labelling, whereby the reconstructed positions of the atoms inside the dataset are maintained, but the list of mass-to-charge ratio is randomly swapped, and with this the elemental identities.

Clustering tendencies can also be assessed by using radial distribution functions, which compute the composition in successive shells of a set thickness but with increasing radius around each atom of a certain species or set of species within the reconstruction [233–235]. The data can then be reduced into a 1D-distribution, which can then be processed to quantify the volume fraction or number density of clusters [104] based on a model similar to what is used to process data from small-angle scattering experiments [12].

Some challenges may arise in that solute clusters may not be well-defined microstructural objects with an abrupt interface. This is compounded with the aberrations in ion trajectories arising in the early stages of their flight that limit the spatial resolution of APT [12,236]. Following field evaporation and reconstructions, two neighbouring atoms at the surface of the specimen are unlikely to be first nearest neighbours in the tomographic reconstruction [33]. There are also missing atoms within the reconstruction because of the limited detector efficiency combined with losses from grids used for ion optics on the path of the ions (35 %–90 % depending on the instrument used). APT reconstructions are hence imperfect and incomplete, which makes the objective definition of what is a cluster and what is a matrix inherently incompatible with the results of cluster-finding algorithms that often only offer a binary classification. These algorithms have a number of input parameters, and their selection has a significant influence on the result of the segmentation [237]. Despite proposed heuristics for parameter selection[238–240], none have yet become widely adopted.

4.3.2 Structural analysis

Methods have been developed to calculate the three-dimensional distribution of atoms surrounding each atom in a dataset, which is similar to the 3D calculation of the radial distribution function [234]. These help provide an average view of each atoms neighbourhood [241], which can then be split into a 2D distribution of neighbours within the plane containing the atom and a 1D plot of the average density of atoms as a function of the distance normal to that plane. This approach is referred to as spatial distribution maps (SDMs) [242,243]. SDMs can be used to quantify the distance between the atomic planes, as often imaged by

APT, Figure 8, [135]. This partial crystallographic information had also been characterised by Fourier Transforms[244] and Hough Transforms[245]. These approaches have played a critical role in facilitating the calibration of the reconstruction – i.e. the adjustment of the free parameters used in the reconstruction paradigm described above in order to obtain the interplanar spacing or angles expected from the crystallography of the material of interest [246].

4.3.3 Coarse-graining methods

Another set of methods for data processing is based on coarse graining the data by dividing it into blocks of fixed number of atoms or into blocks of fixed volume, i.e. voxels. The composition is calculated in each block or voxel and used as a basis for filtering or performing statistical analysis. With blocks, the distribution of composition of given species can be compared to random distributions [247,248] based on e.g. a binomial distribution or randomly-labelled data. The "randomness" is then typically assessed by using a χ^2 approach or a Pearson coefficient that varies from 0 for a distribution compatible with a random distribution to 1 for a fully separated system [248].

Voxel-based methods are more commonly used. The 3D composition map from the voxelated APT data is often subjected to Gaussian smoothing through application of a "delocalisation" function meant to reflect the lack of precision arising from the limited spatial resolution of the technique [249]. Among these, isosurfaces facilitate visualisation of regions of different composition joining adjacent voxels that contain above or below a threshold of composition or a number density of atoms of one or more species, Figure 9a. The threshold is somewhat arbitrary and selected by the user, with some limited efforts at defining heuristics for threshold selection [250].

From these isosurfaces, composition profiles can be calculated as a function of the distance to the selected surface based on the local normal to the isosurface. These are referred to as proximity histogram aka proxigrams [217,251]. A proxigram is plotted for an individual particle in Figure 9d. Proxigrams are very commonly used but have some limitations that are sometimes overlooked [252], particularly for regions exhibiting a complex shape. Finally, voxels of a fixed size can be replaced by meshing, upon which the composition can be calculated and mapped[253,254]. This allows for revealing local patterns associated to the topography of the interface of interface [255].

4.4 Analysis of additional hit information

There has been an increased interest in exploiting information beyond the conventional spatial coordinate and mass-to-charge ratio. For instance, the impact coordinates are all stored, enabling the calculations of detector hitmaps that can facilitate identification of features helping to characterise the crystallography of the sample, as in Figure 7c. Amongst the information stored for every ion is the multiplicity, i.e. how many other ions were detected that were emitted by the same pulse. It was noticed that the number of multiple events was far higher than what would be expected for a random distribution because of correlated field evaporation [256], i.e. the departure of an atom leads to neighbouring atoms to leave on the same pulse or shortly afterwards. This is likely related to the dynamic rearrangement of charges at the specimen's surface that cause a redistribution of the electric field putting some atoms suddenly under much higher fields [257]. Further filtering based on distance between impacts for ions detected as part of multiple hits can also be performed and reveal important aspects of the physics of the fragmentation of cluster ions [258].

In general, field evaporation at higher fields also leads to increased rates of multiple events. Mass spectra can be filtered based on hit multiplicity. The multiple event mass spectrum reveals a lower level of background (background comes primarily from low field evaporation and hence on single events), thereby making high-field species easier to measure more accurately [259]. This improves quantification for some challenging species such as C and B [17,260].

In 2011, Saxey introduced to APT an approach used in other mass spectrometry techniques, that plots a two-dimensional histogram of the number of pairs of ions with specific combinations of mass-to-charge arriving on multiple hits [261]. These have since been used to study specific patterns of dissociations of cluster or molecular ions for instance, particularly pertaining to the analysis oxides [262], nitrides[261], hydrides[263] and carbides [264], and more recently water[159]. These have been instrumental in revealing oxygen loss mechanisms [265] along with some important aspects of the dynamic of molecular ions under intense fields and the mechanisms of fragmentation [266].

5 Modelling

The final output data provided by APT is a representation of the analysed material as a 3D point cloud reconstructed with high spatial precision and relatively good accuracy. As such, APT is the only microscopy and microanalysis technique routinely offering analytical imaging in 3D across almost all solid-state materials at the sub-nanometre scale. APT's elementally resolved point cloud is similar to datasets produced by atomic simulation, facilitating direct comparison of experiments and atomistic modelling. Before extrapolating material or physical information from APT data comes the ultimate question: "How real is what I observe?". The answer to this question is not obvious. First, because there is often no other technique that provides similarly-resolved information for direct comparison, and second, because the metrological performances of APT are only known for selected measurement standards such as pure metals and well-defined structures or alloys [267–269].

Modelling the imaging process is necessary to assess the validity of the measurement. As discussed previously, the reconstruction process to transform experimental raw detector data into a 3D map of atomic position is relatively simple and has evolved relatively little since its introduction in the early 1990s. The reconstructed atomic positions are deduced from the list of the impact coordinates of the ions on the position sensitive detector resulting from field evaporation of the specimen's surface atoms. The properties of the ion projection are directly determined by the specimen itself, since as the specimen is progressively eroded the field evaporating surface evolves in a complex manner. Understanding how the image is reconstructed in 3D thus requires a fine understanding of the APT imaging process. The magnification is APT is produced by the specimen itself, and the quality of the reconstruction is hence strongly dependent on the evolving morphology of the specimen surface during the analysis. This makes APT different from conventional microscopy for which the specimen and optics are independent and the performance limits depend on the quality of the optical system.

The need for modelling tools was expressed very early after the development of first APT prototypes in the 1990s [25,82], and built on preliminary efforts for field-ion microscopy [270–272]. We may note that the development of numerical modelling tool to reproduce the imaging process these last 30 years confirmed the validity of the empirical developed reconstruction recipes[236,273–276]. These models are moreover able to predict potential reconstruction artefacts inherent to the physics of ion emission at the surface of the studied specimen [236,274,277,278]. They are therefore a key tool to validate experimental observations. In addition, a strong effort was recently made to produce a more accurate reconstruction algorithm through leveraging the tight interplay between experiment and simulations. This approach is in its infancy since it relies on the development of artificial intelligence methodologies that necessitate feeding the algorithms with vast amounts of known information. In this section we will cover the main aspects of the imaging process, the methods used to build tomographic reconstructions, atom probe tomography modelling methods, and the intrinsic metrological limitations of APT. We will also explore the current approaches to understand limitations in the reconstruction process as well as future potential directions to improve the integrity of 3D images.

5.1 Electrodynamical approach of the imaging process in APT

The imaging process in APT is uniquely controlled by the behaviour of ion trajectories between the emitter's surface and the detector, which makes understanding of the physical process relatively straightforward. Since the specimen is in vacuum, at cryogenic temperature, and the process involves mostly of the non-time correlated ion emission (no ionic charge space effects), the trajectory is entirely defined by Newton's equations of movements applied to a single ion starting with negligible initial velocity. If **r** is the vector-position of an ion in the instrument, the trajectory follows the classical equation:

$$\frac{d^2\boldsymbol{r}}{dt^2} = \frac{\mathrm{ne}}{m}\boldsymbol{F}(\boldsymbol{r},t), \qquad \text{(Eq 6.1)}$$

where ne is the electric charge, m the mass, and $\boldsymbol{F}(\boldsymbol{r},t)$ is the vector electric field in space that can be time varying when voltage pulses are applied.

$\boldsymbol{F}(\boldsymbol{r},t)$ can be derived from the electric potential distribution $\boldsymbol{F}(\boldsymbol{r},t) = -\boldsymbol{\nabla V}(\boldsymbol{r},t)$. It can also be derived from the distribution of charge existing on the surfaces of the electrodes surrounding the ion considering that any surface dS with a surface charge σ produces an additive electric field $\boldsymbol{dF} = \frac{1}{4\pi\epsilon_0}\frac{\vec{r}}{\boldsymbol{r}^3}\sigma dS$.

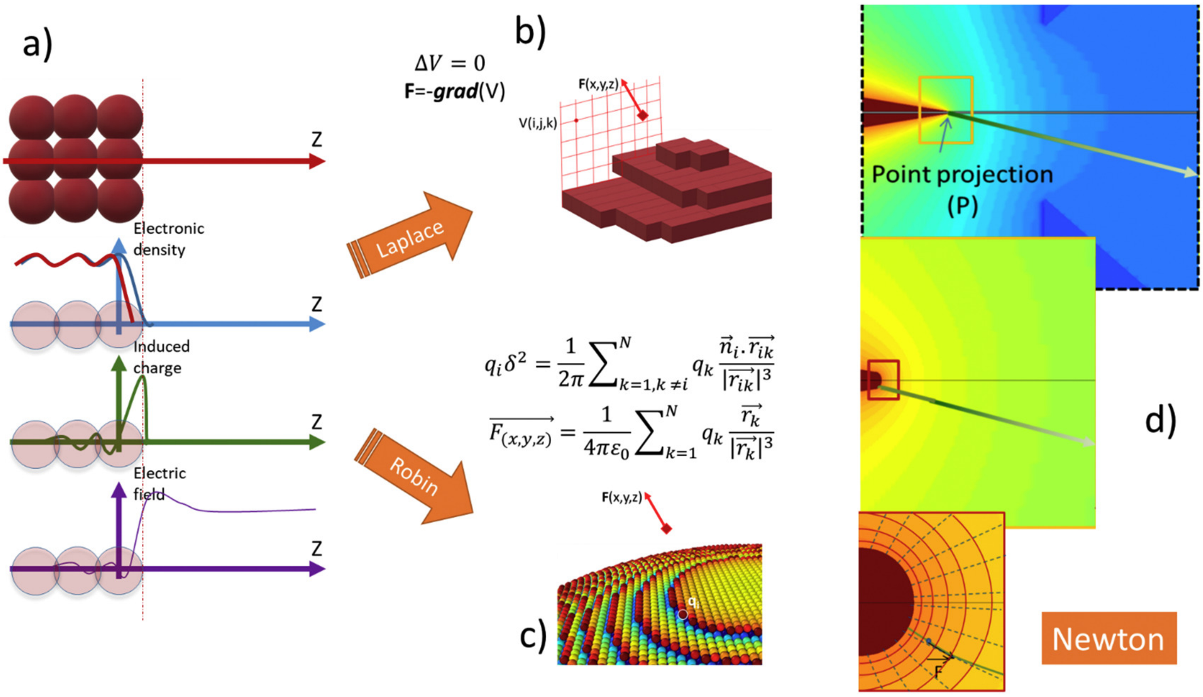

Figure 10 (a) Field evaporation assuming a quantum model of atoms. The application of a voltage on the sample changes the electronic density from the blue curve with no voltage to the red curve with an applied voltage. Electronic density is slightly shifted inside the materials, which gives rise to a positive effective charge localized on the surface atom (in green) and the *local electric field F (in purple). This mechanism is modelled through (b) simple approximations of the Laplace equation, or (c) the Robin equation. These enable (d) determination of the ion trajectories from the resolution of the Newton equations.*

The 3D distribution of the electric field is a classical problem that can be answered by solving the Laplace equation (electrostatic approximation) using a known geometry (figure 10). Conditions of constant voltage are used on metallic surfaces. In older models applied to an arbitrary emitter shape, determining this field was difficult because of the nine or ten orders of magnitude variation in length scale going from the specimen (defined at the nanometre scale) to the surrounding electrodes (defined on the microscale) to the detector (defined at nearly the meter scale). For certain smooth, symmetrical emitter shapes, the problem is easier to solve analytically. A number of mathematical models of emitter shape have been used and some have an exact solution to Laplace's equation for the electrostatic potential [279,280]. The specimen can be described as a hyperboloid or paraboloid of revolution. Currently, the electrostatic field is more often calculated using boundary element methods (BEM), where the distribution of surface charge on electrodes can be calculated in 3D without the need to mesh the 3D space entirely [59,213]. Using this approach, it is possible to use a fine mesh to define the specimen (sub-nm) and a much coarser mesh for electrode of macroscopic dimensions. Both models (Laplace computation or BEM computation) are equivalent, since they both assume that the density of charges are located on the surface with a penetration depth smaller than the size of a single atom.

In all models, the distribution of the electrostatic field in free space is defined by $\boldsymbol{F}(\boldsymbol{r},t) = F_0(\boldsymbol{r},t)$**,** which is a dimensionless vector distribution function. For a material defined by a single field evaporation constant F_0 [281,282], the specimen field evaporates to reach a steady state shape with a smooth geometry. An example is shown in figure 11a. F_0 is the highest electric field in the system. It was found using different models that this constraint imposes a shape very close to a surface of constant curvature radius R, at least close to the specimen axis. To a first approximation, the electric field F_0 was found to follow then classical expression

$$F_0 = \frac{V}{k_F R} \qquad \text{(Eq 6.2)}$$

where V is the voltage applied to the specimen, and k_F a dimensionless semi-constant, i.e. that is slowly varying as the specimen is field evaporated. k_F is in the range of 2–10, and depends primarily on the specimen's shank angle and end radius [213,214,283]. For a smooth emitter, the hemispherical approximation ±45° about the specimen's main axis is a good approximation of the morphology of the specimen's tip. However, when approaching the outer edge of the end apex, the steady state radius of curvature tends to decrease, which makes the specimen surface more elliptical.

When integrating equation 6.1, it is useful to replace t by a dimensionless time unit t' and $\boldsymbol{F}(\boldsymbol{r},t) = F_0(\boldsymbol{r},t)$**,** which is a dimensionless vector distribution function where $\mathbf{F_0}$ is the initial electric field at the moment of departure from the surface. This means that $dt' = \sqrt{\frac{neF_0}{m}}\,\mathrm{d}t$ and the solution trajectories follow the following equation,

$$\boldsymbol{r}(t') = \iint (\boldsymbol{r},t')\, \boldsymbol{dt}'^2 + \mathbf{v'_0}t' + \mathbf{r}_0 \qquad \text{(Eq 6.2)}$$

where $\boldsymbol{v'_0} = \boldsymbol{v_0}\sqrt{\frac{neF_0}{m}}$ with $\mathbf{v_0}$ being the initial velocity and $\mathbf{r_0}$ the initial position.

As pointed out by Smith and Walls [207], it can be seen from equation 6.2 that ion paths are independent of the mass, charge, amplitude of applied voltage, or the field provided that the initial velocity is null. The field distribution is then only dependent on the specimen's shape and the geometry of the electrodes. We can add that the emitter's shape is the strongest contribution to the high magnification of the instrument. Indeed, the field distribution is produced by the application of a high voltage to the pointed needle and surface charges are highly concentrated at the tip of the specimen. This makes the electric field strongly diverging and produces an intense acceleration in the first steps of the ionic flight (figure 10a). Any ion starting from the surface of the specimen with a position (R,θ,φ), with the specimen described as a hemispherical cap of radius R, is seen to almost radially leave the surface. Only a second order bending of the trajectory induces compression of the trajectory towards the specimen's main axis. The microscope was then modelled as projection microscope with a projection point P located on that axis, at a certain distance mR(with m a constant in the range 0.6-1) from the centre O of the hemispherical cap. In this empirical projection model is referred to as a "quasi-stereographic projection"; a stereographic projection is defined by m=1 [80].

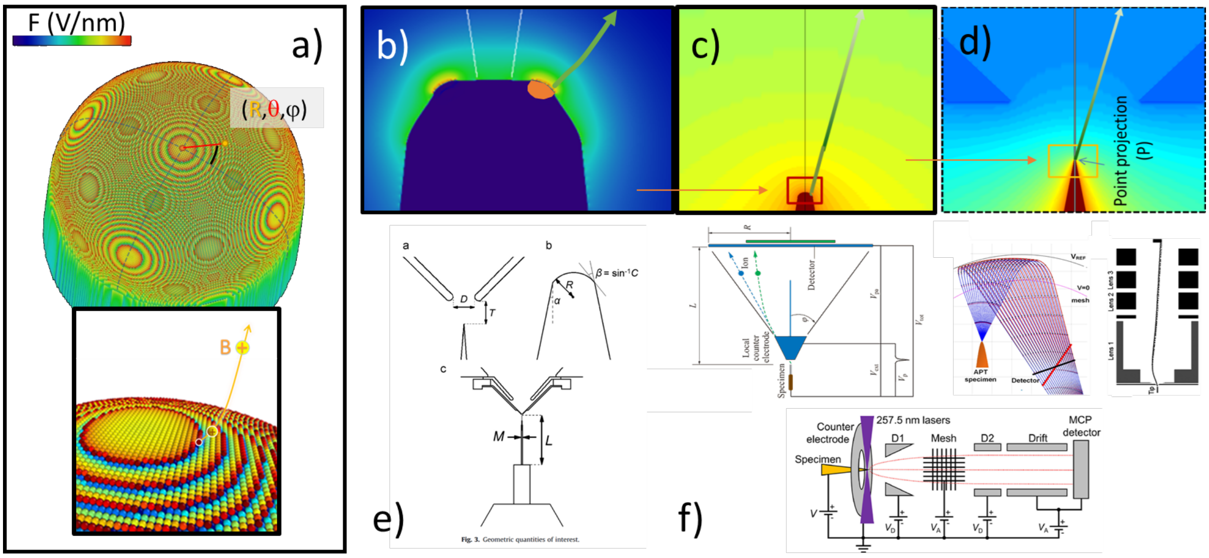

Figure 11 : Visualisation of different length scales in the modelling process of APT applied to different atom probe setups. (a) Atomic scale visualisation of the electric field distribution at the specimen surface when applying a positive kV voltage onto a pointed needle with an end radius of few tens of nanometers. The inset shows the departure of an ion in the field distribution (for details, refer to [284]). (b to d) Electric field and voltage distribution around the sample at the mesoscopic scale. In (d) the edge of a local electrode polarized at ground voltage appears. (e) The size of the local electrode is defined geometrically (common size D~40 microns). (f) Once ions are emitted, they enter into different electrostatic environments including either a straight flight path, energy-compensating reflectron, or an atom probe equipped with multiple complex electrostatic lenses. These latter devices enable collecting a larger field of View [36,285].

We may note also that, even for the simplest approximation regarding specimen and chamber geometries, analytical solutions to Equation 6.2 do not exist, and numerical schemes must be employed to precisely calculate the final trajectories. These calculations were performed as early at the beginning of the 1980s in the context of the FIM and showed the strong impact of the specimen geometry on the magnification of the instrument (figure 10b, c and d). Using FIM, the best empirical model to predict the image projection is a simple proportionality between the radial position L on the detector and the tilt angle θ of the initial position ($L=k_\theta\theta$ relationship) [206,208] that corresponds to a so-called equidistant azimuthal projection [286].

However, the complete trajectory builds up all along the ion's path, integrating the impact of the presence of electrodes and ion optics in the instrument. In the 1990s, the local electrode atom probe [13,287,288] was introduced. This instrument uses conical electrodes with a central hole of a few tens of microns and placed approx. 50 microns from the specimen's apex. This microscope geometry allows for using specimens standing out only a few hundreds of microns above a planar substrate, Figure 11e. Using this geometry, the impact of the presence of the substrate (or a large cone angle) for the specimen could be minimized by the influence of the local electrode. In this case, the projection point is closer to the centre of the hemispherical apex (m~0.3-0.5) [213]. We may note that to the first order, the image is simply angularly compressed. The image compression factor (ICF~m+1) is one of the main parameters in reconstruction algorithms [81,210,211,289].

A second key parameter is the field factor k_F. The field factor, when the evaporation field F_0 is known, enables one to estimate R. Similarly, the ICF associated with the impact position of ions enables one to find the initial angles (θ, φ) onto the specimen. Simple geometrical relationships are used to perform point cloud data reconstructions. The use of local electrode atom probes and specimens prepared by focused-ion beam have reduced the variability of the field factor and ICFs. Commercial software programs typically propose constant, defined values that correspond to some "average" specimen geometry and maybe be derived from simulations. When performing a reconstruction, these parameters are held constant. This has been demonstrated by different authors [214,215,283,290] to inadequately reflect reality. Studies have revealed substantial variations in k_F and ICF with both depth and angular position across the field-of-view. This suggests that instead of being held constant, these parameters should be dynamically adjusted throughout the reconstruction [214,215,283,290]. Recent advances in electrostatic solvers have overcome the sheer complexity of the microscope chamber and have enabled better approximate solutions to the variation of k_F and ICF. As result, a new methodology for reconstruction, referred to as "*dynamic reconstruction*", has enabled improved reconstruction in the analysis of single-phase materials [214,215].

Since the 2000s, several new concepts of atom probes were developed to significantly increase the field of view of the instrument without sacrificing the time-of flight performance (figure 10f). This is accomplished by adding electrostatic devices to compress the trajectories along the path of ions. Electrostatic models were used to calculate ion trajectories considering the geometries of electrodes for electrostatic curved mirrors or for various designs of Einzel lenses. Since these devices are macroscopic and situated well after the voltage space varying region induced by the specimen and the local electrode, the impact on ion trajectories is found constant for an ion with a given acceleration voltage. The transfer function of the electrostatic device is calculated and integrated in the reconstruction software.

5.2 Time varying and velocity influence

As pointed previously, the strength of APT as a nano-analysis 3D microscope is the strong achromaticity of the imaging process: the ion trajectories are theoretically independent of the mass, charge and voltage applied to the specimen in the electrostatic approximation, and assuming no initial velocity.

This last statement is not strictly speaking true when considering the thermal velocity of ions in the first steps of field evaporation. Transverse thermal energy is in the range $E_c \sim k_B T \sim 1$ meV –10 meV at cryogenic temperature and can reach 100 meV in laser pulsing mode and is in fact amplified by the divergent trajectory of the ion. Using calculations from de Castilho and Kingham, the transverse kinetic energy induces lateral noise in the range 0.1nm -0.3 nm in voltage mode [291]. It can reach the nm range in laser pulsing mode which explains partly loss of spatial precision when using laser pulsing mode [292,293].

The impact of additional kinetic energy coming from chemical reaction is also to be considered when trying to understand the imaging properties of the APT in the analysis of non-metallic alloys. APT experiments often incorporate the detection of molecular ions emitted from the specimen, in particular for the case of covalently or ionically bonded materials. These molecular ions are metastable and can dissociate in the high electric field surrounding the specimen [262,265,294]. The dissociation products are then subjected to Coulomb repulsion, which is the effect that is generally exploited in Coulomb explosion imaging [295]. In the atom probe geometry, such repulsion can be expected to induce complex effects on both the ion trajectories and kinetic energies as schematically depicted in Figure 11. The impact of such dissociations was studied by modelling the ion trajectories in the field distribution from the specimen to the detector using phenomenological or ab-initio description of the dissociation process of molecules in high electric field [264,266]. This process was observed in numerous materials, giving rise to a degradation first to the mass spectrometry, molecular fragments presenting kinetic energy deficits or excess induced by the non-standard ion trajectory, and second to degradation of the positioning capability of the instrument. In ZnO analysed by APT, field evaporation of $Zn_2O_2^{2+}$ molecules and their dissociation into ZnO + ions in the high field region in the vicinity of the specimen surface was observed [266]. Coulomb repulsion between the resulting ZnO^+ ions has a significant effect on both their trajectories and times of flight with measured release of kinetic energy up to 3.2 eV. This release degrades the spatial resolution for events resulting from the dissociation of molecular ions by several nanometres. We may note that the impact of these dissociations can also be worse in APT equipped with additional electrostatic devices. In the APT analysis of InP [296], a material producing a large amount of P_n^+ cationic molecules, the formation and subsequent dissociation of phosphorous cations during their flight toward the detector are observed. A thorough analysis of the data shows that delayed dissociations occur in correspondence to low field regions, far from the field emitter surface.

In an atom probe equipped with a reflectron lens, the difference in kinetic energy and kinetic energy spread can be in part compensated, resulting in only partial molecular dissociation signals in mass spectra. When the dissociation is fast and takes place close to the tip, the energy deficit/excess of both daughter ions is small and well compensated by the device (for excess in energy <5 %). When the excess in energy is higher than ~5 % (Figure 6b), the ion with excess energy hits the back-electrode and the ion signal is lost. When the dissociation takes place in the reflectron or after the reflectron, with a delay large enough to avoid filtering the ion in energy excess (Figure 6c), the dissociation is then very delayed (>100 ns) and partial compensation of kinetic energy occurs. In all cases, the presence of the reflectron complicates the interpretation of dissociation tracks in correlation histograms [52,297].

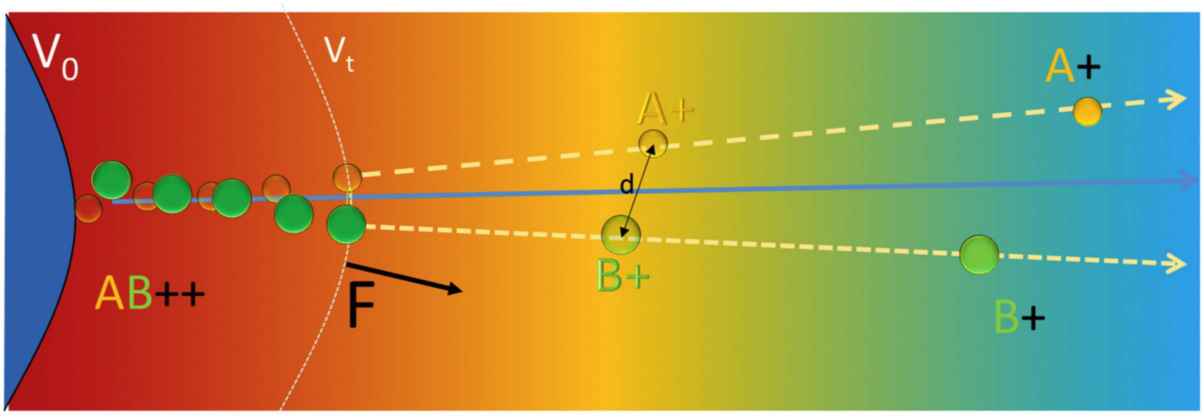

Figure 12: Modelling the impact of in-flight dissociation in APT. Some cationic molecules are not stable during the flight and dissociate in the region of high field. Models are used to understand the impact of Coulomb repulsion between dissociation products and to study ions trajectories that can be expected before and after dissociation as a result of ion/ion and ion/specimen interactions. The different parameters of the dissociation that are studied are the dissociation distance, angle and energy.

The same conclusion can be extended to the case of instruments with additional electrostatic lens. Electrostatic lenses modulate the ion trajectories and act as an energy dispersion filter. The electrostatic lens used to deflect and compress ion trajectories are equivalent to an electrostatic voltage barrier. In this case, dissociation tracks will be deformed by the deceleration/acceleration zones existing in the path of ions and generally electrostatic lenses amplify the positioning errors induced by dissociation [298]. The use of a straight flight path tomographic atom probe instruments is therefore recommended to study dissociation processes [261].

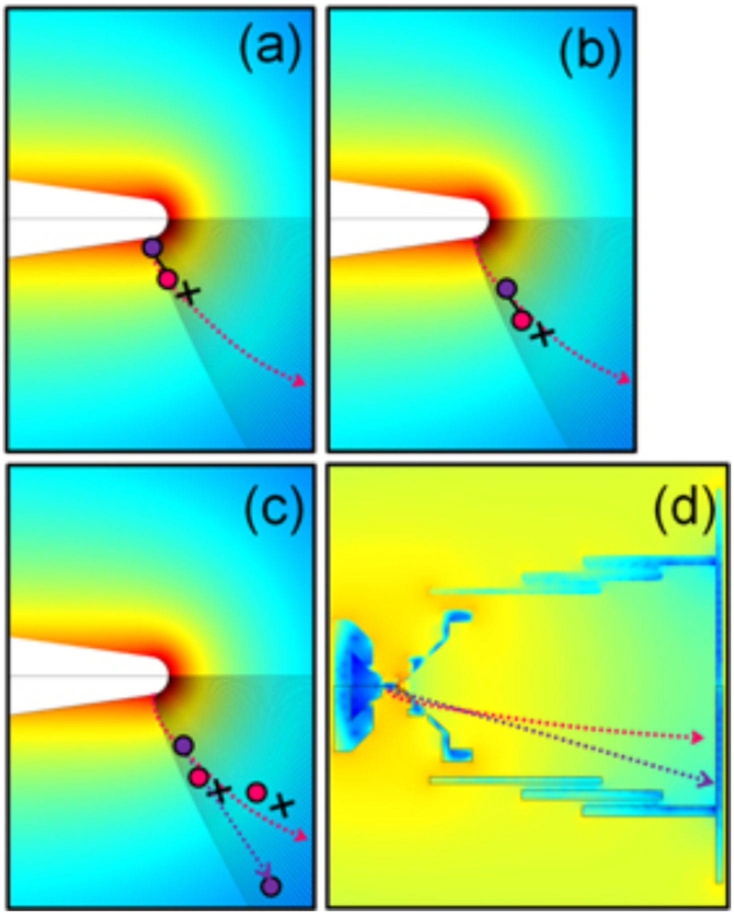

Figure 13: Schematic illustration of the difference in expected trajectory for a neutral and charged fragment in APT. (a) The molecular ion is emitted from the surface, (b) the ion reaches the point of dissociation, (c) the charged fragment (pink) follows a curved trajectory while the neutral fragment (purple) keeps flying straight;,(d) perspective on a full-scale microscope (images from [265]).

The imaging properties of APT are even more perturbed in the case of dissociations that produce neutral species. This was reported in some cases and only through indirect proofs. In reference [265], neutral emission of HO_2 from iron oxide was discussed. By using simulations of ions trajectories within a full-size atom probe microscope, it was found that emission of neutral species after dissociation could lead to a wide spread of incoming position on the detector, depending on the lifetime of the initial molecular parent (FeO_2H^+). This can be explained by the fact that ions follow well-defined trajectories that are dictated by the static field distribution. It is expected that two charged fragments approximately follow the same path since they originate from the same location at the specimen surface. In contrast, the respective trajectories followed by a charged and neutral fragment pair resulting from the same dissociation event should diverge significantly. Momentum is initially acquired by the neutral fragment while it belongs to the parent ion. At the point of dissociation, it can be assumed that it follows a straight trajectory that is the local tangent to the instantaneous trajectory of the parent ion. In contrast, the trajectory of the charged fragment is defined by the static field distribution. These scenarios are depicted schematically in Figure 13.

Dissociation and in particular dissociation producing neutral species has a clear effect on APT data quality. The spatial dispersion induced by field dissociation was for instance fully simulated in the case of SiO^{2+}, where the dynamics were simulated from the sample surface to a virtual detector located at 10 cm. Molecules in different electronic states were placed at the surface of the sample with a surface electric field of ~11 V/nm sufficient to easily dissociate ground state SiO^{2+}. Two dissociation cases and four different fragments are found possible ($SiO^{2+} \rightarrow Si^{2+} + O$; $SiO^{2+} \rightarrow Si^{+} + O^{+}$). The calculated distance between impacts accounts for several millimeters on the detector, in good agreement with experiments. This distance is equivalent to a spatial precision on the tip of 1 nm –2 nm for Si^{+}/O^{+} pairs and 1 nm–5 nm for Si^{2+}/O pairs. It is worth noting that dispersion is larger for Si2+/O dissociation, since conversely to Si2+, the O neutral fragment is not accelerated by the remaining electric field in vacuum that amplifies the distance between impacts on the detector.

Another factor that needs to be considered in APT is the effect of pulsed voltages on the ion trajectories. Equation 6.2 assumes that the field distribution remains constant with time. This was considered in the first designs of atom probes, but the theoretical consequence of time varying effects was not experimentally investigated at this stage. It was found that the final kinetic energy of the ions and the resulting change of magnification could be corrected, but since most of the ions are field evaporated close to the top of voltage pulse, the effects are in fact compensated during the instrumental calibration of the instrument.

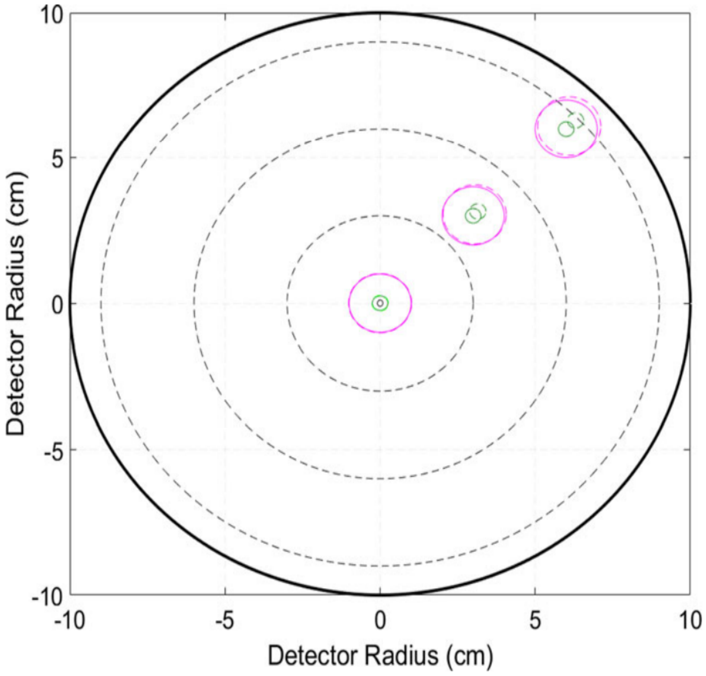

Figure 14 : Schematic representation of chromatic aberration of a virtual precipitate composed of Fe (magenta) and H (green), based on electrodynamic modelling results of a local electrode atom probe in voltage pulse mode. The circle represents the virtual detector of the microscope. The ideal positions are in solid line, the calculated projected precipitate is dashed. The magnification is larger for H^{+} compared to Fe^{2+} showing the impact of dynamic effects.

Recently, the impact of dynamic effects was studied in a straight flight path local electrode atom probe using a full-size atom probe simulation that incorporates a realistic time varying pulse voltage (electrodynamic simulations with Lorentz 2E), for a wide ion mass scale. This enables the investigation of light elements (e.g., H^{+}) to heavy elements (e.g., W^{2+}). It was found that dynamic effects could degrade the performances of AP (mass spectrometry performances and imaging performances). The dependence on the voltage amplitude is strongly visible when the pulse is applied on the counter electrode for ion masses less than 10 Da, in agreement with experiments. Dynamic effects cause some trajectory deviations amplified by the pulse fraction, the angle of departure of the ions, and the ion mass. Again, light ions are sensitive to the pulse amplitude and the pulse waveform. For a standard voltage, the magnification on H+ is ~5 % larger than Fe^{2+}, which can cause chromatic effects in the reconstruction. However, it is worth noting that by quantifying the variation of the compression factor as function of the mass, it is possible to correct the position of the detector impact. This is not routinely implemented yet.

5.3 From the microscale to the mesoscale

The strong magnification in APT is achieved through the high curvature of the specimen's tip, where the electric field is strongly enhanced. Due to the near-radial distribution of the field, the ions (evaporated atoms) fly initially radially from the specimen's surface towards the detector. However, the local electric field is non-uniformly distributed across the specimen's surface, including between two neighbouring atoms, and this leads to trajectory aberrations [236,299,300]. Any deviation in trajectories very close to the surface will be strongly magnified at the detector, and the distance between the impacts of ions that were initially neighbouring atoms on the surface increases proportionally to the flight distance. In principle, the trajectory of each ion is deterministic, and follows a path imposed by the distribution of surrounding atoms that builds the local field distribution. In the future, reconstruction models will have to integrate the distribution of the electric field in the first steps of flight in order to reduce the aberrations [236,274,301,302]. Let us walk through a few aspects that would need to be accounted for to improve APT reconstructions.

Blade-shaped specimen are not uncommon, either when electropolishing a blank that does not have a perfectly square cross-section or during FIB preparation of materials composed of phases with strong differences in sputter yield [303]. Figure 15 evidences the difference in the ion projection between a specimen with and without cylindrical symmetry, demonstrating that the most-commonly used reconstruction protocol will fail to reproduce a correct image for blade-shaped specimens.

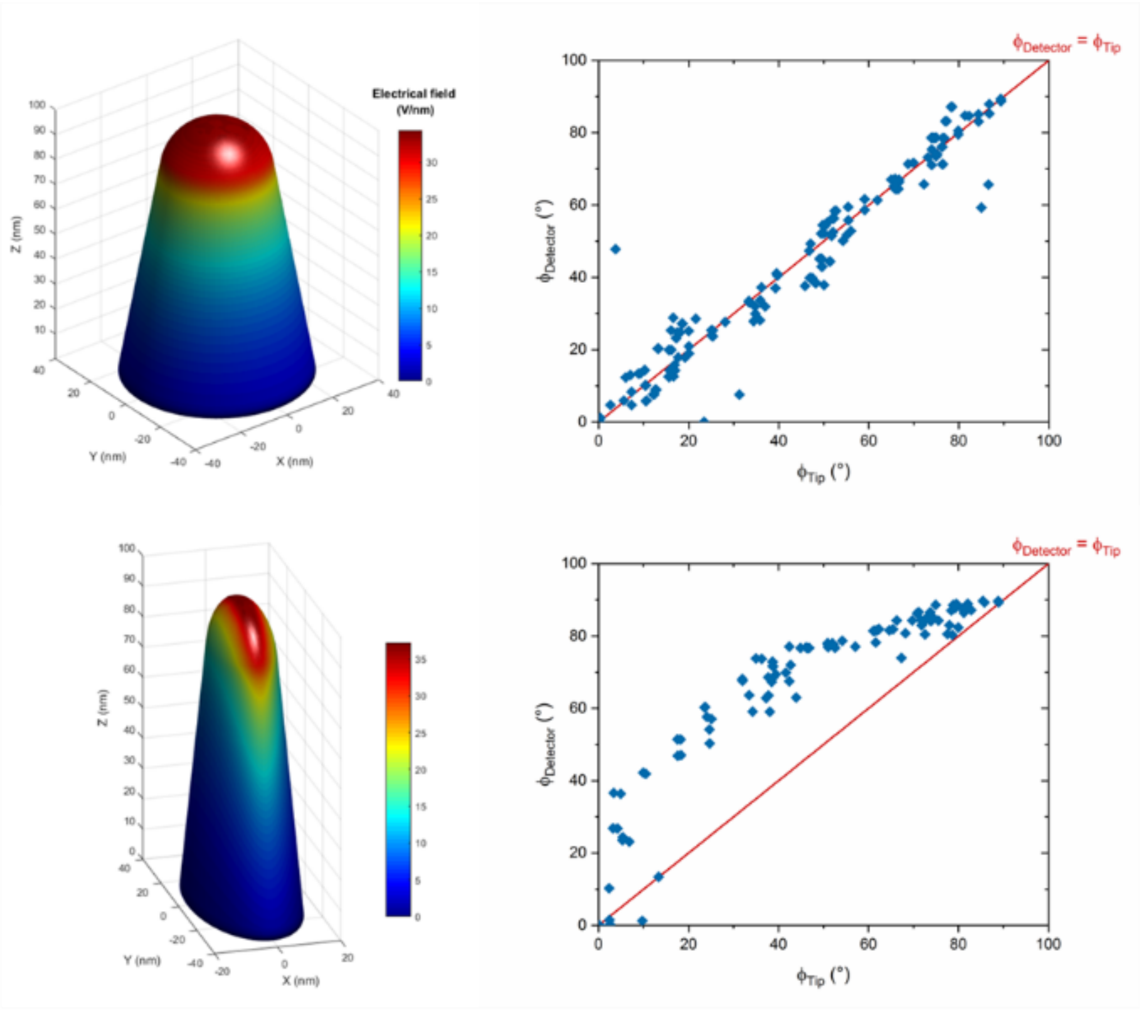

Figure 15 Comparison between the image projection calculated for a specimen with rotational symmetry along the needle axis (top), and a specimen with a blade shape (bottom). In both cases the azimuthal angle ϕ around the specimen axis of the initial of an atom the surface and the position of its corresponding ion hit on the detector was drawn. In the latter case the conventional inverse projection law used to reconstruct atom probe dataset fails and must be corrected.

Several authors have proposed usable solutions for advanced models to calculate the reverse projection [73,302]. The first issue that must be tackled by these new approaches is the variations of reconstruction parameters arising from the gradual change of the emitter's shape over the course of the analysis. The most striking example of artefacts that are theoretically possible to correct is the variation in magnification that occurs when analysing a material composed of phases with different evaporation fields. Phases with low evaporation field exhibit a lower magnification, which induces a significant variation in impact density between phases. This 'local magnification' effect is particularly evident when analysing small precipitates embedded in a matrix [236,304].

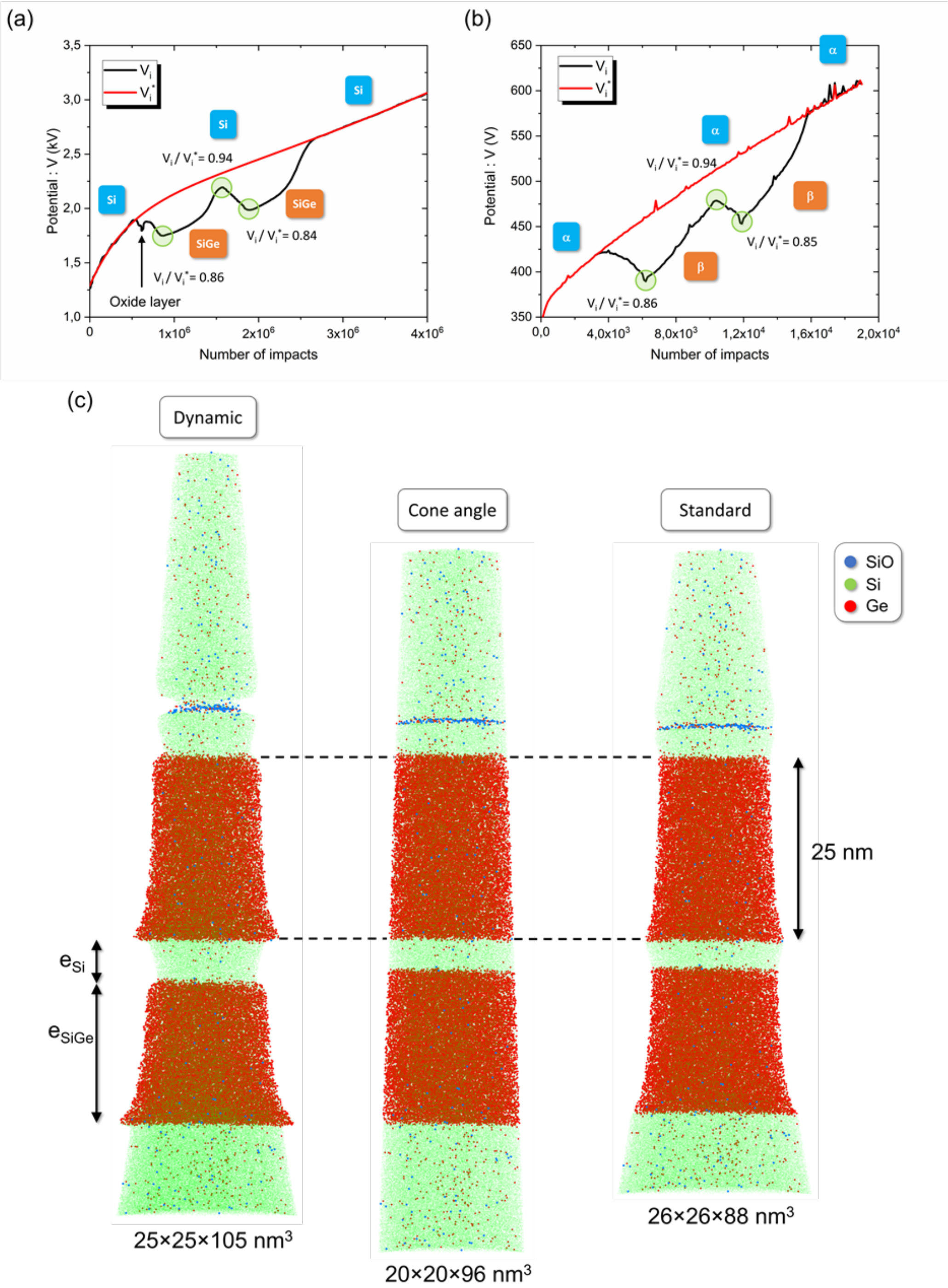

Figure 16 Example of a dynamic reconstruction procedure applied to a specimen composed of different layers of materials having significant differences in field evaporation constants. (a) Experimental voltage curve evolution during the analysis of the specimen. (b) The system was modelled by a simplified field evaporation model assuming rotational symmetry. The simulated voltage curve was compared to the experimental one to assess the evolving field factor and ICF during the analysis. (c) The dynamic reconstruction is compared to standards reconstruction procedures. The dimensions e_{Si} and eSiGe were significantly improved by the dynamic reconstruction algorithm.

Most of the image projection is governed by the specimen's end shape, thus an accurate understanding of this shape can enable reconstructions with less distortion. Having the capability to rapidly model the image transfer function of the instrument as a function of the presence of phases or materials is mandatory in this approach. By expanding previous approaches for homogeneous materials, Hatzoglou et al. showed that it was possible to estimate the evolution of the reconstruction parameters throughout the APT specimen field evaporation for multi-layered structures using simplified field evaporation simulations [215]. The model assumes a three-dimensional geometry with rotational symmetry. Accounting for the evolution of these factors in the reconstruction protocol significantly improves the reconstruction accuracy, Figure 16. This work demonstrates that the evolution of reconstruction parameters can be predicted by field evaporation simulation, provided prior knowledge of the analysed microstructure (for example the layer thickness). Application of dynamic reconstruction protocols to experimental data leads to better reconstructed shape, interface, and thickness in comparison with current reconstruction protocols. The results represent an important step towards a more precise APT analysis of multilayered systems which is important to understand their complex physics and emergent interface phenomena.

Note that the interfaces between layers must be perpendicular to the specimen’s main axis. This dynamic reconstruction is not adapted to tilted layers [305]. To improve the method, the full 3D morphology of the specimen must be considered. For this reason, but also for the sake of saving computing time, 3D models with mean field definition of the specimen surface were developed (mesoscopic scale). Mesoscopic models assume an evolving sample surface with a defined curvature whose evolution is simulated as a function of time. Mesoscopic FE models were first developed by Haley and co-workers using level set approaches, and over time improved to incorporate the realistic impact of the surface electric field [278,302,306]. Alternative approaches using specimen surface meshing were proposed. For instance, Hatzoglou et al. proposed an approach to simulate FE at a mesoscopic scale (nm to µm) by discretizing the evolving sample surface as a triangulated surface mesh [307]. The evaporation sequence is simulated by estimating the evaporation rate of all the mesh primitives (vertices and facets of the triangles supporting the mesh). The physical process of the FE is injected using a continuous model of FE, that is parameterized to handle the local composition and structure of the material and the local temperature.

Results of these simulations are presented for microstructures commonly analysed by APT and compared to experiments, as in Figure 17 with a precipitate embedded in a homogeneous matrix. This broadly demonstrates the validity and the relevance of this FE model at the mesoscopic scale. The model accurately solves the electric field at the surface and the ion trajectory from the specimen to the detector. Given its performance in computing time and memory allocation, this model could be more generally used as a basis for a 3D reconstruction algorithm [276,307].

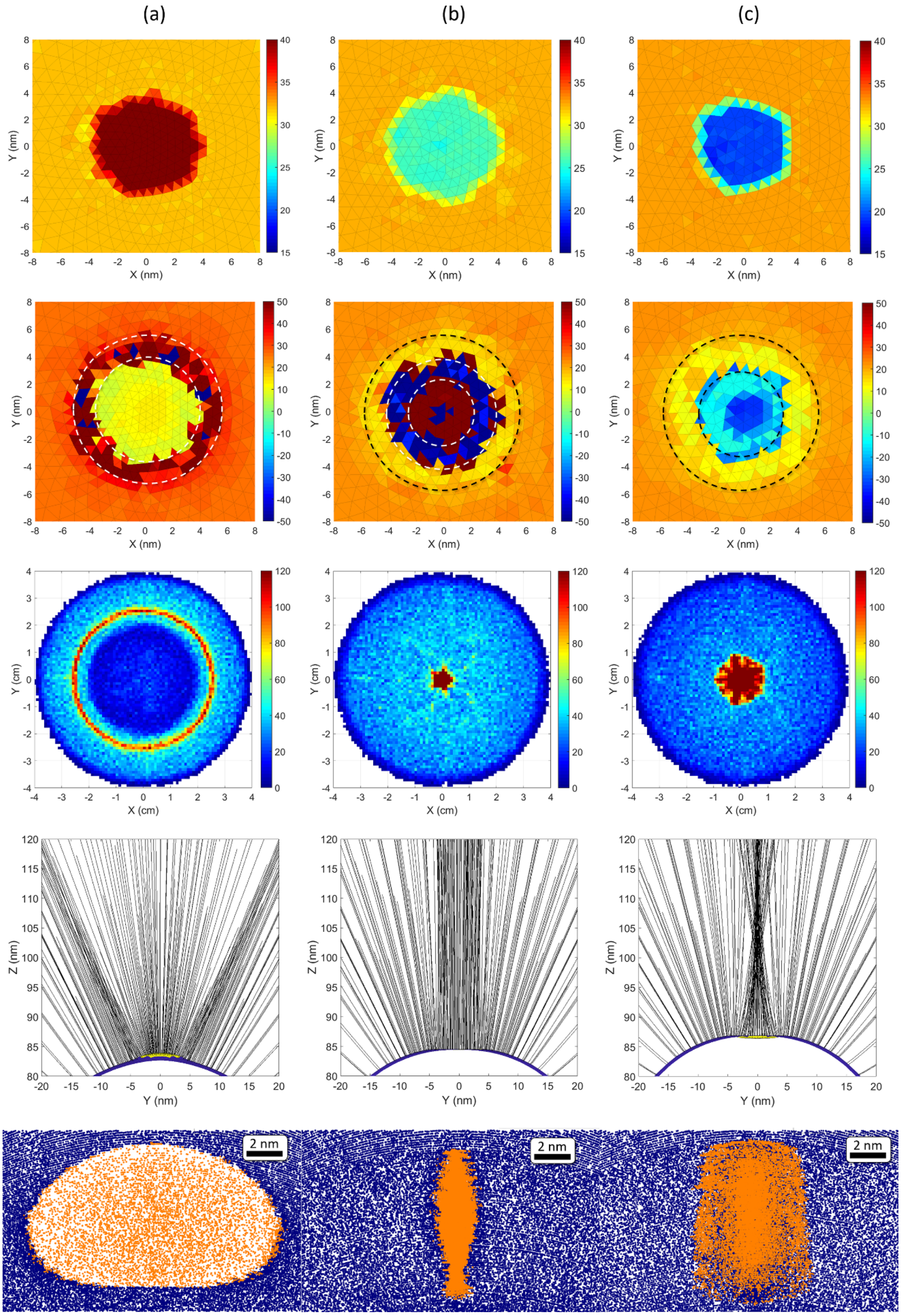

Figure 17 : Modeling the field evaporation of the surface of a specimen with the presence of two phases with different field evaporation constants. (from top to bottom) Electric field ($V\ nm^{-1}$), radius of curvature (nm) at the sample surface (top view), impact density on the detector (number of impact per grid unit area), trajectories from the particle, and the 3D reconstruction (V = 10 nm × 2nm × 17 nm; atoms of matrix in blue and those of the particles in orange), according to its evaporation field FEv,B. (a) FEv,B > FEv,A, (b) FEv,A > FEv,B ⩾ 0.8 × FEv,A and (c) FEv,B < 0.8 × FEv,A with FEv,A the evaporation field of the matrix.

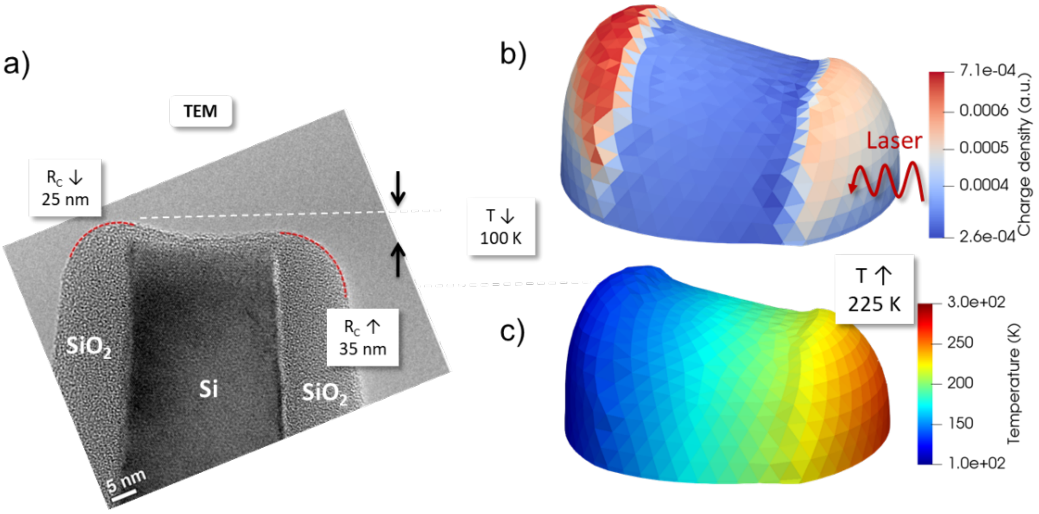

Figure 18 a) TEM image of a SiO_2/Si/SiO_2 trilayer parallel to the specimen axis, analysed in a laser assisted APT. The field evaporation is observed to be highly inhomogeneous, with the Si layer being preferentially field evaporated. A variation of the curvature radius is also observed between the laser illuminated side and the shadow side. b) Mesoscopic modelling of the field evaporation of the same structure assuming a temperature gradient represented in c) between the illuminated side and the shadow side, and a difference of field evaporation of 30 % between Si and SiO_2.

Routine access to such mesoscopic modelling tool is of practical interest for APT analysis of complex microstructures with phases exhibiting drastically different evaporation fields, and/or absorption of the pulsed laser excitation. Figure 18 is an example of a multilayer microstructure composed of SiO_2 and Si aligned with the specimen's main axis and analysed in laser-pulsed APT. Following the analysis, TEM confirms an asymmetrical and complex specimen end shape, Figure 18a. This complex end shape is successfully reproduced by the mesoscopic model assuming strong differences in evaporation fields between phases and a strong inhomogeneous absorption of the laser beam, Figure 18b. The illuminated side reaches a higher peak temperature compared to the shadow side, Figure 18c, as also discussed extensively in the literature [308,309]. Note that 3D modelling is required for specimens without cylindrical symmetry.

5.4 Atomic scale approaches

Approaches described above reach their limits when the scale of objects of interest are close to the atomic scale. The atomic roughness on this scale generates a complex landscape of electric field in the vicinity of the surface that causes deviations of trajectories in the early stages of the flight. These are rapidly amplified by the diverging electric field as discussed above. This atomic scale roughness and the resulting electric field distribution at a distance of a few tenths of a nanometre from the surface creates contrast in field ion micrographs of metals [310]. These electric field conditions are comparable to those in APT, with some additional complexities arising as the atom departs from the surface [272]. Nevertheless, it was shown that a good approximation of the electric field distribution could be derived from a geometric consideration of the surface composed of an assembly of atoms [271].

A quasi-conductive material may be considered as a continuous medium down to the atomic scale, Figure 19a. When the specimen is subjected to a voltage, charges are found to be concentrated on surface atoms. Below the surface, classical solid-state physics states that the electric field rapidly decays within a distance smaller than the size of an atom; the Thomas-

Fermi screening distance is smaller than 0.1 nm in most metals. Only residual oscillatory contributions arise in a few subsequent layers with the application of strong surface electric field. This result is confirmed by quantum calculations. Density functional theory (DFT) predicts that the most protruding atoms concentrate the strongest surface charge [311–313], and are therefore the locations of the highest external field as showcased in Figure 10a [311].

This result justifies the use of calculations or modelling approaches that approximate the atoms constituting the surface by a subatomic scale polyhedral representation, Figure 10b, since the surface charge distributed within a polyhedron produces a field that is strongly dependent on the local surface curvature. Each atom produces its own protrusion above the surface, and so the local field differs strongly from the average field at the surface. Surface atoms may be considered as individual geometrical volumes, which can be as simple as cubes, with charges present on the external facets of these volumes. The field distribution in free space may be calculated assuming the external morphology of the assembly of atoms and solving the Laplace equation by assuming a constant voltage V on the surface. A 3D mesh of voltage nodes fined-grained close to the specimen's surface, and coarse-grained at larger distances, can be used to estimate the entire electric field distribution with good precision. This mesh is used to compute individual ion trajectories travelling from the initial tip surface to the detector. Different mesh symmetries, mesh geometries, boundary approximations, and computational optimizations were developed by different authors for this purpose, and were used to understand the image formation in APT. We refer the reader to Ref. [275] for an overview of the evolution of modelling approaches.

An alternative approach for calculating the electric field distribution in APT uses the electrostatic Robin's equation to directly calculate the charge distribution over the conducting surface of the tip, requiring no knowledge of the surrounding electric field, Figure 10c [284]. The partial ionization state of the surface atoms is at the core of the method. The surface charge is assumed here to be discrete and spread on the positions of every surface atom. The field distribution is retrieved using Coulomb's law, based on the distribution of point charges, without the need for a supporting mesh. The only requirement is a fine scale definition of surface atom positions and the normal direction to the surface at each of these points. The computational efficiency is ensured by an adapted version of the Barnes-Hut N-body problem algorithm. More technical details about the method are in Ref. [284].

Both approaches assume atoms are fixed on a defined 3D structure (which can be a crystal lattice or an amorphous structure) and the impact of physical parameters such as specimen temperature or the presence of species with different evaporation fields strengths can be evaluated. The distribution of the surface electric field, Figure 19a, can be used to evaluate the impact of the atomic structure of the material of interest on the image formation in FIM, Figure 19b, for instance.

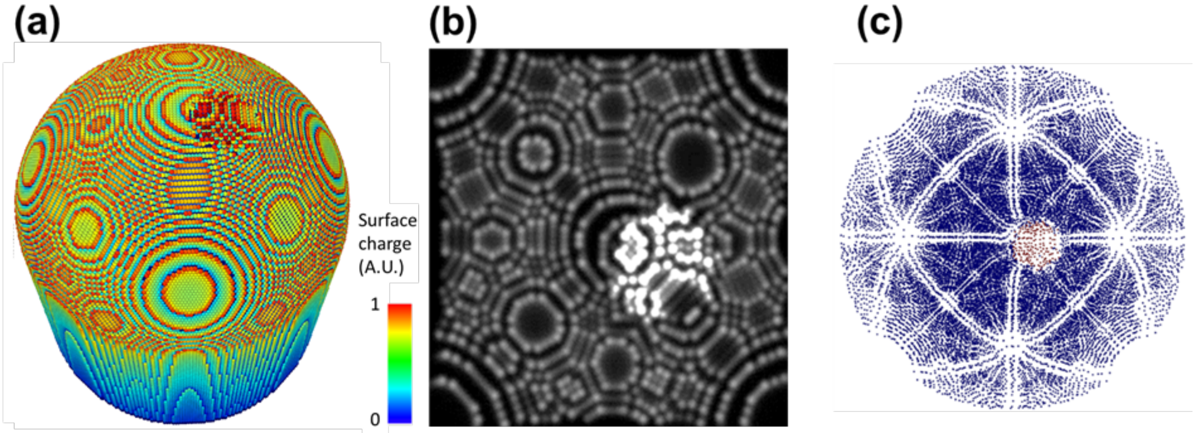

Figure 19 (a) Surface charge (local electric field) of a virtual specimen with an FCC structure with a spherical diamond structure inclusion (field evaporation 20 % higher than the matrix atoms) close to the tip centre. (b) Simulated FIM image, assuming the tunnelling probability and the critical distance of ionization of gas atom. Difference in contrast between phases is uniquely linked to the calculated surface field. (c) Simulated APT hitmap for the evaporation of 3 atomic monolayers on the detectors. Trajectory aberrations of field evaporated atoms are strongly influenced by the charge distribution around evaporated atoms in the first steps of flight (generating zone lines contrast).

Once the potential (or the distribution of surface charges for the initial input structure) has been obtained, the dynamic desorption of atoms is simulated by repetitive execution of three basic steps. First, the algorithm looks for the surface cell which is exposed to the maximum field strength and removes it, i.e. that cell becomes a “vacuum” cell. Different field evaporation thresholds for desorption are considered by appropriate scaling of the surface field. The sequence of evaporation is then deduced by assuming some simple physical law describing the order of evaporation. The simplest one assumes that the sequence is fully deterministic, and the atom under the highest field being the first to be removed. Note that some models use the highest electrostatic force rather than the highest electric field criteria [314].

Second, the potential is recalculated for the new configuration. And third, the ion-trajectory starting from the origin of the removed atom is computed by integration of Newton´s equation of motion. Each evaporated atom produces an impact position on a virtual detector that is recorded. This procedure is applied sequentially, which results in a dataset comparable to an experimental dataset that can be processed and reconstructed using similar protocols for direct comparison.

Most of the artefacts observed experimentally in reconstructed APT datasets are well reproduced using models that assume the electric field distribution with electrostatic approximations on a field emitter [236,290,315]. To understand how the electric field may affect the surface atoms, and the way the specimen is eroded during an APT analysis, it is important to determine how the electric field is generated locally. Therefore, the exact relationship between the curvature at the atomic scale and this field (which results simply from the distribution of surface charges) must be evaluated. This distribution is a key parameter to understand the regularity of the surface erosion by field evaporation of atoms.

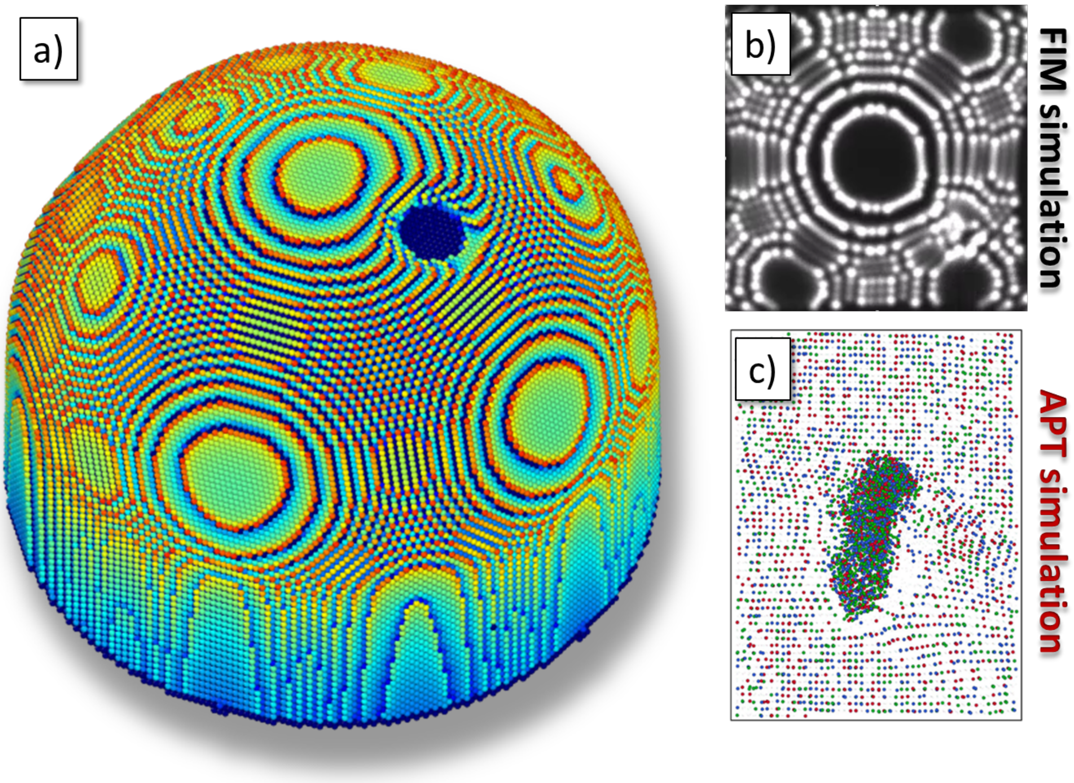

Figure 20 Field evaporation simulation of a nanocavity in a metallic alloy. The simulation reproduces the APT analysis of a NiCrAl medium-entropy alloy containing nano-sized He bubbles. The sample used for this study was the NiCoCr medium-entropy alloy containing nano-sized He bubbles surrounded by a shell enriched in Co and Ni. a) Snapshot of the tip surface with representation of the local surface electric field with a color map (red: highest electric field blue: low electric field). b) Simulation of a FIM image of the surface with the presence in the bottom right of a blurring feature induced by the focusing effects of the nanovoid intercepting the tip surface. c) Simulated reconstruction of the distribution of Co, Ni and Cr (Co in green, Ni in red, Cr in blue) including a shell with low evaporation field compared to the matrix.

The compromise of these models is to consider the sample being un-deformed, and non-perturbed between the removals of two successive surface atoms. This hypothesis is supported by the conditions used experimentally during an APT experiment. The specimen is held at a temperature in the range 20 K–80 K. From a classical point of view, atoms are 'frozen', and atomic movements are limited.

An example of a simulation provided to understand image artefacts in the analysis of nanovoids is presented in Figure 20. The simulation reproduces the APT analysis of a NiCoCr medium-entropy alloy containing nano-sized He bubbles [316]. These bubbles were first identified by STEM performed on the APT specimen. Based on high angle annular dark field images taken at different rotation angles, the size and coordinates of the bubbles were accurately determined. Point density differences within the reconstructed APT data could be directly correlated to the He bubbles found in the STEM images. The simulation gives access to the morphology evolution of the sample as the specimen's surface is field evaporated, as well as the deformation in image projection even in the case of nanoscale features. In the example, the shell of the nanovoids is enriched in Co and Ni and is focused on the core of the void position, giving rise to artificial enhancement of the local point density in the reconstructed APT datasets.

The model was used successfully in various systems. Thus, the correct input of the field distribution after each evaporated atom should improve APT reconstructions. The access to the atomic level is thus of fundamental interest to keep pushing the spatial precision of APT measurements. APT is known for its excellent reconstruction performance in depth (z), which is linked to the regular and controlled field evaporation sequence of the specimen. The influence of an ‘ideal’ order of field evaporation, as it may be expected in APT image reconstruction, was demonstrated using a purely geometrical model with atoms with the same evaporation field [136,267]. In the model, the surface is seen to be eroded atom after atom assuming the chosen atom to be field evaporated is always the most protruding atom of the surface. Any protrusion at the surface enhances the local field, and electrostatics predicts that the field increases proportionally to the degree of protrusion [317]. Degradation of the depth precision occurs when this ideal order is perturbated. This is the case when higher base or laser pulse temperatures are used [318]. These are even more critical as the relatively recent extension of APT to non-metallic materials mostly employs laser pulsing [19]. There are additional aspects that further increase the complexity of mechanisms that must be considered to understand the image formation [319]. This was experimentally and theoretically demonstrated by different authors [12,311,320,321].

Increases in temperature make the choice of the atom to be field evaporated less field dependent and more stochastic [318]. The variation of local binding energy may also influence the evaporation of surface atoms during the imaging process. This was pointed out by Gault and co-workers when they measured a dependency of the depth resolution as a function of the crystallographic direction [137]. The evaporation field may vary from place to place across the surface even for pure materials [322], thus changing the evaporation order. In alloys, and especially disordered alloys, the presence of elements with different evaporation fields along with the presence atomic defects modify the perfect sequence of field evaporation and the depth precision of reconstruction.

An example is presented in Figure 21 when a small quantity of Re is inserted in a matrix of heavily deformed Ni with a large quantity of dislocations and vacancies. The simulation demonstrated that the final reconstruction is perturbed, inducing spatial deviations of several fractions of a nanometer. Models must describe how the atomic surface evolves under the presence of a high electric field, which depends on the local roughness at the atomic scale and between the successive evaporation of two atoms. We may note that assuming atoms remain at rigid positions on the surface is sufficient only if spontaneous field evaporation of atoms is involved. Nevertheless, the impact of the local arrangement of atoms, underpinning the local electric field, and the influence of the stochastic nature of the field evaporation process are important aspects of the most recent models developed to mimic the erosion of alloys.

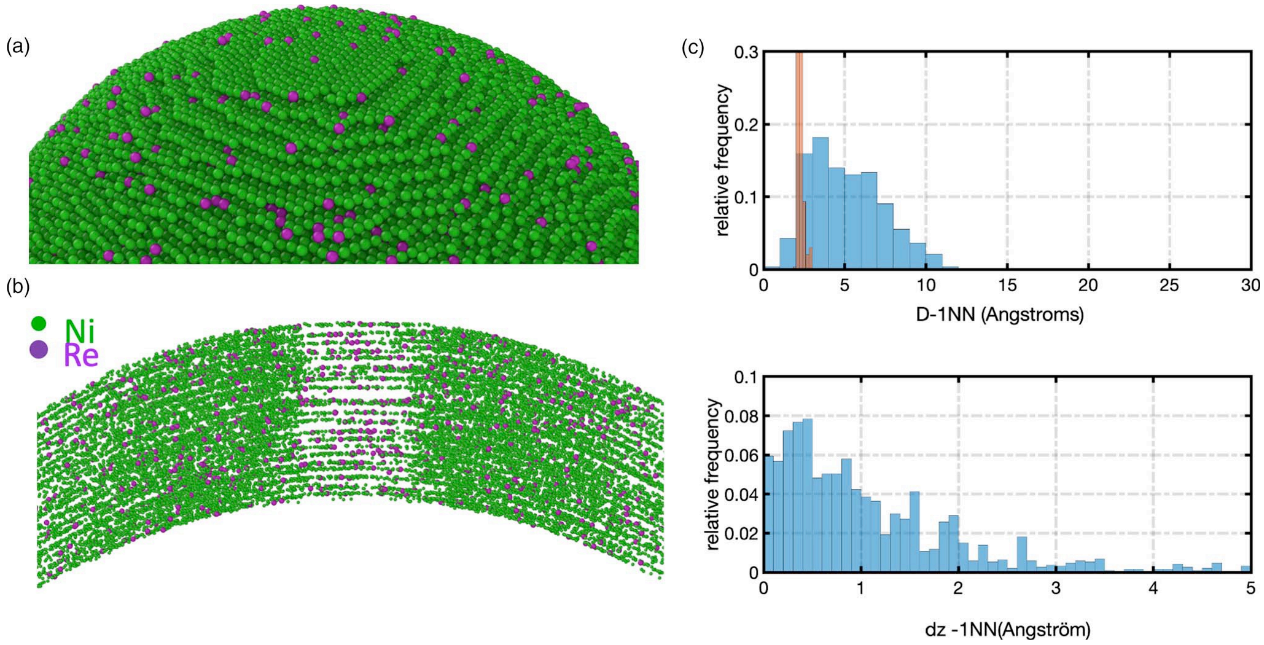

Figure 21 Simulation cell with Re segregated to atomic defects (stacking faults) in the Nickel lattice. (b) Thin slice though the reconstructed simulated data showing the in-depth degradation of the spatial precision after field evaporation. (c) D-1NN (distance to the first nearest neighbors in the same plane) and dz-1NN (distance to the nearest neighbors out of plane) for Re atoms initially on the same plane in the input data in orange and in the simulated and reconstructed data in blue.

Understanding the degradation of spatial precision in the analysis of alloys by APT is of fundamental importance, since local short or medium range order of atoms in complex alloys can enhance mechanical properties. The deterioration of the spatial accuracy in alloys composed of multiple species, each with an individual evaporation field (such as high entropy alloys [300]) make quantifying short range order parameters from APT extremely challenging. Recent studies highlight these difficulties using even the most favourable experimental conditions in metals (e.g. low temperature analyse, voltage pulse, reduced evaporation rate) [234,323,324]. This difficulty is inherent to the physics of field evaporation of complex multicomponent systems, as it was demonstrated by simulation. For instance, simulating the field evaporation of alloys composed of 4 different atoms having ranges of field evaporation constants ±5 %, ±10 %, and ±20 % between elements, the spatial precision in atom positioning was found to be degraded both in depth and laterally. The FWHM of the in-depth reconstruction changes substantially, increasing from approximately 0.04 nm to 0.075 nm whereas the lateral positioning precision is degraded up 0.1 nm to 1.2 nm, as the range of evaporation field increases [325]. The precision of the measurement worsens with the compositional complexity, with a clear mixing of nearest-neighbour positions. Notably, the depth resolution is also affected [136], but remains more robust against a spread in evaporation fields, thereby enabling the opportunity to quantify short-range ordering in compositionally complex alloys along the z direction [326,327].

5.5 Molecular dynamics approaches

Previous atomic-scale field evaporation simulations intrinsically assume that atoms are fixed onto their crystallographic lattice inside the specimen until the electrostatic field reaches the critical value for field evaporation. Nevertheless, a few experimental cases have shown that some atomic species could move prior to observed field evaporation. For example, it was found in a FeSi alloy with Si in solid solution that Si atoms may migrate short distances on the surface following receding step edges on low index (011) planes [328]. This was also observed in more detail by Gault and co-workers in steels containing a low amount of non-metallic solutes (e.g. C,N,P and Si) [329]. This movement was found to be weakly dependent on the analysis temperature. A thermally activated migration process is possible, as observed in FIM operating at high temperature [330], but it was supposed to be driven by a chemical or relaxation process occurring when a significant difference in field evaporation exists between matrix atoms and solute atoms. It was suggested by Gault and co-worker that this phenomenon is field gradient triggered, as solutes migrate toward high electric field regions on the specimen surface. These solutes often form homo- or hetero- species molecular ions to facilitate their departure from the surface.

To integrate these movements that occur between successive evaporation, several molecular dynamics model (MD) were developed concurrently. The “athermal” movement of atoms implies integration of the relaxation of the atomic surface under the high stress that induces spontaneous displacement of atoms, with a very low to null energy barrier. The relaxation is induced here by the electrostatic forces existing between partially charged atoms on the surface. These must hence be included in models. Note that correct models should consider “pre-evaporation” effects such as atomic surface diffusion and global specimen deformation induced by electrostatic pressure [331,332] as well as “post-evaporation” effects such as atomic relaxation. For instance, it was observed by Tsong & Walco [333] that an electric field gradient may generate a directional random walk by reducing the energy barrier for surface diffusion. Short diffusional jumps are thus also influenced by local electric fields and local polarisation effects.

These processes can be simulated by molecular dynamics (MD). In addition to the standard interatomic interactions, the interaction between charged surface atoms and the electric field must be included, as well as the Coulomb interaction between the partially charged atoms. In this approach, the surface charge and field are calculated via solution of the Laplace equation around the surface features and utilizing Gauss' law to calculate a corresponding partial charge on each atom exposed to the electric field. Parviainen et al. proposed models combining molecular dynamic approaches with field evaporation models [334], and then at a later stage combined with the Robin-Rolland model described above to account for the surface charges [335]. By dynamically calculating the induced charge on surface atoms (corresponding to a given applied external electric field), the force resulting from the interaction between the electric field and the charged atom is then added to the classical interatomic interactions included in classical molecular dynamics. Thus, it is possible to use the technique to simulate any metallic sample for which a suitable MD interatomic potential exists.

This extension of MD enables the study of the effects outlined above. For instance It was shown that adatom migration of W on W is modified in the presence of an electric field, in good agreement with experimental observations [336]. Results show that in the presence of an external electric field, adatom migration can be enhanced by almost an order of magnitude on a W sample. The electric field indeed pulls the migrating atom away from the surface, weakening the interaction with the other surface atoms, and allowing it to move more freely on the surface. The calculated surface diffusion coefficient increases with increasing field, Figure 22A. However, once the field is sufficiently strong, it will trigger field evaporation instead of migration. It was also observed how the removal of one or more surface atoms alters the local electric field, making it difficult to interpret experimental sequences of FIM images, Figure 22B [257]. It was also shown that the diffusion coefficient increases with time, as the migrating atoms drift towards edges where the local electric field is enhanced due to geometric effects. The presence of an adatom will further increase the field enhancement near a ledge, raising the probability of atoms from a lower plane climbing up the ledge, or triggering the evaporation of the ad-atom and nearby atoms, Figure 22C.

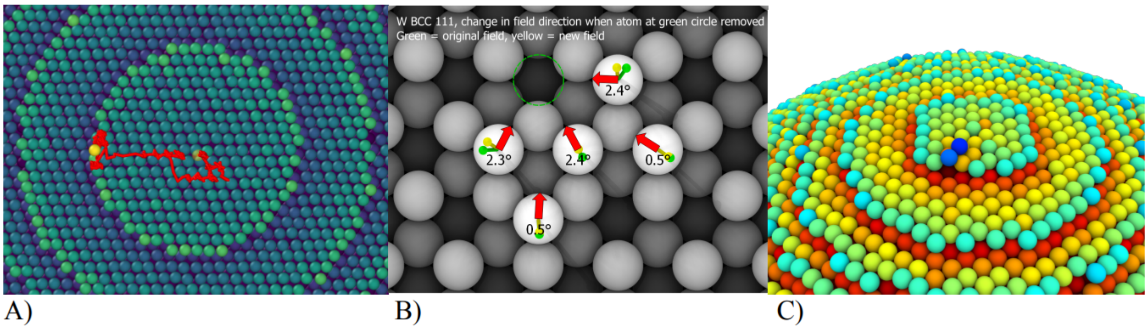

Figure 22: A) Simulated migration path of a W atom on a W sample surface under a high electric field. Due to geometric field enhancement the field is higher at the edge, leading to a directed migration. B) Calculated change in the local electric field when one atom is removed from a W {111} surface. The change in the direction is several degrees, which affects the trajectories of any evaporating atoms. C) A migrating W atom enables another W atom to climb up a ledge an a simulated W sample (Figure and caption from [336]).

To provide some perspective, with this enhanced MD it is possible to model accurately and efficiently and the dynamic evolution of the specimen shape as well as the distribution of the electric field at atomic resolution. The shape and local field are tightly coupled together, forming almost a feedback loop: an increase in the specimen local curvature can locally increase the electric field, which in turn affects the shape of the tip via additional forces exerted by the field at the surface that can facilitate surface diffusion. Such an implementation of MD is needed to understand the morphological changes that may occur and that affect the obtained tomographic data.

In addition to modelling dynamic processes, molecular dynamics also has another advantage in that while integrating the atomic trajectories, information about the binding energy of each atom also becomes available. This binding energy can be used to estimate the evaporation probability for individual atoms more accurately than simply looking at the local electric field strength and comparing them with pre-tabulated critical evaporation field values. This approach is more flexible, as it makes no assumptions about the crystal structure, number of neighboring atoms, or other factors that affect the critical evaporation field. It is also possible to estimate the critical evaporation field directly by observing the value of the local electric field that is sufficient to break the bonds between an atom and the rest of the surface.

Such simulations are also necessary to interpret the apparent in-depth displacement of some specific species in pure matrix (the simulated case in this last reference was Cu in Al). Some experimental evidences of retention of B atoms in Si over several atomic layers were observed in laser assisted field evaporation of B-doped Si [337], and similar observations were reported in Fe-based materials [338]. Such large-scale movements imply physical retention/surface diffusion mechanisms at the tip surface that take place at high laser pulse energies.

Finally, in non-metallic alloys the problem can be even more complex, since electric charges redistribute in a complex way depending on the chemical nature of the atoms. For instance, the field evaporated surface of stochiometric MgO was observed to be more rough than the same surface before running APT in laser mode at low intensity illumination [339]. This phenomenon was also attributed to photoionization effect, when the absorption of a photon by surface atoms may cause direct field evaporation, and therefore less driven by the electrostatic field. In semiconductors or insulators, field evaporation assisted by laser pulses appear to be more complex than classical field evaporation in metals. In oxidized Fe and Zr, the presence of unexpected layers of oxides is interpreted by field induced in-depth diffusion and oxidation at the nanoscale [340]. It was also pointed out that residual internal electric field could be the source of field driven diffusion during the field evaporation process of species with high ionic conduction such as Li-doped silicate and borate glasses [341] or oxides for Li-ion battery cathodes [176]. Under measurement conditions in laser-pulsed APT, the mobile Li ions are redistributed in response to high electric fields. As a consequence, the direct interpretation of the Li-distribution is significantly uncertain. Understanding and modeling these processes will enable improvement in APT's analytical performance for such challenging materials.

5.6 Density Functional Theory approaches

The charge redistribution associated with thermal or athermal relaxation of the surface structure is obviously out of the reach of conventional MD approaches since the chemical and the collective nature of the electrons at the specimen surface must be considered. Most advanced treatments use density functional theory (DFT) to calculate at the atomic scale how electron density redistributes when a sheet of materials is biased to a constant voltage [312,342]. These models, which reproduce the atomistic surface of the material, ought to give reliable results in both metals and non-metals. To simplify the problem, several ways of computation have been pursued.

The very first models used a 1D approximation for the substrate using a jellium structure [313]. The effects of a strong positive electric field on the surface geometry of a smooth metal single crystal surface were presented in the early eighties. The results were explained in terms of a simple analytical model depicting field evaporation differently from the established empirical models [343]. With this approach, it was pointed out the possible role of field induced reconstruction, in particular for determining the critical field for stripping the surface layer of atoms. The field evaporation was considered for a full atomic layer of atoms in 1D. However, this model was too crude to be compared with realistic experimental data because of the real atom-by-atom nature of the process and because of the three-dimensional nature of the atomic surface.

Field evaporation simulations based on quantum mechanical calculations including real three-dimensional nature of the surface were later introduced [281,344–357]. 3D field evaporation simulations were reported on different pure materials (e.g. Al, Si, Mo, W) under three-dimensional periodic boundary conditions, or on small clusters of atoms for some compounds (e.g. AlSc, ZnO, MgO…). More recent approaches take into account the local reconstruction of the surface under the electrostatic stress during the field evaporation process [358–360]. In these recent studies using different numerical models, the local interaction of an atom with its neighbors and the collective behavior of surface atoms during field evaporation was shown to play a great role in the energetics of the process. This is especially true under the relatively low electric field conditions relevant to laser-pulsed excitation or low evaporation rate in voltage mode. An example is the atom of interest rolling up above the surface atoms before departure, which involves a local displacement and provides transverse velocity [347]. This roll-up perturbates the atom trajectory in the first step of flight and influences the energetics of the field evaporation process [281,355,357].

As an example shown by Ashton et al. [357], Figure 22, the field dependence of the activation energy for evaporation events for W, in agreement with experimental measurements, do not follow the behavior predicted by earlier theoretical models. These models generally assume an ideal straight-line departure of the ion from the surface [21,23]. The field evaporation mechanism is effectively a two-stage process: first a roll-up event, followed by the actual departure from the surface. Each of the two stages has its own respective energy barrier. The roll-up can be understood as a competition between the force of the evaporating atom's nearest neighbor bonds and the force of the field tugging on the ion. Classical models predict unphysically high barriers with fields lower than the evaporation field [361].

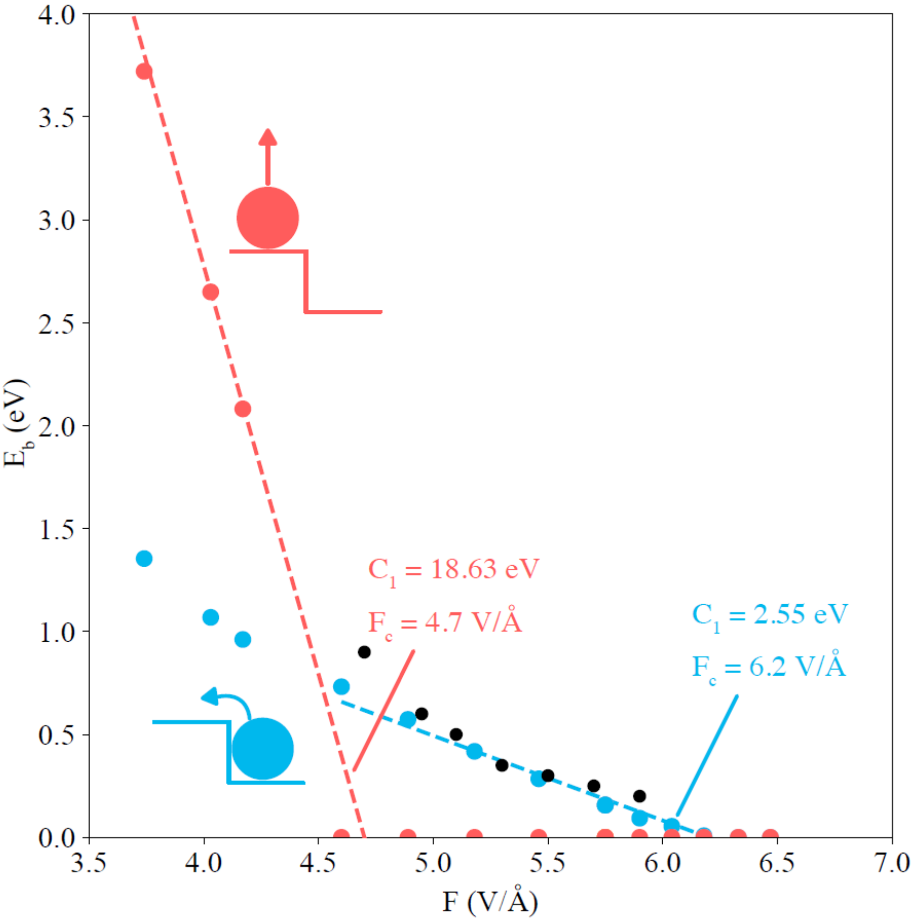

Figure 23 Energetic barriers as a function of applied electric field for a W atom on top of a W slab. To mimic a step-like structure, the slab is oriented in the <10 8 1> direction, and one kink atom was considered. The barrier to the initial rollover motion (blue) and the barrier to evaporation from the adatom site (red) are plotted separately. Experimental data previously reported for tungsten are shown in black [361]. Image from Ashton et al. [359]

5.7 Perspective

These recent models highlight the necessity to simultaneously describe the charge redistribution at the specimen's surface, the local arrangement of atoms around the atom of interest, and the collective motion of atoms in the process of field evaporation. These three aspects are all necessary to correctly capture the physical parameters for each atom including the threshold electrostatic field to trigger field evaporation, the sensitivity to this field, the initial position, the kinetic energy of the expelled ion, and the reconstruction of the surface after the process. Note that the collective nature of the process and the persistent interaction between the evaporating atom and its nearest neighbors is likely responsible for the substantial number of spatially correlated co-evaporation events experimentally observed [256].

The atomic-scale field evaporation mechanism is therefore an important piece of the theory of APT. The success of DFT to provide a realistic picture of the field evaporation process, compared to former phenomenological descriptions, offers us a new way to guide the interpretation and design new experiments. The evidence provided in these studies is essential for accurately controlling and interpreting APT on various systems and pushing performance of the instrument to its ultimate boundaries. However, since DFT can only be applied on system composed of a up to a few tens or hundreds of atoms, it alone is unable to provide a complete picture of an APT specimen. Multiscale simulations integrating from DFT to MD to FEM/BEM models must be developed to provide a full description of APT in the future.

6 Analytical performance

For many aspects of APT, there are no standard ways to assess the elemental or spatial resolution, even if some attempts have been reported across the literature. In the following, we focus on the main concepts that limit the performance, both from in terms of compositional and spatial analyses. It is important to state once again that many of the limitations arise from the physics of the field evaporation process and only moderately from the instrument itself – if we exclude the detector efficiency.

6.1 Compositional analysis

Conventional mass spectrometry techniques, including SIMS, analyse billions and billions of ions. In comparison, APT analyses contain tens to hundreds of millions of ions. This can limit the sensitivity of APT and the precision of the composition reported. In recent years, some metrics have been proposed to quantify its sensitivity [26], yet once again, there is no wide community adoption. The mass resolution of APT used to be defined by measuring the full width at half or tenth maximum of a peak within the mass spectrum. In most cases using modern instruments, peaks are sufficiently narrow to avoid overlaps at half-maximum and even at tenth maximum. The width of mass peaks can be related to the precision of voltage and the flight distance measurements, as well as that of the time-of-flight. This is rarely a relevant information to assess the compositional sensitivity of the technique. What limits the accuracy of the compositional analysis is more often the presence of background, the relative signal-to-background ratio, and whether the difference between peaks and background is statistically significant.

6.1.1 Origins of the background

There are two main sources of background. First, the MCPs that are used on the entry face of the particle-detector to convert an ionic impact into a detectable electron signal have a “dark current”, i.e. a discharge that can be related to asperities on their surface or ionisation of residual gases in their vicinity. This leads to a few counts per second per square centimetre of the MCPs. The second source of background is the detection of ions that depart in between pulses, and whose time-of-flight cannot be recorded appropriately as a consequence. These can be either from field ionisation of residual gases from the chamber or from the field desorption of surface species, i.e. adsorbed atoms or molecules from the residual gas or the field evaporation of surface atoms because the amplitude of the DC field is sufficient to cause their departure.

At this point, let us go back to some considerations regarding the probability of field evaporation. The field evaporation rate follows an Arrhenius-type law, whereby the electric field lowers an activation barrier and atoms field evaporate through a thermally-assisted process [23]. To a first approximation, at field close to the field evaporation threshold, one can consider that the field necessary to reach a certain evaporation rate ϕ varies linearly with the temperature at which the field evaporation occurs [362]. This variation is schematically depicted in Figure 24a. The region shaded in orange is a network of curves for a range of evaporation rates. Experimentally, the field can be adjusted via the voltage, and the base temperature can be selected as one of the data acquisition parameters. To maximise the level of control over the field evaporation process, conditions should be selected that correspond to the blue circle: without pulsing the field (i.e. voltage pulsing) or the temperature (i.e. laser pulsing), no significant field evaporation takes place. This will limit the measured background level.

Under conditions indicated by the crossing of the dashed grey curves, a measurable rate of field evaporated ions will be generated. Indeed, the field evaporation of an atom uncorrelated to a pulse does not allow for a measurement of the time-of-flight, and field evaporation at the DC field can take place at any time leading to a level of “white” noise across the mass spectrum. The conversion of the time-of-flight into a mass-to-charge ratio is defined by a quadratic relationship, making this random time-independent background appear as a slow decaying signal with increasing mass-to-charge ratio in the mass spectrum. These are indicated by the regions shaded in green (low background) and red (high background) in Figure 24b.

Importantly, because the evaporation field varies with the considered species, both the position and slope of this network of curves depends on the considered species. This is shown in Figure 10a as a second network of curves in blue. Controlling the conditions can then become much more complex, as too high a DC field can lead to the so-called “preferential” field evaporation of the species with the lowest evaporation field or the retention on the surface of the species of the highest evaporation field [328]. Either way, this can have consequences on the analysis, with the former being more problematic from a compositional standpoint as it leads to the loss of the species with the lowest evaporation field. Much remains unknown as to how to estimate evaporation fields for each species in an alloys, since variation from local atomic neighbourhoods can be expected [363] including for a single species across two different phases for instance [364].

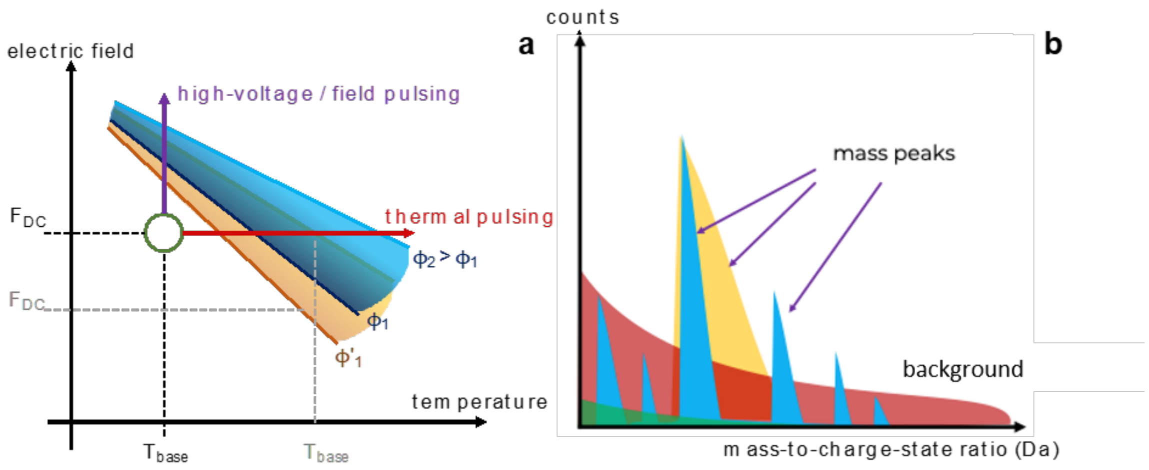

Figure 24: (a) Networks of curves of the variations of the electric field necessary to cause field evaporation at different rates as a function of the specimen's base temperature. The pulsing modes are indicated by arrows, along with possible sets of analysis conditions, and for two different elements. (b) cartoon view of a section of a mass spectrum, showing two levels of background in red and green, (modified from [202]).

6.1.2 Origins of the peak shape

The shape of the peaks is related to the distribution of the times-of-flight for ions of a given mass-to-charge. In voltage pulsing mode, there is a distribution in the energy of the emitted ions with the appearance of so-called energy-deficits associated with the fact that not all ions are emitted strictly on the top of the pulse. Hence, some are not accelerated by the exact same potential. This leads to a spread in the ions' energy and numerous ions with longer times-of-flight that form the tail of the mass peaks.

In laser pulsing mode, all ions are accelerated by the same DC voltage, and they hence have the same energy. However, there can be a delay in the emission of the ions caused by the duration of the thermal pulse that depends on the material's thermal diffusivity as well as on the geometry of the specimen [365,366]. These lead to potentially long tails of the mass peaks that can overlap to form a higher level of background locally. Possible differences are indicated in the schematic in Figure 24b, with the yellow mass peak showing a slower decay than the peak for the same species in blue.

The presence of these tails, notwithstanding their origins, can affect the accuracy of the measured mass and create overlap with peaks pertaining to other isotopes or elements. On average, the use of reflectron-fitted instruments will help reduce these tails. This occurs in high-voltage pulsing mode by focusing the ions "in time", meaning that the reflectron equates the time-of-flight of ions with the same mass-to-charge but different kinetic energies by making ions with more energy travel over a longer path. It works in laser pulsing mode by increasing the flight distance and hence time-of-flight making the relative measurement error relatively smaller.

6.2 Role of the detector

There are several factors related to the detector itself that can limit the detection of a species.

The biases used on the MCPs are selected to make them insensitive to the energy of the incoming ions – at least above a certain threshold (typically 2 kV). The amplitude of the electronic signal generated should be the same for light and heavy ions regardless of the charge state. Data acquired at too low voltages, may however have species-specific losses.

Additional losses can originate from the dissociation of molecular ions that lead to the formation of low-energy ions or neutral atoms or molecules. Depending on where along the ion flight the dissociative event occurs, the daughter ions may not have been accelerated sufficiently to trigger a detectable signal[265]. During dissociation, daughter ions may not acquire the energy that is necessary to make the time-of-flight of these ions close enough to other ions from the same species, making it impossible to associate them to a specific range. These aspects are typically revealed by using Saxey's approach of a correlation histogram[261].

For data acquired at higher voltages, the main issue is the capacity for the detector to process multiple ions emitted by a single pulse striking the detector. If ions are separated by a sufficient distance or a sufficient time, there is normally no issue. The critical distance and time depend on the specific detector, its configuration, and the processing of the signals [16,49,50]. For modern commercial instruments when an ion strikes the detector it creates a "dead area" over a certain duration, typically a few ns, which then propagates over time over the entire surface of the detector [51]. A second ion striking the detector during that time or in that region has a higher chance of being lost, which is referred to as the pile-up effect [367]. The shape of the dead area, once again, depends on the detector itself and can be characterised by looking at materials such as carbides with high rates of multiple events [52]. Species-specific losses arising from such mechanisms have been reported in the case of C [52,368,369] and B[51,370].

6.3 Performance and optimisation

Sensitivities as low as 10 atomic parts-per-million have been quoted in the past [37,371]. This is not universal for any element in any specimen. The actual sensitivity in a given experiment depends on the specimen, material, and element of interest as well as the local background, both time dependent and time independent. For instance, at a given level of background more atoms of an element with multiple isotopes (say, Sn) will be required to be detected compared to monoisotopic elements (say, Al or Co). In addition, due to the varying level of background vs. mass-to-charge, but also the wider peaks and hence worse mass resolution at higher mass-to-charge, quoting a single number for the performance of APT is nearly impossible and, to be perfectly honest, meaningless.

There is a significant sensitivity of the analytical performance based on the selection of experimental parameters, particularly the balance between the base temperature and the electric field. The latter can be adjusted via the target detection rate. One should aim to maximise the electric field while minimising the level of background. A higher background can hinder the detection of peaks from minor elements, whereas a higher field normally offers better control over the sequence of field evaporation. Higher fields yield higher spatial resolution yet can facilitate preferential evaporation and lead to species-specific losses[328,372,373] as well as an increase in the number of multiple events, and hence possible losses from detector pile-up. Optimising parameters will help with balancing these antagonistic aspects, but the "perfect" data does not exist.

6.4 Spatial performance

APT data representation being based on a point cloud gives a misleading impression of infinite precision in the reconstructed atomic positions. Errors on the measured distances or size are rarely considered or displayed on composition profiles, in contrast with statistical error estimations on the measured composition. This section provides perspective on the spatial precision achievable by APT. Ultimately, it should be noted that the problem of the resolution of APT is not so much that an object below the quoted resolution cannot be imaged, i.e. the atoms constituting that particle will be ionised and detected with the same probability as those form the surrounding matrix. The key issue is that the measurement of its composition will be inaccurate since mixed with atoms from the matrix.

6.4.1 For single phase materials

Conversely to most conventional microscopy techniques where the optical system and the source are decoupled, in APT the main projection optic is the emitting specimen itself. This makes the resolution dependent the individual specimen and strictly speaking not even constant over the course of a single analysis. The resolution limit arises from trajectory aberrations associated with the distribution of the electrostatic field at the near-atomic scale, which depends on the local atomic organisation on the surface [374]. This has been extensively studied by finite-element simulations [275] that have shown how the local distribution of the field can push the departing atom sideways compared to what would be expected from a straight projection. In addition, local gradients in field can drive migration of the partially charged atom onto its neighbours on the surface, prior to departure. These motions are referred to as roll-up and have been studied experimentally [272,347,362]. In recent years, insights from density-functional theory calculations have come in support to these processes [351,357]. These roll-ups push the departure position away from the original's atom position inside the material, further degrading the spatial resolution. For the most part, these effects are related to the high fields that are necessary to perform APT analysis and cannot be avoided.

Following departure from the surface ions follow trajectories that depend on the distribution of the electrostatic potential inside the microscope, and depend on the specimen's curvature and global shape [207,213]. Ultimately, notwithstanding the actual trajectories, the ion's projection can be well described by a range of projection laws [208,209,375] (provided that the parameters are adjusted for each specimen) [212], and to some extent, the analysis conditions [376]. Unfortunately, these parameters also change during the course of an experiment since the specimen is being eroded and the radius progressively increases, as supported by measurements [214]. There are still debates as to what projection model to use [209]. These projection models assume cylindrical symmetry and an isotropic magnification, and as such reflect the main features of the projection but cannot account for the details of the trajectory of each individual ion.

These effects all combine to offset the positions of the atoms in the reconstructed data, resulting in a limited spatial resolution that depends on the species considered. It is important to note that these aberrations primarily affect the lateral position of the atoms, more so than the depth since that is calculated based on the sequence of detection of the ions primarily. Most attempts to quantify the spatial resolution were on pure metals. For the depth resolution, the spacing of the reconstructed atomic planes was considered the appropriate metric, and was measured using spatial distribution maps or Fourier transforms [137,268,377,378] This method leads to depth resolutions reported down to 20 pm[379] for Al and 60 pm[268] for W. Lateral resolutions in the range of 200 pm were reported by analysing the evolution of the depth resolution from Fourier transforms spatial distribution maps as the analysis volume is tilted [137,268,269]. The elephant in the room in this latter case is evidenced in Figure 25: in (a), the map obtained for {002} planes in pure-Al has the expected distribution of neighbour atoms along the plane, but a profile through the map along the dashed orange line and plotted in (b) shows that if some atoms are where they are expected in these peaks, a majority of the atoms are not and contribute to a high level of background. This means that most of the neighbourhood relationships are lost due to the offset induced by trajectory aberrations.

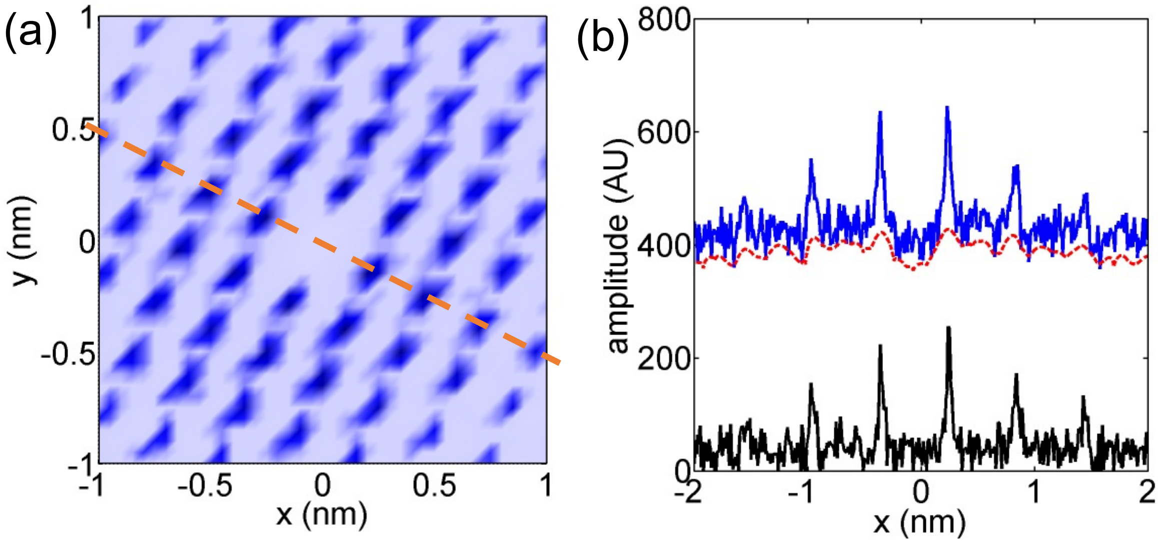

Figure 25: (a) 2D spatial distribution map for {002} planes in pure Al; and (b) amplitude of the distribution calculated along the dashed orange line in (a). The dashed red line in (b) gives an estimate of the background and in black is the background-reduced distribution (modified from [243]).

Recent work attempted to quantify the offset in the case of compositionally-complex alloys containing 5 elements in an equimolar mixture using finite-element simulations [284]. This analysis considered as input data pairs of neighbour atoms sitting on the same horizontal plane versus how far they are from each other in the reconstructed data within a horizontal plane and in depth, as plotted in Figure 26. Three ranges of evaporation field across the five species were considered: ±5 %, ±10 %, and ± 20 % variation around an average in (a), (b), and (c), respectively. This analysis shows that as the spread in evaporation field increases, the likelihood that atoms remain first neighbours drops substantially, with the offset in the z-direction being smaller by an order of magnitude on average. The relative robustness of the z-resolution has been used to study site occupation relationships in intermetallics [241,380,381] and recently also to investigate possible short-range ordering reactions [382].

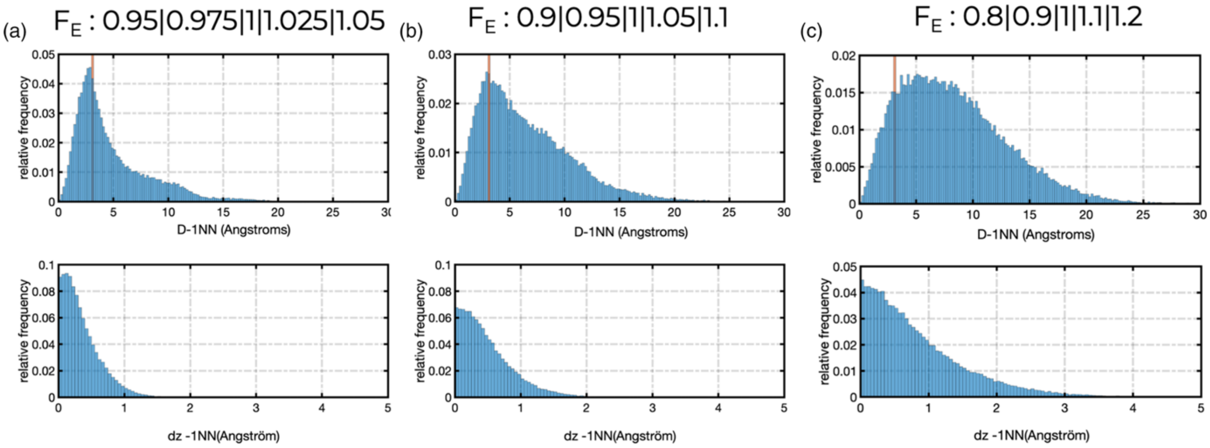

Figure 26: Results from finite-element simulations of the field evaporation of 5-element equimolar materials, considering atoms initially nearest neighbours and located at the same depth in the input data, the distributions of the distance to the 1st nearest neighbour within the same plane (D-1NN) and in the depth (dz-1NN) after field evaporation simulation and data

reconstruction are plotted for three ranges of evaporation fields F_E (a) ± 5 %, (b) ±10 %, and (c) ± 20 % around an average field (from [325]).

For single phase materials, there are reports in the literature of possible surface migration prior to the departure of the atoms from the specimen's surface [329,330]. These are assumed to be due to the retention of atoms of species requiring a very high field to trigger their evaporation on the surface, for instance C in Fe. During the time they are on the exposed surface, they can hop from one site to another driven by local field gradients [330]. This leads to their field evaporation from where the last atomic planes collapse, i.e. at the centre of poles and on zone lines where the build-up of the field can be very high. There have also been reports of apparent increase in composition of certain species along crystallographic poles. These are most likely related to "chromatic aberrations", i.e. whereby the evaporation field of atoms of a certain species at the pole makes them more susceptible to trajectory aberrations than others [364]. This is often visible in Al-alloys but also in numerous alloys (FeCr, compositionally-complex alloys etc.) and should not be mistaken for the signature of a different microstructural feature [325,383].

6.4.2 For materials with multiple phases

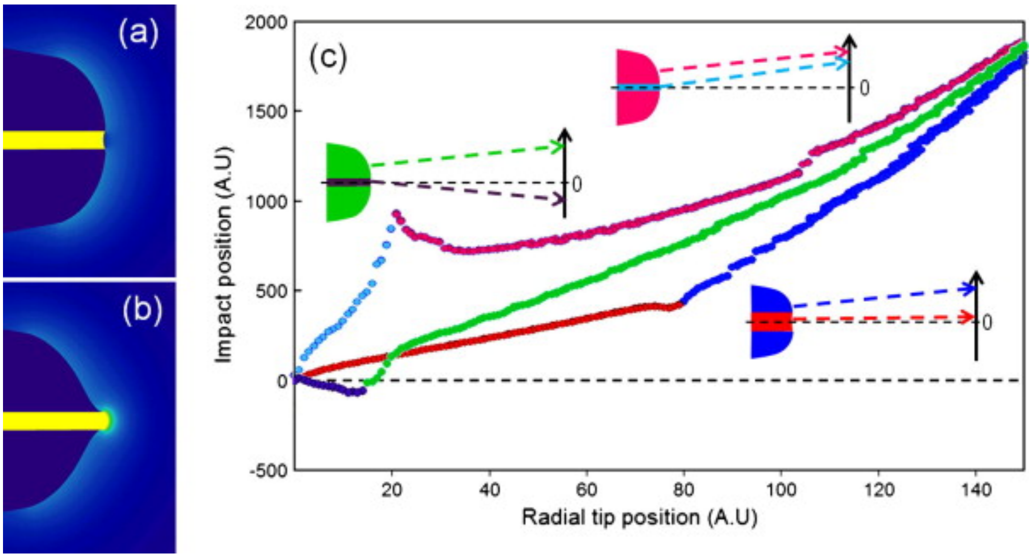

Figure 27: Distribution of the electrostatic field around a simulated shape for ε = 0.5. For clarity, a schematic view of the cylindrical precipitate in the core of the specimen has been superimposed (yellow). (b) Similar distribution for ε = 2.0. For clarity, a schematic view of the cylindrical precipitate in the core of the specimen has been superimposed (yellow). (c) Impact position on the detector as a function of the radial position at the specimen surface for cylindrical precipitate with $r_p \sim 3$ nm and ε = 2.0 (cyan and pink $r_p \sim 16$ nm and ε = 0.55 (red and blue) and $r_p \sim 3$ nm and ε = 0.55 (purple and green). Schematic views shown in the insets (from [384]) .

Additional issues arise when the curvature of the specimen's surface has heterogeneities, i.e. a locally higher or lower curvature, as this causes local changes in magnification [317] that lead to additional trajectory aberrations [304]. In Figure 27 are results from 2D simulations for two configurations of a cylinder in the core of a specimen forming a trough in (a) or a protrusion in (b) [384], and the result of projection of ions placed at different locations on the specimen surface on a virtual detector in (c). The interest here is to visualise that in all cases, some positions on the detector have ions originating from two different points on the emitting surface. There can be a "negative magnification" whereby ions originating from one side of the specimen land on the other side of the detector (green & purple). These curvature heterogeneities can arise from local changes in composition, i.e. secondary phases or precipitates [236], or crystalline defects [385]. The effect of these trajectory aberrations can be traced within the reconstructed data as variations in the point density [236], which can in turn be used to correct the reported composition of particles [386–388].

A recent article by De Geuser et al. reviewed the literature reporting particle size measured by APT and small-angle X-ray or neutron scattering (SAXS/SANS) for precipitate-strengthened alloys[12]. A cut-off was revealed for particles below approximately 1 nm as measured by APT. Once again, this only means that their size and composition measurement will be inaccurate, not that they are not imaged. This does not remove the fact that APT is uniquely positioned to provide extremely valuable insights, simply that care should be taken when reporting and interpreting the results.

6.5 Hydrogen

Spatially resolved characterization of hydrogen has been a long-standing frontier in microscopy and microanalysis and is an area where atom probe can provide unique insights. Hydrogen is known to embrittle and cause catastrophic failure for many materials [389,390]. However, its 3D spatial distribution within material structures at the atomic scale is difficult to determine using spectroscopic techniques and it is impossible to image directly. Hydrogen is readily detected in APT, but it is challenging to establish whether it originates from the specimen itself or from residual hydrogen from within the vacuum chamber. Isotopic labelling has been proposed as an approach to circumvent this issue [78,391,392]. Samples are charged with deuterium, which can serve as a marker for hydrogen from within the sample itself. This has been shown to successfully allow for the detection of hydrogen trapping [392,393], although quantification is not straightforward [394] and will depend on the analysis conditions [263,395]. In order to minimise diffusion of hydrogen out of the specimen, it is also necessary to keep the sample cold between charging and analysis. The study of hydrogen by APT has hence been facilitated in the past few years by developments in specimen transfer under cryogenic conditions. It has been shown that hydrogen can be trapped at grain boundaries, phase boundaries, and dislocations [155,396–398], and there have been several studies reporting the analysis of hydrides and their growth mechanisms[399,400]. A

7 Outlook

APT has remained a niche technique for several decades, but the past 20 years have seen both novel developments and ventures into new fields that make the outlook for the technique rather bright. There are efforts in multiple directions, some of which we will discuss below:

(1) Through direct integration of an atom probe into a TEM, there are opportunities to potentially achieve true “atomic-scale tomography” [71], which has been a longstanding goal for the community. The TOMO instrument at Forschung Zentrum Jülich is to be delivered before the end of 2024 and should start operation relatively soon after [74]. What may seem like the ultimate atomic-scale analytical instrument will not lead to miracles and will require dedicated and targeted developments in terms of specimen preparation, data acquisition, reconstruction, and processing in order to deliver its full potential. Amongst key limitations will be the limited efficiency of the single particle detectors – i.e. even if we could image that an atom has departed the surface of the specimen by electron microscopy, it may still go undetected. This may be overcome by advances in detector technology, as proposed by Kelly and Hunt [401]. If the design is similar to other delay-line detectors [402], the physical principle

is different and allows for avoiding the use of microchannel plates with their limited opened area leading to ion losses. There is also need to better understand the probabilistic nature of trajectory aberrations, revealed in more details by recent work using density-functional theory [357,403], and to combine these with modelling efforts [275,307] to better define the initial atom’s position.

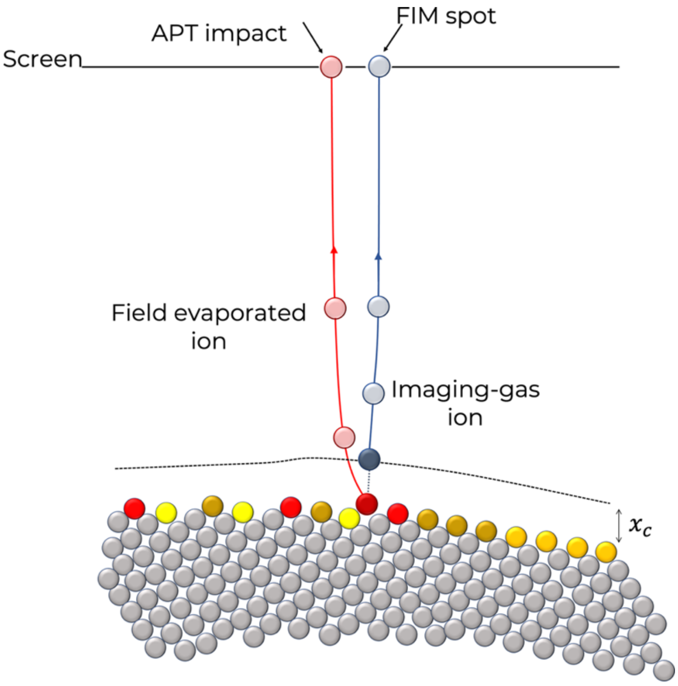

Figure 28: Diagram of the difference between the trajectories of a population of imaging gas ions, in blue, leading to the formation of an individual spot on a field-ion micrograph, and, in red, for an individual field evaporated ion leading to a single detector impact in atom probe tomography. From [325]

(2) Along similar lines, there have been efforts at combining atom probe and field-ion microscopy [33,34]. In these experiments APT is performed with a higher pressure of an imaging gas that allows for forming a field-ion image at the DC voltage in between pulses, while atoms from the specimen itself are field evaporated by the pulses. The issue of the high level of background from the time-independent field ionisation can be overcome through data mining and filtering. FIM allows for imaging the precise, actual atomic positions before the atom has been field evaporated, so in principle has full atomic resolution – at least on some of the imaged atomic planes. In combination with the analytical capabilities of APT and contrast interpretation by density-functional theory, this has enabled precise imaging of interaction between structural defects and specific solutes in simple alloys [31,33,404]. Energy-sensitive detectors, such as those recently proposed by Bacchi et al. [405] could further help with data filtering. These could be combined with novel instrumentation developments for FIM [406], along with new method developments [407–409] to push the boundaries of analytical field-ion microscopy.

(3) In terms of developments on the instrument side, the use of increasing photon energy in pulsed-laser atom probe may lead to potentially exciting new physics [39,67]. These novel, complex instruments may also offer additional mechanisms to better control

the field evaporation from materials that have not so far been amenable to APT analysis – including organics and soft matter.

(4) With respects to efforts in this latter space, soft matter, there have been several articles pointing to a possible role of APT in addressing fundamental questions in biology[410]. Until now most applications have been on biominerals [411–414] and not on soft tissues or even simple biomacromolecules such as proteins. These molecules are most often made of combinations of C, H, O, N and sometimes other elements in small quantity. This raises questions as to the potential role of APT as a compositional mapping tool, in particular because of the complex field evaporation behaviour of organic materials [57,415–420]. Before data could even be acquired, there was a need to develop paths for preparing samples from soft, often wet material systems. As discussed above, the availability of integrated suite of instruments for cryogenic handling, preparation, and transfer [41,47,75,159] is already making it easier to prepare specimens from frozen solutions or wet systems [167,168] as well as from environmentally-sensitive samples. This includes most materials for application in batteries, or catalysts. Recently developed approaches for capping APT specimens [181] (see Section 3.5) directly inside the FIB with no exposure to ambient atmosphere may also be generalised and help protect the reactive surface and increase yield. They may also maybe prevent unwanted effects of the field on the migration of e.g. Li [187] or maybe H.

(5) Early results reported for wet and soft materials have highlighted new levels of complexity in the way the data needs to be acquired and processed [157,165,166,421]. These frontier applications point to limits in the understanding of the physics of the field evaporation process in general, and more particularly for non-metallic or molecular materials. Ab initio calculations and atomistic simulations have been used for simulating the field evaporation process in the past [312,351,422,423], including for molecular materials [416]. These approaches are being revisited for metals [357,403] and to support contrast interpretation in field-ion microscopy [33,424], but also to rationalise the field evaporation of water [159] and the mechanisms of fragmentation of molecular ions [166,264–266]. There is still a strong need to push the development of these methods and advance the understanding of the details of the processes at play during an APT experiment to better interpret the data and avoid pitfalls and artefacts.

(6) The complexity of modern APT data arising from the analyses of an increasingly large array of materials, along with the ever-larger size of the datasets mean that extracting information reliably, reproducibly, and routinely requires the development of dedicated data processing techniques. The field has a long history of "data mining" [425], and there is a recent surge of interest in deploying machine-learning techniques to push these aspects even further. These include unsupervised and supervised learning approaches for cluster identification [230,426,427], but also data segmentation [428–430] and peak identification or quantification in the mass spectrum [205,260,431]. There will be a need in the future to make the APT data processing workflow more transparent, better documented, and compliant with FAIR principles[432] that are quickly moving toward becoming international standards. Research into how machine-learning can help with other areas is needed, including data reconstruction. This should involve advanced simulations to better account for

local magnification [236] and methods should be derived that go beyond the hypotheses that underpin current state-of-the-art algorithms [384].

This list is not exhaustive but gives a flavour for aspects that deserve new developments and that are being or will soon be subject of studies across the community.

9 Acknowledgements

The article was a collaborative effort and, even though we tried to be inclusive of all perspectives on various aspects of APT research, it reflects our experiences, and some articles likely escaped our attention. Apologies to those forgotten – it was not intentional.

BG is grateful to all members of his group at MPIE, and for financial support from the ERC (ERC-CoG-SHINE-771602), the Max-Planck Society, the BMBF, the DFG incl. for the Leibniz Prize, the Volkswagen Stiftung, the Alexander von Humboldt Stiftung and the EPSRC.

10 References

[1] E.W. Muller, Oberflachenwanderung von Wolfram auf dem eigenen Kristallgitter, Zeitschrift Fur Physik 126 (1949) 642–665. https://doi.org/10.1007/bf01328783.

[2] E.W. Müller, K. Bahadur, Field Ionization Of Gases At A Metal Surface And The Resolution Of The Field Ion Microscope, Physical Review 102 (1956) 624–631.

[3] E.W. Müller, Atoms Visualized, Scientific American 196 (1957) 113–122.

[4] E.W. Müller, J.A. Panitz, S.B. McLane, E.W. Müller, Atom-Probe Field Ion Microscope, Review of Scientific Instruments 39 (1968) 83–86. https://doi.org/10.1063/1.1683116.

[5] E.W. Müller, Atom-Probe Field Ion Microscope, Naturwissenschaften 57 (1970) 222–230.

[6] A. Cerezo, T.J. Godfrey, G.D.W. Smith, Application of a position-sensitive detector to atom probe microanalysis, Review of Scientific Instruments 59 (1988) 862. https://doi.org/10.1063/1.1139794.

[7] D. Blavette, A. Bostel, J.M. Sarrau, B. Deconihout, A. Menand, An atom probe for three-dimensional tomography, Nature 363 (1993) 432–435.

[8] J.A. Panitz, The 10 cm atom probe, Review of Scientific Instruments 44 (1973) 1034.

[9] A.R. Waugh, E.D. Boyes, M.J. Southon, Field-desorption microscopy and the atom probe, Nature 253 (1975) 342–343.

[10] T.F. Kelly, M.K. Miller, Invited review article: Atom probe tomography., The Review of Scientific Instruments 78 (2007) 31101. https://doi.org/10.1063/1.2709758.

[11] M.K. Miller, The Development of Atom Probe Field-Ion Microscopy, Materials Characterization 44 (2000) 11–27. https://doi.org/10.1016/S1044-5803(99)00053-4.

[12] F. De Geuser, B. Gault, Metrology of small particles and solute clusters by atom probe tomography, Acta Materialia 188 (2020) 406–415. https://doi.org/10.1016/j.actamat.2020.02.023.

[13] T.F. Kelly, T.T. Gribb, J.D. Olson, R.L. Martens, J.D. Shepard, S.A. Wiener, T.C. Kunicki, R.M. Ulfig, D.R. Lenz, E.M. Strennen, E. Oltman, J.H. Bunton, D.R. Strait, First data from a commercial local electrode atom probe (LEAP)., Microscopy and Microanalysis : The Official Journal of Microscopy Society of America, Microbeam Analysis Society, Microscopical Society of Canada 10 (2004) 373–383. https://doi.org/10.1017/S1431927604040565.

[14] B. Gault, F. Vurpillot, A. Vella, M. Gilbert, A. Menand, D. Blavette, B. Deconihout, Design of a femtosecond laser assisted tomographic atom probe, Review of Scientific Instruments 77 (2006) 43705. https://doi.org/10.1063/1.2194089.

[15] B. Deconihout, F. Vurpillot, B. Gault, G. Da Costa, M. Bouet, A. Bostel, D. Blavette, A. Hideur, G. Martel, M. Brunel, Toward a laser assisted wide-angle tomographic atom-probe, Surface and Interface Analysis 39 (2007) 278–282. https://doi.org/10.1002/sia.2491.

[16] L. Renaud, G. Da Costa, M. Bouet, B. Deconihout, Design of a fast multi-hit sensitive detector based on a CCD camera, Nucl. Instr. Meth. Phys. Res. Sect. A 477 (2002) 150–154.

[17] G.D. Costa, H. Wang, S. Duguay, A. Bostel, D. Blavette, B. Deconihout, G. Da Costa, H. Wang, S. Duguay, A. Bostel, D. Blavette, B. Deconihout, Advance in multi-hit detection and quantization in atom probe tomography, Review of Scientific Instruments 83 (2012) 123709.

[18] J.H. Bunton, J.D. Olson, D.R. Lenz, T.F. Kelly, Advances in pulsed-laser atom probe: instrument and specimen design for optimum performance., Microscopy and Microanalysis : The Official Journal of Microscopy Society of America, Microbeam Analysis Society, Microscopical Society of Canada 13 (2007) 418–427. https://doi.org/10.1017/S1431927607070869.

[19] K. Hono, T. Ohkubo, Y.M. Chen, M. Kodzuka, K. Oh-ishi, H. Sepehri-Amin, F. Li, T. Kinno, S. Tomiya, Y. Kanitani, Broadening the applications of the atom probe technique by ultraviolet femtosecond laser, Ultramicroscopy 111 (2011) 576–583.

[20] S.P. Ringer, M.H. Apperley, Networking strategies of the microscopy community for improved utilisation of advanced instruments: (1) The Australian Microscopy and Microanalysis Research Facility (AMMRF), Comptes Rendus Physique 15 (2014) 269–275. https://doi.org/10.1016/j.crhy.2014.01.003.

[21] D.G. Brandon, On Field Evaporation, Philosophical Magazine 14 (1966) 803–820.

[22] R.G. Forbes, Charge hopping and charge draining - 2 mechanisms of field desorption, Surface Science 102 (1981) 255–263.

[23] R.G. Forbes, Field evaporation theory: a review of basic ideas, Applied Surface Science 87–88 (1995) 1–11. https://doi.org/10.1016/0169-4332(94)00526-5.

[24] T.T. Tsong, Atom-Probe Field Ion Microscopy, Cambridge University Press, Cambridge, 1990. https://doi.org/10.1017/CBO9780511599842.

[25] M.K. Miller, A. Cerezo, M.G. Hetherington, G.D.W. Smith, Atom Probe Field Ion Microscopy, Oxford Science Publications - Clarendon Press, Oxford, UK, 1996.

[26] Williams. Lefebvre-Ulrikson, François. Vurpillot, Xavier. Sauvage, Atom probe tomography : put theory into practice, Academic Press, 2016.

[27] M.K. Miller, R.G. Forbes, Atom-Probe Tomography, Springer US, Boston, MA, 2014. https://doi.org/10.1007/978-1-4899-7430-3.

[28] D. Blavette, B. Deconihout, A. Bostel, J.M. Sarrau, M. Bouet, A. Menand, The tomographic atom-probe - a quantitative 3-dimensional nanoanalytical instrument on an atomic-scale, Review of Scientific Instruments 64 (1993) 2911–2919.

[29] E.W. Müller, Das Feldionenmikroskop, Zeitschrift Fur Physik 131 (1951) 136–142.

[30] J.A. Panitz, Field-Ion Microscopy - A Review Of Basic Principles And Selected Applications, Journal of Physics E-Scientific Instruments 15 (1982) 1281–1294. https://doi.org/10.1088/0022-3735/15/12/004.

[31] B. Klaes, J. Renaux, R. Lardé, F. Delaroche, F.F. Morgado, L.T. Stephenson, B. Gault, F. Vurpillot, Analytical Three-Dimensional Field Ion Microscopy of an Amorphous Glass

FeBSi, Microscopy and Microanalysis 28 (2022) 1280–1288. https://doi.org/10.1017/S1431927621012629.

[32] J.M.J.M.M. Cairney, B. Gault, D.J.D.J.J. Larson, Recognizing 60 years of achievements in field emission and atomic scale microscopy: Reflections on the International Field Emission Society, Materials Today 19 (2016) 182–183. https://doi.org/10.1016/j.mattod.2016.01.019.

[33] S.S. Katnagallu, L.T. Stephenson, I. Mouton, C. Freysoldt, A.P.A. Subramanyam, J. Jenke, A.N.C. Ladines, S. Neumeier, T. Hammerschmidt, R. Drautz, J. Neugebauer, F. Vurpillot, D. Raabe, B. Gault, Imaging individual solute atoms at crystalline imperfections in metals, New Journal of Physics 21 (2019) 123020. https://doi.org/10.1088/1367-2630/ab5cc4.

[34] S. Katnagallu, F.F.F. Morgado, I. Mouton, B. Gault, L.T. Stephenson, Three-dimensional atomically-resolved analytical imaging with a field ion microscope, Microscopy and Microanalysis 28 (2022) 1264–1279. https://doi.org/10.1017/S1431927621012381.

[35] A. Cerezo, T.J. Godfrey, S.J. Sijbrandij, G.D.W. Smith, P.J. Warren, Performance of an energy-compensated three-dimensional atom probe, Review of Scientific Instruments 69 (1998) 49.

[36] A. Bostel, M. Yavor, (12) Patent Application Publication (10) Pub. No.: US 2010/0223698 A1, 1 (2010).

[37] P.H. Clifton, T.T. Gribb, S.S.A. Gerstl, R.M.M. Ulfig, D.J.J. Larson, Performances Advantages of a Modern, Ultra-High Mass Resolution Atom Probe, Microscopy and Microanalysis 14 (Suppl. (2008) 454–455. https://doi.org/10.1017/S1431927608087217.

[38] A. Cerezo, M.K. Miller, Einzel lenses in atom probe designs, Surface Science 246 (1991) 450–456.

[39] A.N. Chiaramonti, L. Miaja-Avila, B.W. Caplins, P.T. Blanchard, D.R. DIercks, B.P. Gorman, N.A. Sanford, Field Ion Emission in an Atom Probe Microscope Triggered by Femtosecond-Pulsed Coherent Extreme Ultraviolet Light, Microscopy and Microanalysis 26 (2020) 258–266. https://doi.org/10.1017/S1431927620000203.

[40] P.A.J.J. Bagot, T. Visart de Bocarmé, A. Cerezo, G.D.W.W. Smith, 3D atom probe study of gas adsorption and reaction on alloy catalyst surfaces I: Instrumentation, Surface Science 600 (2006) 3028–3035. https://doi.org/10.1016/j.susc.2006.05.026.

[41] D.E. Perea, S.S.A. Gerstl, J. Chin, B. Hirschi, J.E. Evans, An environmental transfer hub for multimodal atom probe tomography., Advanced Structural and Chemical Imaging 3 (2017) 12. https://doi.org/10.1186/s40679-017-0045-2.

[42] I.E. McCarroll, P.A.J. Bagot, A. Devaraj, D.E. Perea, J.M. Cairney, New frontiers in atom probe tomography: a review of research enabled by cryo and/or vacuum transfer systems, Materials Today Advances 7 (2020) 100090. https://doi.org/10.1016/j.mtadv.2020.100090.

[43] S. Dumpala, S.R. Broderick, P.A.J. Bagot, K. Rajan, An integrated high temperature environmental cell for atom probe tomography studies of gas-surface reactions:

instrumentation and results., Ultramicroscopy 141 (2014) 16–21. https://doi.org/10.1016/j.ultramic.2014.03.002.

[44] D. Haley, I. McCarroll, P.A.J. Bagot, J.M. Cairney, M.P. Moody, A Gas-Phase Reaction Cell for Modern Atom Probe Systems, Microscopy and Microanalysis 25 (2019) 410–417. https://doi.org/10.1017/S1431927618016240.

[45] H. Khanchandani, A.A. El-Zoka, S.-H. Kim, U. Tezins, D. Vogel, A. Sturm, D. Raabe, B. Gault, L.T. Stephenson, Laser-equipped gas reaction chamber for probing environmentally sensitive materials at near atomic scale, PLOS ONE 17 (2022) e0262543. https://doi.org/10.1371/journal.pone.0262543.

[46] S.S.A. Gerstl, R. Wepf, Methods in Creating, Transferring, & Measuring Cryogenic Samples for APT, Microscopy and Microanalysis 21 (2015) 517–518. https://doi.org/10.1017/S1431927615003384.

[47] L.T. Stephenson, A. Szczepaniak, I. Mouton, K.A.K. Rusitzka, A.J. Breen, U. Tezins, A. Sturm, D. Vogel, Y. Chang, P. Kontis, A. Rosenthal, J.D. Shepard, U. Maier, T.F. Kelly, D. Raabe, B. Gault, The Laplace project: an integrated suite for correlative atom probe tomography and electron microscopy under cryogenic and UHV conditions, PLOS One 13 (2018) e0209211. https://doi.org/10.1371/journal.pone.0209211.

[48] P.J. Felfer, A Toolchain for the Analysis of Hydrogen in Materials at the Atomic Scale, Microscopy and Microanalysis 25 (2019) 278–279. https://doi.org/10.1017/S1431927619002125.

[49] G. Da Costa, F. Vurpillot, A. Bostel, M. Bouet, B. Deconihout, Design of a delay-line position-sensitive detector with improved performance, Review of Scientific Instruments 76 (2005) 13304. https://doi.org/013304 10.1063/1.1829975.

[50] O. Jagutzki, A. Cerezo, A. Czasch, R. Dorner, M. Hattass, M. Huang, V. Mergel, U. Spillmann, K. Ullmann-Pfleger, T. Weber, H. Schmidt-Bocking, G.D.W. Smith, Multiple hit readout of a microchannel plate detector with a three-layer delay-line anode, IEEE Transactions on Nuclear Science 49 (2002) 2477–2483. https://doi.org/10.1109/tns.2002.803889.

[51] F. Meisenkothen, E.B. Steel, T.J. Prosa, K.T. Henry, R. Prakash Kolli, Effects of detector dead-time on quantitative analyses involving boron and multi-hit detection events in atom probe tomography., Ultramicroscopy 159 Pt 1 (2015) 101–111. https://doi.org/10.1016/j.ultramic.2015.07.009.

[52] Z. Peng, F. Vurpillot, P.-P. Choi, Y. Li, D. Raabe, B. Gault, On the detection of multiple events in atom probe tomography, Ultramicroscopy 189 (2018) 54–60. https://doi.org/10.1016/j.ultramic.2018.03.018.

[53] M.K. Miller, Thomas.F. Kelly, K. Rajan, S.P. Ringer, The future of atom probe tomography, Materials Today 15 (2012) 158–165. https://doi.org/10.1016/S1369-7021(12)70069-X.

[54] T.F. Kelly, Kinetic energy discrimination for atom probe tomography, Microscopy and Microanalysis 17 (2011) 1–14.

[55] J. Suttle author, A superconducting ion detector, 2018., 2018. https://search.library.wisc.edu/catalog/9912648659402121 (accessed February 6, 2025).

[56] C. Bacchi, G. Da Costa, F. Vurpillot, Development of an energy-sensitive detector for the Atom Probe Tomography, Microscopy and Microanalysis First View (2022) 1076–1091. https://doi.org/doi.org/10.1017/S1431927621012708.

[57] O. Nishikawa, Y. Ohtani, K. Maeda, M. Watanabe, K. Tanaka, Development of the Scanning Atom Probe and Atomic Level Analysis, Materials Characterization 44 (2000) 29–57. https://doi.org/10.1016/S1044-5803(99)00046-7.

[58] A. Cerezo, T.J. Godfrey, M. Huang, G.D.W. Smith, Design of a scanning atom probe with improved mass resolution, Review of Scientific Instruments 71 (2000) 3016–3023.

[59] L. Rousseau, A. Normand, F.F. Morgado, L. Stephenson, B. Gault, K. Tehrani, F. Vurpillot, Dynamic Effects in Voltage Pulsed Atom Probe, Microscopy and Microanalysis 26 (2020) 1133–1146. https://doi.org/10.1017/S1431927620024587.

[60] D.J. Larson, T.J. Prosa, R.M. Ulfig, B.P. Geiser, T.F. Kelly, Local electrode atom probe tomography, New York, US: Springer Science (2013) 318.

[61] T.T. Tsong, J.H. Block, M. Nagasaka, B. Viswanatha, Photon stimulated field ionization, Journal of Chemical Physics 65 (1976) 2469.

[62] G.L. Kellogg, T.T. Tsong, Pulsed-laser atom-probe field-ion microscopy, Journal of Applied Physics 51 (1980) 1184. https://doi.org/10.1063/1.327686.

[63] A. Cerezo, G.D.W. Smith, EFFECT OF LASER PULSE SHAPE ON MASS RESOLUTION IN THE PULSED-LASER ATOM PROBE., Journal of Physics E: Scientific Instruments 20 (1987) 1392–1394.

[64] F. Vurpillot, M. Gilbert, B. Deconihout, Towards the three-dimensional field ion microscope, Surface and Interface Analysis 39 (2007) 273–277. https://doi.org/10.1002/sia.2490.

[65] A. Cerezo, G.D.W. Smith, P.H. Clifton, Measurement of temperature rises in the femtosecond laser pulsed three-dimensional atom probe, Applied Physics Letters 88 (2006) 154103. https://doi.org/10.1063/1.2191412.

[66] T. Prosa, D. Lenz, I. Martin, D. Reinhard, D. Larson, J. Bunton, Evaporation-Field Differences with Deep-UV Atom Probe Tomography, Microscopy and Microanalysis 27 (2021) 1262–1264. https://doi.org/10.1017/S1431927621004736.

[67] A.N. Chiaramonti, L. Miaja-Avila, P.T. Blanchard, D.R. Diercks, B.P. Gorman, N.A. Sanford, A Three-Dimensional Atom Probe Microscope Incorporating a Wavelength-Tuneable Femtosecond-Pulsed Coherent Extreme Ultraviolet Light Source, MRS Advances (2019) 1–9. https://doi.org/10.1557/adv.2019.296.

[68] B.W. Caplins, A.N. Chiaramonti, J.M. Garcia, N.A. Sanford, L. Miaja-Avila, Atom probe tomography using an extreme ultraviolet trigger pulse, Review of Scientific Instruments 94 (2023) 093704. https://doi.org/10.1063/5.0160797.

[69] A. Rundquist, C.G. Durfee, Z. Chang, C. Herne, S. Backus, M.M. Murnane, H.C. Kapteyn, Phase-Matched Generation of Coherent Soft X-rays, Science 280 (1998) 1412–1415. https://doi.org/10.1126/science.280.5368.1412.

[70] A. Vella, J. Houard, L. Arnoldi, M. Tang, M. Boudant, A. Ayoub, A. Normand, G. Da Costa, A. Hideur, High-resolution terahertz-driven atom probe tomography, Science Advances 7 (2021) eabd7259. https://doi.org/10.1126/sciadv.abd7259.

[71] T.F. Kelly, M.K. Miller, K. Rajan, S.P. Ringer, Atomic-scale tomography: a 2020 vision., Microscopy and Microanalysis : The Official Journal of Microscopy Society of America, Microbeam Analysis Society, Microscopical Society of Canada 19 (2013) 652–664. https://doi.org/10.1017/S1431927613000494.

[72] B.P. Gorman, S.P. Ringer, T.F. Kelly, eds., Atomic-Scale Analytical Tomography, in: Atomic-Scale Analytical Tomography: Concepts and Implications, Cambridge University Press, Cambridge, 2022: pp. i–i. https://www.cambridge.org/core/books/atomicscale-analytical-tomography/atomicscale-analytical-tomography/8AF4C6BEEEA9A14E231152448904CF65 (accessed August 29, 2023).

[73] T. Kelly, R. Dunin-Borkowski, J. Meyer, Project Tomo: Toward Atomic-scale Analytical Tomography, Microscopy and Microanalysis 26 (2020) 2618–2621. https://doi.org/10.1017/s1431927620022205.

[74] J. Mayer, J. Barthel, A. Vayyala, R. Dunin-Borkowski, M. Bischoff, H. van Leeuwen, S. Kujawa, J. Bunton, D. Lenz, T.F. Kelly, The TOMO Project – Integrating a Fully Functional Atom Probe in an Aberration-Corrected TEM, Microscopy and Microanalysis 29 (2023) 593–594. https://doi.org/10.1093/micmic/ozad067.286.

[75] P. Stender, H. Solodenko, A. Weigel, I. Balla, T.M. Schwarz, J. Ott, M. Roussell, Y. Joshi, R. Duran, M. Al-Shakran, T. Jacob, G. Schmitz, A Modular Atom Probe Concept: Design, Operational Aspects, and Performance of an Integrated APT-FIB/SEM Solution, Microscopy and Microanalysis 28 (2022) 1168–1180. https://doi.org/10.1017/S1431927621013982.

[76] J. Houard, A. Normand, E. Di Russo, C. Bacchi, P. Dalapati, G. Beainy, S. Moldovan, G. Da Costa, F. Delaroche, C. Vaudolon, J.M. Chauveau, M. Hugues, D. Blavette, B. Deconihout, A. Vella, F. Vurpillot, L. Rigutti, A photonic atom probe coupling 3D atomic scale analysis with in situ photoluminescence spectroscopy, Review of Scientific Instruments 91 (2020) 083704. https://doi.org/10.1063/5.0012359.

[77] P. Felfer, B. Ott, M. Monajem, V. Dalbauer, M. Heller, J. Josten, C. Macaulay, An Atom Probe with Ultra-Low Hydrogen Background, Microscopy and Microanalysis 28 (2022) 1255–1263. https://doi.org/10.1017/S1431927621013702.

[78] R. Gemma, T. Al-Kassab, R. Kirchheim, A. Pundt, APT analyses of deuterium-loaded Fe/V multi-layered films, Ultramicroscopy 109 (2009) 631–636. https://doi.org/10.1016/j.ultramic.2008.11.005.

[79] R. Gemma, T. Al-Kassab, R. Kirchheim, A. Pundt, Visualization of deuterium dead layer by atom probe tomography, Scripta Materialia 67 (2012) 903–906. https://doi.org/10.1016/j.scriptamat.2012.08.025.

[80] D. Blavette, J.M. Sarrau, A. Bostel, J. Gallot, Direction and depth of atom probe analysis, Revue De Physique Appliquee 17 (1982) 435–440.

[81] P. Bas, A. Bostel, B. Deconihout, D. Blavette, A general protocol for the reconstruction of 3D atom probe data, Applied Surface Science 87–88 (1995) 298–304.

[82] M.K. Miller, G.D.W. Smith, Atom Probe Microanalysis: Principles and Applications to Materials Problems, Materials Research Society, Pittsburg, PA, 1989.

[83] A.J. Melmed, The art and science and other aspects of making sharp tips, Journal of Vacuum Science & Technology B 9 (1991) 601–608.

[84] J.M. Papazian, The preparation of field-ion-microscope specimens containing grain boundaries, Journal of Microscopy 94 (1971) 63–67. https://doi.org/10.1111/j.1365-2818.1971.tb02361.x.

[85] H. Nordén, K.M. Bowkett, Electron microscope holders for viewing thin wire specimens and field-ion microscope tips, Journal of Scientific Instruments 44 (1967) 238–240. https://doi.org/10.1088/0950-7671/44/3/423.

[86] A. Henjered, H. Norden, A controlled specimen preparation technique for interface studies with atom-probe field-ion microscopy, Journal of Physics E: Scientific Instruments 16 (1983) 617–619. https://doi.org/10.1088/0022-3735/16/7/014.

[87] R. Estivill, G. Audoit, J.-P. Barnes, A. Grenier, D. Blavette, Preparation and Analysis of Atom Probe Tips by Xenon Focused Ion Beam Milling., Microscopy and Microanalysis : The Official Journal of Microscopy Society of America, Microbeam Analysis Society, Microscopical Society of Canada 22 (2016) 576–582. https://doi.org/10.1017/S1431927616000581.

[88] B. Gault, A.J. Breen, Y. Chang, J. He, E.A. Jägle, P. Kontis, P. Kürnsteiner, A. Kwiatkowski Da Silva, S.K. Makineni, I. Mouton, H. Zhao, D. Raabe, Interfaces and defect composition at the near-atomic scale through atom probe tomography investigations, Journal of Materials Research 33 (2018) 4018–4030. https://doi.org/10.1557/jmr.2018.375.

[89] K. Eder, V. Bhatia, B. Van Leer, J.M. Cairney, Using a Plasma FIB Equipped with Xe, N 2 , O 2 and Ar for Atom Probe Sample Preparation – Ion Implantation and Success Rates, Microscopy and Microanalysis 25 (2019) 316–317. https://doi.org/10.1017/s1431927619002319.

[90] J.E. Halpin, R.W.H. Webster, H. Gardner, M.P. Moody, P.A.J. Bagot, D.A. MacLaren, An in-situ approach for preparing atom probe tomography specimens by xenon plasma-focussed ion beam, Ultramicroscopy 202 (2019) 121–127. https://doi.org/10.1016/j.ultramic.2019.04.005.

[91] S.K. Makineni, M. Lenz, P. Kontis, Z. Li, A. Kumar, P.J.J.J. Felfer, S. Neumeier, M. Herbig, E. Spiecker, D. Raabe, B. Gault, D. Raabe, B. Gault, Correlative Microscopy—Novel Methods and Their Applications to Explore 3D Chemistry and Structure of Nanoscale Lattice Defects: A Case Study in Superalloys, JOM 70 (2018) 1736–1743. https://doi.org/10.1007/s11837-018-2802-7.

[92] M.L. Taheri, J.T. Sebastian, B.W. Reed, D.N. Seidman, A.D. Rollett, Site-specific atomic scale analysis of solute segregation to a coincidence site lattice grain boundary, Ultramicroscopy 110 (2010) 278–284. https://doi.org/10.1016/j.ultramic.2009.11.006.

[93] M.I. Hartshorne, D. Isheim, D.N. Seidman, M.L. Taheri, Specimen preparation for correlating transmission electron microscopy and atom probe tomography of

mesoscale features., Ultramicroscopy 147 (2014) 25–32. https://doi.org/10.1016/j.ultramic.2014.05.005.

[94] D.J. Larson, D.T. Foord, A.K. Petford-Long, T.C. Anthony, I.M. Rozdilsky, A. Cerezo, G.W.D. Smith, Focused ion-beam milling for field-ion specimen preparation:, Ultramicroscopy 75 (1998) 147–159. https://doi.org/10.1016/S0304-3991(98)00058-8.

[95] D.J. Larson, D.T. Foord, A.K. Petford-Long, H. Liew, M.G. Blamire, A. Cerezo, G.D.W. Smith, Field-ion specimen preparation using focused ion-beam milling, Ultramicroscopy 79 (1999) 287–293. https://doi.org/10.1016/S0304-3991(99)00055-8.

[96] M.K.K. Miller, K.F.F. Russell, Atom probe specimen preparation with a dual beam SEM/FIB miller., in: Ultramicroscopy, IEEE, 2006: pp. 761–766. https://doi.org/10.1016/j.ultramic.2007.02.023.

[97] M.K. Miller, K.F. Russell, G.B. Thompson, Strategies for fabricating atom probe specimens with a dual beam FIB., Ultramicroscopy 102 (2005) 287–298. https://doi.org/10.1016/j.ultramic.2004.10.011.

[98] M.K. Miller, K.F. Russell, K. Thompson, R. Alvis, D.J. Larson, Review of atom probe FIB-based specimen preparation methods., Microscopy and Microanalysis : The Official Journal of Microscopy Society of America, Microbeam Analysis Society, Microscopical Society of Canada 13 (2007) 428–436. https://doi.org/10.1017/S1431927607070845.

[99] K. Thompson, D. Lawrence, D.J. Larson, J.D. Olson, T.F. Kelly, B. Gorman, In situ site-specific specimen preparation for atom probe tomography., Ultramicroscopy 107 (2007) 131–139. https://doi.org/10.1016/j.ultramic.2006.06.008.

[100] I. Utke, P. Hoffmann, J. Melngailis, Gas-assisted focused electron beam and ion beam processing and fabrication, Journal of Vacuum Science & Technology B: Microelectronics and Nanometer Structures Processing, Measurement, and Phenomena 26 (2008) 1197–1276. https://doi.org/10.1116/1.2955728.

[101] J.F. Ziegler, M.D. Ziegler, J.P. Biersack, SRIM – The stopping and range of ions in matter (2010), Nuclear Instruments and Methods in Physics Research Section B: Beam Interactions with Materials and Atoms 268 (2010) 1818–1823. https://doi.org/10.1016/J.NIMB.2010.02.091.

[102] K.A. UNOCIC, M.J. MILLS, G.S. DAEHN, Effect of gallium focused ion beam milling on preparation of aluminium thin foils, Journal of Microscopy 240 (2010) 227–238. https://doi.org/10.1111/j.1365-2818.2010.03401.x.

[103] B. Gault, A.J. Breen, Y. Chang, J. He, E.A. Jägle, P. Kontis, P. Kürnsteiner, A. Kwiatkowski Da Silva, S.K. Makineni, I. Mouton, Z. Peng, D. Ponge, T. Schwarz, L.T. Stephenson, A. Szczepaniak, H. Zhao, D. Raabe, Interfaces and defect composition at the near-atomic scale through atom probe tomography investigations, Journal of Materials Research 33 (2018). https://doi.org/10.1557/jmr.2018.375.

[104] H. Zhao, F. De Geuser, A. Kwiatkowski da Silva, A. Szczepaniak, B. Gault, D. Ponge, D. Raabe, Segregation assisted grain boundary precipitation in a model Al-Zn-Mg-Cu alloy, Acta Materialia 156 (2018) 318–329. https://doi.org/10.1016/j.actamat.2018.07.003.

[105] K. Fisher, E. Marquis, Comparing Plasma-FIB and Ga-FIB Preparation of Atom Probe Tomography Samples, Microscopy and Microanalysis 22 (2016) 692–693. https://doi.org/10.1017/s1431927616004311.

[106] J.R. Famelton, G.M. Hughes, C.A. Williams, C. Barbatti, M.P. Moody, P.A.J. Bagot, Xenon plasma focussed ion beam preparation of an Al-6XXX alloy sample for atom probe tomography including analysis of an α-Al(Fe,Mn)Si dispersoid, Materials Characterization 178 (2021) 111194. https://doi.org/10.1016/J.MATCHAR.2021.111194.

[107] D.J. Larson, C.-M. Teng, P.P. Camus, T.F. Kelly, Fabrication of microtips on planar specimens, Applied Surface Science 87–88 (1995) 446–452. https://doi.org/10.1016/0169-4332(94)00504-4.

[108] P. Felfer, I. McCarroll, C. Macauley, J.M. Cairney, A simple approach to atom probe sample preparation by using shadow masks, Ultramicroscopy 160 (2016) 163–167. https://doi.org/10.1016/j.ultramic.2015.09.005.

[109] N. White, K. Eder, J. Byrnes, J.M. Cairney, I.E. McCarroll, Laser ablation sample preparation for atom probe tomography and transmission electron microscopy, Ultramicroscopy 220 (2021) 113161. https://doi.org/10.1016/j.ultramic.2020.113161.

[110] B. Tordoff, C. Hartfield, A.J. Holwell, S. Hiller, M. Kaestner, S. Kelly, J. Lee, S. Müller, F. Perez-Willard, T. Volkenandt, R. White, T. Rodgers, The LaserFIB: new application opportunities combining a high-performance FIB-SEM with femtosecond laser processing in an integrated second chamber, Applied Microscopy 50 (2020) 24. https://doi.org/10.1186/s42649-020-00044-5.

[111] S. Hestad, F. Pérez-Willard, C. Hartfield, K. Crosby, R. Ulfig, K. Rice, Laser Ablation: A New Approach to APT Specimen Preparation, Microscopy and Microanalysis 28 (2022) 50–51. https://doi.org/10.1017/S1431927622001118.

[112] M. Tkadletz, H. Waldl, M. Schiester, A. Lechner, G. Schusser, M. Krause, N. Schalk, Efficient preparation of microtip arrays for atom probe tomography using fs-laser processing, Ultramicroscopy 246 (2023) 113672. https://doi.org/10.1016/j.ultramic.2022.113672.

[113] A. Bachmaier, G.B. Rathmayr, P. Felfer, Mechanical Precision Preparation of Atom Probe Tips, Microscopy and Microanalysis 25 (2019) 320–321. https://doi.org/10.1017/S1431927619002332.

[114] C. Barroo, A.J. Akey, D.C. Bell, Atom Probe Tomography for Catalysis Applications: A Review, Applied Sciences 9 (2019) 2721. https://doi.org/10.3390/app9132721.

[115] P. Felfer, T. Li, K. Eder, H. Galinski, A.P. Magyar, D.C. Bell, G.D.W. Smith, N. Kruse, S.P. Ringer, J.M. Cairney, New approaches to nanoparticle sample fabrication for atom probe tomography, Ultramicroscopy 159 (2015) 413–419. https://doi.org/10.1016/j.ultramic.2015.04.014.

[116] T. Li, P.A.J. Bagot, E. Christian, B.R.C. Theobald, J.D.B. Sharman, D. Ozkaya, M.P. Moody, S.C.E. Tsang, G.D.W. Smith, Atomic Imaging of Carbon-Supported Pt, Pt/Co, and Ir@Pt Nanocatalysts by Atom-Probe Tomography, ACS Catalysis 4 (2014) 695–702. https://doi.org/10.1021/cs401117e.

[117] K. Tedsree, T. Li, S. Jones, C.W.A. Chan, K.M.K. Yu, P.A.J. Bagot, E.A. Marquis, G.D.W. Smith, S.C.E. Tsang, Hydrogen production from formic acid decomposition at room temperature using a Ag-Pd core-shell nanocatalyst, Nature Nanotechnology 6 (2011) 302–307. https://doi.org/10.1038/nnano.2011.42.

[118] A. Devaraj, M. Gu, R. Colby, P. Yan, C.M. Wang, J.M. Zheng, J. Xiao, A. Genc, J.G. Zhang, I. Belharouak, D. Wang, K. Amine, S. Thevuthasan, Visualizing nanoscale 3D compositional fluctuation of lithium in advanced lithium-ion battery cathodes, Nature Communications 6 (2015). https://doi.org/10.1038/ncomms9014.

[119] D. Diercks, B.P. Gorman, C.L. Cheung, G. Wang, Techniques for Consecutive TEM and Atom Probe Tomography Analysis of Nanowires, Microscopy and Microanalysis 15 (2009) 254–255. https://doi.org/doi:10.1017/S1431927609093398.

[120] Y. Xiang, V. Chitry, P. Liddicoat, P. Felfer, J. Cairney, S. Ringer, N. Kruse, Long-chain terminal alcohols through catalytic CO hydrogenation, Journal of the American Chemical Society 135 (2013) 7114–7117. https://doi.org/10.1021/ja402512r.

[121] C. Barroo, A.J. Akey, D.C. Bell, Aggregated nanoparticles: Sample preparation and analysis by atom probe tomography, Ultramicroscopy 218 (2020). https://doi.org/10.1016/j.ultramic.2020.113082.

[122] S.-H.H. Kim, P.W. Kang, O.O. Park, J.-B.B. Seol, J.-P.P. Ahn, J.Y. Lee, P.-P.P. Choi, A new method for mapping the three-dimensional atomic distribution within nanoparticles by atom probe tomography (APT), Ultramicroscopy 190 (2018) 30–38. https://doi.org/10.1016/J.ULTRAMIC.2018.04.005.

[123] K. Jang, S.-H. Kim, H. Jun, C. Jung, J. Yu, S. Lee, P.-P. Choi, Three-dimensional Atomic Mapping of Ligands on Nanoparticles, Nature Communications (2021).

[124] J. Lim, S.-H. Kim, R. Aymerich Armengol, O. Kasian, P.-P. Choi, L.T. Stephenson, B. Gault, C. Scheu, Atomic-Scale Mapping of Impurities in Partially Reduced Hollow TiO2 Nanowires, Angewandte Chemie - International Edition (2020). https://doi.org/10.1002/anie.201915709.

[125] S.-H.S.H. Kim, J. Lim, R. Sahu, O. Kasian, L.T.L.T. Stephenson, C. Scheu, B. Gault, Direct Imaging of Dopant and Impurity Distributions in 2D MoS2, Advanced Materials 32 (2020). https://doi.org/10.1002/adma.201907235.

[126] M. Krämer, B. Favelukis, A.A. El-Zoka, M. Sokol, B.A. Rosen, N. Eliaz, S.-H. Kim, B. Gault, Near-Atomic-Scale Perspective on the Oxidation of Ti3C2Tx MXenes: Insights from Atom Probe Tomography (Adv. Mater. 3/2024), Advanced Materials 36 (2024) 2470024. https://doi.org/10.1002/adma.202470024.

[127] S.-H. Kim, S.-H. Yoo, P. Chakraborty, J. Jeong, J. Lim, A.A. El-Zoka, L.T. Stephenson, T. Hickel, J. Neugebauer, C. Scheu, M. Todorova, B. Gault, Understanding Alkali Contamination in Colloidal Nanomaterials to Unlock Grain Boundary Impurity Engineering, Journal of the American Chemical Society 144 (2022) 987–994. https://doi.org/10.1021/jacs.1c11680.

[128] L.S. Aota, C. Jung, S. Zhang, S.-H. Kim, B. Gault, Revealing Compositional Evolution of PdAu Electrocatalyst by Atom Probe Tomography, ACS Energy Lett. 8 (2023) 2824–2830. https://doi.org/10.1021/acsenergylett.3c00911.

[129] W. Xiang, N. Yang, X. Li, J. Linnemann, U. Hagemann, O. Ruediger, M. Heidelmann, T. Falk, M. Aramini, S. DeBeer, M. Muhler, K. Tschulik, T. Li, 3D atomic-scale imaging of mixed Co-Fe spinel oxide nanoparticles during oxygen evolution reaction, Nat Commun 13 (2022) 179. https://doi.org/10.1038/s41467-021-27788-2.

[130] D.J. Larson, A.D. Giddings, Y. Wu, M.A. Verheijen, T.J. Prosa, F. Roozeboom, K.P. Rice, W.M.M. Kessels, B.P. Geiser, T.F. Kelly, Encapsulation method for atom probe tomography analysis of nanoparticles, Ultramicroscopy 159 (2015) 420–426. https://doi.org/10.1016/j.ultramic.2015.02.014.

[131] K. Thompson, D.J. Larson, R.M. Ulfig, Pre-sharpened and Flat-top Microtip Coupons: a Quantitative Comparison for Atom-Probe Analysis Studies, Microscopy and Microanalysis 11 (2005) 882–883. https://doi.org/doi:10.1017/S1431927605502629.

[132] P.J. Felfer, T. Alam, S.P. Ringer, J.M. Cairney, A reproducible method for damage-free site-specific preparation of atom probe tips from interfaces, Microscopy Research and Technique 75 (2012) 484–491. https://doi.org/10.1002/jemt.21081.

[133] M. Herbig, P. Choi, D. Raabe, Combining structural and chemical information at the nanometer scale by correlative transmission electron microscopy and atom probe tomography., Ultramicroscopy 153 (2015) 32–39. https://doi.org/10.1016/j.ultramic.2015.02.003.

[134] B. Loberg, H. Norden, Observations of the field-evaporation end form of tungsten, Arkiv For Fysik 39 (1968) 383–395.

[135] B. Gault, M.P. Moody, J.M. Cairney, S.P. Ringer, Atom probe crystallography, Materials Today 15 (2012) 378–386. https://doi.org/10.1016/S1369-7021(12)70164-5.

[136] F. Vurpillot, A. Bostel, E. Cadel, D. Blavette, The spatial resolution of 3D atom probe in the investigation of single-phase materials, Ultramicroscopy 84 (2000) 213–224. https://doi.org/10.1016/S0304-3991(00)00035-8.

[137] B. Gault, M.P. Moody, F. De Geuser, A. La Fontaine, L.T. Stephenson, D. Haley, S.P. Ringer, Spatial resolution in atom probe tomography., Microscopy and Microanalysis 16 (2010) 99–110. https://doi.org/10.1017/S1431927609991267.

[138] M. Herbig, Spatially correlated electron microscopy and atom probe tomography: Current possibilities and future perspectives, Scripta Materialia 148 (2018) 98–105. https://doi.org/10.1016/J.SCRIPTAMAT.2017.03.017.

[139] M. Herbig, D. Raabe, Y.J. Li, P. Choi, S. Zaefferer, S. Goto, Atomic-Scale Quantification of Grain Boundary Segregation in Nanocrystalline Material, Physical Review Letters 112 (2014) 126103. https://doi.org/10.1103/PhysRevLett.112.126103.

[140] S.K. Makineni, A. Kumar, M. Lenz, P. Kontis, T. Meiners, C. Zenk, S. Zaefferer, G. Eggeler, S. Neumeier, E. Spiecker, D. Raabe, B. Gault, On the diffusive phase transformation mechanism assisted by extended dislocations during creep of a single crystal CoNi-based superalloy, Acta Materialia 155 (2018) 362–371. https://doi.org/10.1016/J.ACTAMAT.2018.05.074.

[141] D. Palanisamy, D. Raabe, B. Gault, On the compositional partitioning during phase transformation in a binary ferromagnetic MnAl alloy, Acta Materialia 174 (2019) 227–236. https://doi.org/10.1016/j.actamat.2019.05.037.

[142] D. Palanisamy, D. Raabe, B. Gault, Elemental segregation to twin boundaries in a MnAl ferromagnetic Heusler alloy, Scripta Materialia 155 (2018) 144–148. https://doi.org/10.1016/j.scriptamat.2018.06.037.

[143] K. Inoue, K. Yoshida, Y. Nagai, K. Kishida, H. Inui, Correlative atom probe tomography and scanning transmission electron microscopy reveal growth sequence of LPSO phase in Mg alloy containing Al and Gd, Sci Rep 11 (2021) 3073. https://doi.org/10.1038/s41598-021-82705-3.

[144] C.H. Liebscher, A. Stoffers, M. Alam, L. Lymperakis, O. Cojocaru-Mirédin, B. Gault, J. Neugebauer, G. Dehm, C. Scheu, D. Raabe, Strain-Induced Asymmetric Line Segregation at Faceted Si Grain Boundaries, Physical Review Letters 121 (2018) 15702. https://doi.org/10.1103/PhysRevLett.121.015702.

[145] O. Cojocaru-Mirédin, Y. Fu, A. Kostka, R. Sáez-Araoz, A. Beyer, N. Knaub, K. Volz, C.-H. Fischer, D. Raabe, Interface engineering and characterization at the atomic-scale of pure and mixed ion layer gas reaction buffer layers in chalcopyrite thin-film solar cells, Progress in Photovoltaics: Research and Applications (2014) n/a--n/a. https://doi.org/10.1002/pip.2484.

[146] I. Povstugar, J. Weber, D. Naumenko, T. Huang, M. Klinkenberg, W.J. Quadakkers, Correlative Atom Probe Tomography and Transmission Electron Microscopy Analysis of Grain Boundaries in Thermally Grown Alumina Scale, Microscopy and Microanalysis 25 (2019) 11–20. https://doi.org/10.1017/S143192761801557X.

[147] M. Herbig, A. Kumar, Removal of hydrocarbon contamination and oxide films from atom probe specimens, Microscopy Research and Technique 84 (2021) 291–297. https://doi.org/10.1002/JEMT.23587.

[148] K. Babinsky, R. De Kloe, H. Clemens, S. Primig, A novel approach for site-specific atom probe specimen preparation by focused ion beam and transmission electron backscatter diffraction., Ultramicroscopy 144 (2014) 9–18. https://doi.org/10.1016/j.ultramic.2014.04.003.

[149] A.J. Breen, K. Babinsky, A.C. Day, K. Eder, C.J. Oakman, P.W. Trimby, S. Primig, J.M. Cairney, S.P. Ringer, Correlating Atom Probe Crystallographic Measurements with Transmission Kikuchi Diffraction Data, Microsc. Microanal. 0 (2017) 1–12. https://doi.org/10.1017/S1431927616012605.

[150] T. Schwarz, G. Stechmann, B. Gault, O. Cojocaru-Mirédin, R. Wuerz, D. Raabe, Correlative transmission Kikuchi diffraction and atom probe tomography study of Cu(In,Ga)Se<inf>2</inf> grain boundaries, Progress in Photovoltaics: Research and Applications 26 (2018) 196–204. https://doi.org/10.1002/pip.2966.

[151] B. Gault, H. Khanchandani, T.S. Prithiv, S. Antonov, T.B. Britton, Transmission Kikuchi Diffraction Mapping Induces Structural Damage in Atom Probe Specimens, Microscopy and Microanalysis 29 (2023) 1026–1036. https://doi.org/10.1093/micmic/ozad029.

[152] L. Rigutti, A. Vella, F. Vurpillot, A. Gaillard, N. Sevelin-Radiguet, J. Houard, A. Hideur, G. Martel, G. Jacopin, A. De Luna Bugallo, B. Deconihout, Coupling atom probe tomography and photoluminescence spectroscopy: exploratory results and perspectives., Ultramicroscopy 132 (2013) 75–80. https://doi.org/10.1016/j.ultramic.2013.02.002.

[153] B. Gault, K. Schweinar, S. Zhang, L. Lahn, C. Scheu, S.-H. Kim, O. Kasian, Correlating atom probe tomography with x-ray and electron spectroscopies to understand microstructure–activity relationships in electrocatalysts, MRS Bulletin 2022 (2022) 1–9. https://doi.org/10.1557/S43577-022-00373-8.

[154] A. BalaKrishnan, N. Blanc, U. Hagemann, P. Gemagami, K. Wonner, K. Tschulik, T. Li, Direct Detection of Surface Species Formed on Iridium Electrocatalysts during the Oxygen Evolution Reaction, Angewandte Chemie - International Edition 60 (2021) 21396–21403. https://doi.org/10.1002/anie.202106790.

[155] Y.-S. Chen, D. Haley, S.S.A. Gerstl, A.J. London, F. Sweeney, R.A. Wepf, W.M. Rainforth, P.A.J. Bagot, M.P. Moody, Direct observation of individual hydrogen atoms at trapping sites in a ferritic steel, Science 355 (2017) 1196–1199.

[156] D.E. Perea, D.K. Schreiber, J.V. Ryan, M.G. Wirth, L. Deng, X. Lu, J. Du, J.D. Vienna, Tomographic mapping of the nanoscale water-filled pore structure in corroded borosilicate glass, Npj Materials Degradation 4 (2020) 1–7. https://doi.org/10.1038/s41529-020-0110-5.

[157] A.A. El-Zoka, S.-H. Kim, S. Deville, R.C. Newman, L.T. Stephenson, B. Gault, Enabling near-atomic–scale analysis of frozen water, Science Advances 6 (2020) eabd6324. https://doi.org/10.1126/sciadv.abd6324.

[158] S.-H. Kim, K. Dong, H. Zhao, A.A. El-Zoka, X. Zhou, E.V. Woods, F. Giuliani, I. Manke, D. Raabe, B. Gault, Understanding the Degradation of a Model Si Anode in a Li-Ion Battery at the Atomic Scale, J. Phys. Chem. Lett. 13 (2022) 8416–8421. https://doi.org/10.1021/acs.jpclett.2c02236.

[159] T.M. Schwarz, E.M. Weikum, K. Meng, E. Hadjixenophontos, C.A. Dietrich, J. Kästner, P. Stender, G. Schmitz, Field evaporation and atom probe tomography of pure water tips, Scientific Reports 10 (2020) 20271.

[160] N.A.A.N.A. Rivas, A. Babayigit, B. Conings, T. Schwarz, A. Sturm, A.G.G. Manjón, O. Cojocaru-Mirédin, B. Gault, F.U. Renner, Cryo-focused ion beam preparation of perovskite based solar cells for atom probe tomography, PLoS ONE 15 (2020) e0227920. https://doi.org/10.1371/journal.pone.0227920.

[161] L. Lilensten, B. Gault, New approach for FIB-preparation of atom probe specimens for aluminum alloys, PLoS ONE 15 (2020). https://doi.org/10.1371/journal.pone.0231179.

[162] Y. Chang, W. Lu, J. Guénolé, L.T. Stephenson, A. Szczpaniak, P. Kontis, A.K. Ackerman, F. Dear, I. Mouton, X. Zhong, D. Raabe, B. Gault, S. Zhang, D. Dye, C.H. Liebscher, D. Ponge, S. Korte-Kerze, D. Raabe, B. Gault, Ti and its alloys as examples of cryogenic focused ion beam milling of environmentally-sensitive materials, Nature Communications 10 (2019) 942. https://doi.org/10.1038/s41467-019-08752-7.

[163] I. Mouton, Y. Chang, P. Chakraborty, S. Wang, L.T. Stephenson, T. Ben Britton, B. Gault, Hydride growth mechanism in zircaloy-4: Investigation of the partitioning of alloying elements, Materialia 15 (2021) 101006. https://doi.org/10.1016/j.mtla.2021.101006.

[164] S.H. Kim, L.T. Stephenson, A.K. da Silva, B. Gault, A.A. El-Zoka, Phase separation and anomalous shape transformation in frozen microscale eutectic indium-gallium upon remelting, Materialia 26 (2022) 101595. https://doi.org/10.1016/J.MTLA.2022.101595.

[165] T.M. Schwarz, J. Ott, H. Solodenko, G. Schmitz, P. Stender, Nanoscale analysis of frozen honey by atom probe tomography, Scientific Reports 2022 12:1 12 (2022) 1–14. https://doi.org/10.1038/s41598-022-22717-9.

[166] T.M. Schwarz, C.A. Dietrich, J. Ott, E.M. Weikum, R. Lawitzki, H. Solodenko, E. Hadjixenophontos, B. Gault, J. Kästner, G. Schmitz, P. Stender, 3D sub-nanometer analysis of glucose in an aqueous solution by cryo-atom probe tomography, Scientific Reports 2021 11:1 11 (2021) 1–19. https://doi.org/10.1038/s41598-021-90862-8.

[167] E.V. Woods, M.P. Singh, S.-H. Kim, T.M. Schwarz, J.O. Douglas, A.A. El-Zoka, F. Giulani, B. Gault, A Versatile and Reproducible Cryo-sample Preparation Methodology for Atom Probe Studies, Microscopy and Microanalysis (2023) ozad120. https://doi.org/10.1093/micmic/ozad120.

[168] D.K. Schreiber, D.E. Perea, J.V. Ryan, J.E. Evans, J.D. Vienna, A method for site-specific and cryogenic specimen fabrication of liquid/solid interfaces for atom probe tomography, Ultramicroscopy 194 (2018) 89–99. https://doi.org/10.1016/J.ULTRAMIC.2018.07.010.

[169] J.O. Douglas, M. Conroy, F. Giuliani, B. Gault, In Situ Sputtering From the Micromanipulator to Enable Cryogenic Preparation of Specimens for Atom Probe Tomography by Focused-Ion Beam, Microscopy and Microanalysis 29 (2023) 1009–1017. https://doi.org/10.1093/micmic/ozad020.

[170] D.J. Larson, Local electrode atom probe tomography : a user's guide, Springer, 2013.

[171] J.B. Seol, C.M. Kwak, Y.T. Kim, C.G. Park, Understanding of the field evaporation of surface modified oxide materials through transmission electron microscopy and atom probe tomography, Applied Surface Science 368 (2016) 368–377.

[172] T.J. Wilkes, J.M. Titchmar, G.D.W. Smith, D.A. Smith, R.F. Morris, S. Johnston, T.J. Godfrey, P. Birdseye, Fracture of Field-Ion Microscope Specimens, Journal of Physics D-Applied Physics 5 (1972) 2226–2230.

[173] C.K.S. Moy, G. Ranzi, T.C. Petersen, S.P. Ringer, Macroscopic electrical field distribution and field-induced surface stresses of needle-shaped field emitters, Ultramicroscopy 111 (2011) 397–404.

[174] S.D. Taylor, J. Liu, B.W. Arey, D.K. Schreiber, D.E. Perea, K.M. Rosso, Resolving Iron(II) Sorption and Oxidative Growth on Hematite (001) Using Atom Probe Tomography, Journal of Physical Chemistry C 122 (2018) 3903–3914. https://doi.org/10.1021/acs.jpcc.7b11989.

[175] P. Felfer, P. Benndorf, A. Masters, T. Maschmeyer, J.M. Cairney, Revealing the distribution of the atoms within individual bimetallic catalyst nanoparticles., Angewandte Chemie (International Ed. in English) 53 (2014) 11190–11193. https://doi.org/10.1002/anie.201405043.

[176] S. Kim, S. Antonov, X. Zhou, L. Stephenson, C. Jung, A. El-Zoka, D.K. Schreiber, S. Conroy, B. Gault, J. Mater, S.-H. Kim, S. Antonov, X. Zhou, L.T. Stephenson, C. Jung, A.A. El-Zoka, D.K. Schreiber, M. Conroy, B. Gault, Atom probe analysis of electrode materials for Li-ion batteries: challenges and ways forward, Journal of Materials Chemistry A 6 (2022) 4883–5230. https://doi.org/10.1039/D1TA10050E.

[177] D.S. Mosiman, Y.-S. Chen, L. Yang, B. Hawkett, S.P. Ringer, B.J. Mariñas, J.M. Cairney, Atom Probe Tomography of Encapsulated Hydroxyapatite Nanoparticles, Small Methods 5 (2021) 2000692. https://doi.org/10.1002/smtd.202000692.

[178] V.R. Adineh, R.K.W. Marceau, Y. Chen, K.J. Si, T. Velkov, W. Cheng, J. Li, J. Fu, Pulsed-voltage atom probe tomography of low conductivity and insulator materials by application of ultrathin metallic coating on nanoscale specimen geometry, Ultramicroscopy 181 (2017) 150–159. https://doi.org/10.1016/j.ultramic.2017.05.002.

[179] S. Qiu, V. Garg, S. Zhang, Y. Chen, J. Li, A. Taylor, R.K.W. Marceau, J. Fu, Graphene encapsulation enabled high-throughput atom probe tomography of liquid specimens, Ultramicroscopy (2020) 113036. https://doi.org/10.1016/j.ultramic.2020.113036.

[180] S. Kölling, W. Vandervorst, Failure mechanisms of silicon-based atom-probe tips, Ultramicroscopy 109 (2009) 486–491. https://doi.org/10.1016/J.ULTRAMIC.2008.11.013.

[181] T.M. Schwarz, E. Woods, M.P. Singh, C. Jung, L.S. Aota, K. Jang, M. Krämer, S.-H. Kim, I. McCarroll, B. Gault, In-situ metallic coating of atom probe specimen for enhanced yield, performance, and increased field-of-view, (2023). https://doi.org/10.48550/arXiv.2309.07836.

[182] A. Saksena, B. Sun, X. Dong, H. Khanchandani, D. Ponge, B. Gault, Optimizing site-specific specimen preparation for atom probe tomography by using hydrogen for visualizing radiation-induced damage, International Journal of Hydrogen Energy (2023). https://doi.org/10.1016/j.ijhydene.2023.09.057.

[183] M.P. Singh, S.-H. Kim, X. Zhou, H. Kwak, A.K. da Silva, S. Antonov, L.S. Aota, C. Jung, Y.S. Jung, B. Gault, Near-Atomic-Scale Evolution of the Surface Chemistry in Li[Ni,Mn,Co]O2 Cathode for Li-Ion Batteries Stored in Air, Advanced Energy and Sustainability Research (2022) 2200121. https://doi.org/10.1002/AESR.202200121.

[184] B. Pfeiffer, J. Maier, J. Arlt, C. Nowak, In Situ Atom Probe Deintercalation of Lithium-Manganese-Oxide, Microscopy and Microanalysis 23 (2017) 314–320. https://doi.org/10.1017/S1431927616012691.

[185] D. Santhanagopalan, D.K. Schreiber, D.E. Perea, R.L. Martens, Y. Janssen, P. Khalifah, Y.S. Meng, Effects of laser energy and wavelength on the analysis of $LiFePO_4$ using laser assisted atom probe tomography., Ultramicroscopy 148 (2015) 57–66. https://doi.org/10.1016/j.ultramic.2014.09.004.

[186] S.-H. Kim, K. Shin, X. Zhou, C. Jung, H.Y. Kim, S. Pedrazzini, M. Conroy, G. Henkelman, B. Gault, Atom probe analysis of BaTiO3 enabled by metallic shielding, Scripta Materialia 229 (2023) 115370. https://doi.org/10.1016/j.scriptamat.2023.115370.

[187] M.P. Singh, E.V. Woods, S.-H. Kim, C. Jung, L.S. Aota, B. Gault, Facilitating the Systematic Nanoscale Study of Battery Materials by Atom Probe Tomography through in-situ Metal Coating, Batteries & Supercaps n/a (n.d.) e202400015. https://doi.org/10.1002/batt.202400015.

[188] J. Dubochet, A Reminiscence about Early Times of Vitreous Water in Electron Cryomicroscopy, Biophysical Journal 110 (2016) 756–757. https://doi.org/10.1016/J.BPJ.2015.07.049.

[189] J.T. Sebastian, O.C. Hellman, D.N. Seidman, New method for the calibration of three-dimensional atom-probe mass spectra, Review of Scientific Instruments 72 (2001) 2984–2988.

[190] D.R. Kingham, The post-ionization of field evaporated ions: A theoretical explanation of multiple charge states, Surface Science 116 (1982) 273–301. https://doi.org/10.1016/0039-6028(82)90434-4.

[191] T.T. Tsong, Observation of doubly charged diatomic cluster ions of a metal, Journal of Chemical Physics 85 (1986) 639–640.

[192] A. Cerezo, C.R.M. Grovenor, R.M. Hoyle, G.D.W. Smith, Atom probe analysis of a ceramic oxide superconductor, Applied Physics Letters 52 (1988) 1020. https://doi.org/10.1063/1.99232.

[193] B. Gault, A. Menand, F. de Geuser, B. Deconihout, R. Danoix, F. de Geuser, B. Deconihout, R. Danoix, Investigation of an oxide layer by femtosecond-laser-assisted atom probe tomography, Applied Physics Letters 88 (2006) 114101. https://doi.org/10.1063/1.2186394.

[194] M.J. Galtrey, R.A. Oliver, M.J. Kappers, C.J. Humphreys, D.J. Stokes, P.H. Clifton, A. Cerezo, Three-dimensional atom probe studies of an InxGa1-xN/GaN multiple quantum well structure: Assessment of possible indium clustering, Applied Physics Letters 90 (2007) 61903. https://doi.org/10.1063/1.2431573.

[195] M. Thuvander, J. Weidow, J. Angseryd, L.K.L. Falk, F. Liu, M. Sonestedt, K. Stiller, H.-O. Andrén, Quantitative atom probe analysis of carbides., Ultramicroscopy 111 (2011) 604–608. https://doi.org/10.1016/j.ultramic.2010.12.024.

[196] D. Hudson, G.D.W.D.W.D.W. Smith, B. Gault, Optimisation of mass ranging for atom probe microanalysis and application to the corrosion processes in Zr alloys, Ultramicroscopy 111 (2011) 480–486. https://doi.org/10.1016/j.ultramic.2010.11.007.

[197] R.M. Ulfig, T.F. Kelly, B. Gault, Promoting Standards in Quantitative Atom Probe Tomography Analysis, Microscopy and Microanalysis 15 (2009) 260–261. https://doi.org/10.1017/S143192760909881X.

[198] D. Haley, P. Choi, D. Raabe, Guided mass spectrum labelling in atom probe tomography., Ultramicroscopy (2015). https://doi.org/10.1016/j.ultramic.2015.03.005.

[199] J.W. Valley, A.J. Cavosie, T. Ushikubo, D.A. Reinhard, D.F. Lawrence, D.J. Larson, P.H. Clifton, T.F. Kelly, S.A. Wilde, D.E. Moser, M.J. Spicuzza, Hadean age for a post-magma-ocean zircon confirmed by atom-probe tomography, Nature Geoscience 7 (2014) 219–223. https://doi.org/10.1038/ngeo2075.

[200] M.J. Lloyd, R.G. Abernethy, M.R. Gilbert, I. Griffiths, P.A.J. Bagot, D. Nguyen-Manh, M.P. Moody, D.E.J. Armstrong, Decoration of voids with rhenium and osmium transmutation products in neutron irradiated single crystal tungsten, Scripta Materialia 173 (2019) 96–100. https://doi.org/10.1016/j.scriptamat.2019.07.036.

[201] P.D.P.D. Edmondson, B. Gault, M.R.M.R. Gilbert, An atom probe tomography and inventory calculation examination of second phase precipitates in neutron irradiated

single crystal tungsten, Nuclear Fusion 60 (2020) 126013. https://doi.org/10.1088/1741-4326/abb149.

[202] B. Gault, A. Chiaramonti, O. Cojocaru-Mirédin, P. Stender, R. Dubosq, C. Freysoldt, S.K. Makineni, T. Li, M. Moody, J.M. Cairney, Atom Probe Tomography, Nature Reviews, Methods Primers (2021) 1–51.

[203] A. Koprek, O. Cojocaru-Miredin, R. Wuerz, C. Freysoldt, B. Gault, D. Raabe, Cd and Impurity Redistribution at the CdS/CIGS Interface after Annealing of CIGS-Based Solar Cells Resolved by Atom Probe Tomography, IEEE Journal of Photovoltaics 7 (2017) 313–321. https://doi.org/10.1109/JPHOTOV.2016.2629841.

[204] A.J. London, D. Haley, M.P. Moody, Single-Ion Deconvolution of Mass Peak Overlaps for Atom Probe Microscopy, Microscopy and Microanalysis 23 (2017) 300–306. https://doi.org/doi:10.1017/S1431927616012782.

[205] Y. Wei, R.S. Varanasi, T. Schwarz, L. Gomell, H. Zhao, D.J. Larson, B. Sun, G. Liu, H. Chen, D. Raabe, B. Gault, Machine-learning-enhanced time-of-flight mass spectrometry analysis, Patterns 2 (2021) 100192. https://doi.org/10.1016/j.patter.2020.100192.

[206] T.J. Wilkes, G.D.W. Smith, D.A. Smith, I. Martin, L. Renaud, A. Bostel, D. Haley, S.P. Ringer, On the quantitative analysis of field-ion micrographs, Metallography 7 (1974) 403–430. https://doi.org/10.1016/0026-0800(74)90041-X.

[207] R. Smith, J.M. Walls, Ion trajectories in field-ion microscope, Journal of Physics D-Applied Physics 11 (1978) 409–419.

[208] A. Cerezo, P.J. Warren, G.D.W. Smith, Some aspects of image projection in the field-ion microscope, Ultramicroscopy 79 (1999) 251–257. https://doi.org/10.1016/S0304-3991(99)00071-6.

[209] F. De Geuser, B. Gault, Reflections on the Projection of Ions in Atom Probe Tomography, Microscopy and Microanalysis 23 (2017) 238–246. https://doi.org/10.1017/S1431927616012721.

[210] B.P. Geiser, D.J. Larson, E. Oltman, S.S. Gerstl, D.A. Reinhard, T.F. Kelly, T.J. Prosa, Wide-Field-of-View Atom Probe Reconstruction, Microscopy and Microanalysis 15 (suppl (2009) 292–293.

[211] B. Gault, D. Haley, F. De Geuser, M.P. Moody, E.A. Marquis, D.J. Larson, B.P. Geiser, Advances in the reconstruction of atom probe tomography data., Ultramicroscopy 111 (2011) 448–457. https://doi.org/10.1016/j.ultramic.2010.11.016.

[212] J.M. Hyde, A. Cerezo, R.P. Setna, P.J. Warren, G.D.W. Smith, Lateral and depth scale calibration of the position sensitive atom probe, Applied Surface Science 76/77 (1994) 382–391.

[213] S.T. Loi, B. Gault, S.P. Ringer, D.J. Larson, B.P. Geiser, Electrostatic simulations of a local electrode atom probe: the dependence of tomographic reconstruction parameters on specimen and microscope geometry., Ultramicroscopy 132 (2013) 107–113. https://doi.org/10.1016/j.ultramic.2012.12.012.

[214] B. Gault, S.T. Loi, icente J. Araullo-Peters, L.T. Stephenson, M.P. Moody, S.L. Shrestha, R.K.W. Marceau, L. Yao, J.M. Cairney, S.P. Ringer, Dynamic reconstruction for atom

probe tomography, Ultramicroscopy 111 (2011) 1619–1624. https://doi.org/10.1016/j.ultramic.2011.08.005.

[215] C. Hatzoglou, G. Da Costa, P. Wells, X. Ren, B.P. Geiser, D.J. Larson, R. Demoulin, K. Hunnestad, E. Talbot, B. Mazumder, D. Meier, F. Vurpillot, Introducing a Dynamic Reconstruction Methodology for Multilayered Structures in Atom Probe Tomography, Microscopy and Microanalysis 29 (2023) 1124–1136. https://doi.org/10.1093/micmic/ozad054.

[216] G. Sha, L. Yao, X. Liao, S.P. Ringer, Z. Chao Duan, T.G. Langdon, Segregation of solute elements at grain boundaries in an ultrafine grained Al-Zn-Mg-Cu alloy, Ultramicroscopy 111 (2011) 500–505.

[217] O.C. Hellman, J.A. Vandenbroucke, J. Rüsing, D. Isheim, D.N. Seidman, Analysis of three-dimensional atom-probe data by the proximity histogram, Microscopy and Microanalysis 6 (2000) 437–444.

[218] B. Gault, F. Scenini, M.P. Moody, J.H. Huang, G.A. Botton, D. Mangelinck, M. Descoins, R.C. Newman, Atom Probe Characterization of Corroded Alloy 600, Microscopy and Microanalysis 19 (2013) 1020–1021. https://doi.org/10.1017/S1431927613007095.

[219] B. Gault, A Brief Overview of Atom Probe Tomography Research, Applied Microscopy 46 (2016) 117–126. https://doi.org/10.9729/AM.2016.46.3.117.

[220] L.T. Stephenson, M.P. Moody, P.V. Liddicoat, S.P. Ringer, New techniques for the analysis of fine-scaled clustering phenomena within atom probe tomography (APT) data., Microscopy and Microanalysis 13 (2007) 448–463. https://doi.org/10.1017/S1431927607070900.

[221] T. Philippe, F. De Geuser, S. Duguay, W. Lefebvre, O. Cojocaru-Miredin, G. Da Costa, D. Blavette, O. Cojocaru-Mirédin, G. Da Costa, D. Blavette, Clustering and nearest neighbour distances in atom-probe tomography, Ultramicroscopy 109 (2009) 1304–1309. https://doi.org/10.1016/j.ultramic.2009.06.007.

[222] F. De Geuser, W. Lefebvre, Determination of Matrix Composition Based on Solute-Solute Nearest-Neighbor Distances in Atom Probe Tomography, Microscopy Research and Technique 74 (2011) 257–263. https://doi.org/10.1002/jemt.20899.

[223] L. Morsdorf, E. Emelina, B. Gault, M. Herbig, C.C. Tasan, Carbon redistribution in quenched and tempered lath martensite, Acta Materialia (2020) 116521. https://doi.org/10.1016/j.actamat.2020.116521.

[224] J.M. Hyde, C.A. English, An Analysis of the Structure of Irradiation Induced Cu-Enriched Clusters in Low and High Nickel Welds, Materials Research Society Symposium Proceedings 650 (2001) 6--6.

[225] M.K. Miller, E.A. Kenik, Atom probe tomography: a technique for nanoscale characterization., in: Microscopy and Microanalysis : The Official Journal of Microscopy Society of America, Microbeam Analysis Society, Microscopical Society of Canada, 2002: pp. 1126–1127. https://doi.org/10.1017/S1431927604040577.

[226] D. Vaumousse, A. Cerezo, P.J. Warren, A procedure for quantification of precipitate microstructures from three-dimensional atom probe data, Ultramicroscopy, 95, Unknown 215 (2003) 7.

[227] E.A. Marquis, J.M. Hyde, Applications of atom-probe tomography to the characterisation of solute behaviours, Materials Science and Engineering: R: Reports 69 (2010) 37–62.

[228] P. Dumitraschkewitz, S.S.A. Gerstl, L.T. Stephenson, P.J. Uggowitzer, S. Pogatscher, Clustering in Age-Hardenable Aluminum Alloys, Advanced Engineering Materials 20 (2018) 1800255. https://doi.org/10.1002/adem.201800255.

[229] I. Ghamarian, E.A. Marquis, Hierarchical density-based cluster analysis framework for atom probe tomography data, Ultramicroscopy 200 (2019) 28–38. https://doi.org/10.1016/j.ultramic.2019.01.011.

[230] J. Zelenty, A. Dahl, J. Hyde, G.D.W. Smith, M.P. Moody, Detecting Clusters in Atom Probe Data with Gaussian Mixture Models, Microscopy and Microanalysis 23 (2017) 269–278. https://doi.org/10.1017/S1431927617000320.

[231] R.A. Karnesky, C.K. Sudbrack, D.N. Seidman, Best-fit ellipsoids of atom-probe tomographic data to study coalescence of gamma ’ (L1(2)) precipitates in Ni-Al-Cr, Scripta Materialia 57 (2007) 353–356. https://doi.org/10.1016/j.scriptamat.2007.04.020.

[232] R.K.W. Marceau, L.T. Stephenson, C.R. Hutchinson, S.P. Ringer, Quantitative atom probe analysis of nanostructure containing clusters and precipitates with multiple length scales, Ultramicroscopy 111 (2011) 738–742.

[233] C. Sudbrack, R. Noebe, D. Seidman, Direct observations of nucleation in a nondilute multicomponent alloy, Physical Review B 73 (2006) 212101. https://doi.org/10.1103/PhysRevB.73.212101.

[234] D. Haley, T. Petersen, G. Barton, S.P. Ringer, Influence of field evaporation on Radial Distribution Functions in Atom Probe Tomography, Philosophical Magazine 89 (2009) 925–943. https://doi.org/10.1080/14786430902821610.

[235] F. De Geuser, W. Lefebvre, D. Blavette, 3D atom probe study of solute atoms clustering during natural ageing and pre-ageing of an Al-Mg-Si alloy, Philosophical Magazine Letters 86 (2006) 227–234. https://doi.org/10.1080/09500830600643270.

[236] F. Vurpillot, A. Bostel, D. Blavette, Trajectory overlaps and local magnification in three-dimensional atom probe, Applied Physics Letters 76 (2000) 3127–3129.

[237] J.M. Hyde, E.A. Marquis, K.B. Wilford, T.J. Williams, A sensitivity analysis of the maximum separation method for the characterisation of solute clusters, Ultramicroscopy 111 (2011) 440–447. https://doi.org/10.1016/J.ULTRAMIC.2010.12.015.

[238] R.P. Kolli, D.N. Seidman, Comparison of compositional and morphological atom-probe tomography analyses for a multicomponent Fe-Cu steel., Microscopy and Microanalysis : The Official Journal of Microscopy Society of America, Microbeam Analysis Society, Microscopical Society of Canada 13 (2007) 272–284. https://doi.org/10.1017/S1431927607070675.

[239] C.A. Williams, D. Haley, E.A. Marquis, G.D.W.W. Smith, M.P. Moody, Y. Wu, G.R. Odette, T. Yoshiie, Y. Nishiyama, K. Onizawa, N. Castin, L. Malerba, P. Pareige, Defining clusters

in APT reconstructions of ODS steels., Ultramicroscopy 132 (2013) 271–278. https://doi.org/10.1016/j.ultramic.2012.12.011.

[240] A. Cerezo, L. Davin, Aspects of the observation of clusters in the 3-dimensional atom probe, Surface and Interface Analysis 39 (2007) 184–188. https://doi.org/10.1002/sia.2486.

[241] T. Boll, T. Al-Kassab, Y. Yuan, Z.G. Liu, Investigation of the site occupation of atoms in pure and doped TiAl/Ti3Al intermetallic., Ultramicroscopy 107 (2007) 796–801. https://doi.org/10.1016/j.ultramic.2007.02.011.

[242] B.P. Geiser, T.F. Kelly, D.J. Larson, J. Schneir, J.P. Roberts, Spatial Distribution Maps for Atom Probe Tomography, Microscopy and Microanalysis 13 (2007) 437–447. https://doi.org/10.1017/S1431927607070948.

[243] M.P. Moody, B. Gault, L.T. Stephenson, D. Haley, S.P. Ringer, Qualification of the tomographic reconstruction in atom probe by advanced spatial distribution map techniques., Ultramicroscopy 109 (2009) 815–824. https://doi.org/10.1016/j.ultramic.2009.03.016.

[244] F. Vurpillot, F. De Geuser, G. Da Costa, D. Blavette, Application of Fourier transform and autocorrelation to cluster identification in the three-dimensional atom probe., Journal of Microscopy 216 (2004) 234–240. https://doi.org/10.1111/j.0022-2720.2004.01413.x.

[245] L. Yao, M.P. Moody, J.M. Cairney, D. Haley, A.V. Ceguerra, C. Zhu, S.P. Ringer, Crystallographic structural analysis in atom probe microscopy via 3D Hough transformation, Ultramicroscopy 111 (2011) 458–463.

[246] B. Gault, M.P. Moody, F. de Geuser, G. Tsafnat, A.L. Fontaine, L.T. Stephenson, D. Haley, S.P. Ringer, Advances in the calibration of atom probe tomographic reconstruction, Journal of Applied Physics 105 (2009) 034913. https://doi.org/10.1063/1.3068197.

[247] M.P.M.P. Moody, L.T.L.T. Stephenson, P.V.P.V. Liddicoat, S.P.S.P. Ringer, Contingency table techniques for three dimensional atom probe tomography., Microscopy Research and Technique 70 (2007) 258–268. https://doi.org/10.1002/jemt.20412.

[248] M.P. Moody, L.T. Stephenson, A.V. Ceguerra, S.P. Ringer, Quantitative binomial distribution analyses of nanoscale like-solute atom clustering and segregation in atom probe tomography data., Microscopy Research and Technique 71 (2008) 542–550. https://doi.org/10.1002/jemt.20582.

[249] O.C. Hellman, J.B. du Rivage, D.N. Seidman, Efficient sampling for three-dimensional atom probe microscopy data, Ultramicroscopy 95 (2003) 199–205. https://doi.org/10.1016/S0304-3991(02)00317-0.

[250] K.E. Yoon, R.D. Noebe, O.C. Hellman, D.N. Seidman, Dependence of interfacial excess on the threshold value of the isoconcentration surface, in: Surface and Interface Analysis, 2004: pp. 594–597. http://www.scopus.com/inward/record.url?eid=2-s2.0-3042658382&partnerID=tZOtx3y1.

[251] P. Felfer, J. Cairney, Advanced concentration analysis of atom probe tomography data: Local proximity histograms and pseudo-2D concentration maps, Ultramicroscopy 189 (2018) 61–64. https://doi.org/10.1016/j.ultramic.2018.03.011.

[252] T.L. Martin, A. Radecka, L. Sun, T. Simm, D. Dye, K. Perkins, B. Gault, M.P. Moody, P.A.J. Bagot, Insights into microstructural interfaces in aerospace alloys characterised by atom probe tomography, Materials Science and Technology (United Kingdom) 32 (2016) 232–241. https://doi.org/10.1179/1743284715Y.0000000132.

[253] P. Felfer, B. Scherrer, J. Demeulemeester, W. Vandervorst, J.M. Cairney, Mapping interfacial excess in atom probe data, Ultramicroscopy 159 (2015) 438–444. https://doi.org/10.1016/j.ultramic.2015.06.002.

[254] Z. Peng, Y. Lu, C. Hatzoglou, A. Kwiatkowski Da Silva, F. Vurpillot, D. Ponge, D. Raabe, B. Gault, An Automated Computational Approach for Complete In-Plane Compositional Interface Analysis by Atom Probe Tomography, Microscopy and Microanalysis 25 (2019) 389–400. https://doi.org/10.1017/S1431927618016112.

[255] L. Yao, S.P. Ringer, J.M. Cairney, M.K. Miller, The anatomy of grain boundaries: Their structure and atomic-level solute distribution, Scripta Materialia 69 (2013) 622–625. https://doi.org/10.1016/j.scriptamat.2013.07.013.

[256] F. De Geuser, B. Gault, A. Bostel, F. Vurpillot, Correlated field evaporation as seen by atom probe tomography, Surface Science 601 (2007) 536–543. https://doi.org/10.1016/j.susc.2006.10.019.

[257] S. Katnagallu, M. Dagan, S. Parviainen, A. Nematollahi, B. Grabowski, P.A.J.A.J. Bagot, N. Rolland, J. Neugebauer, D. Raabe, F. Vurpillot, M.P.P. Moody, B. Gault, Impact of local electrostatic field rearrangement on field ionization, Journal of Physics D: Applied Physics 51 (2018) 105601. https://doi.org/10.1088/1361-6463/aaaba6.

[258] M. Müller, D.W. Saxey, G.D.W. Smith, B. Gault, Some aspects of the field evaporation behaviour of GaSb, Ultramicroscopy 111 (2011) 487–492. https://doi.org/10.1016/j.ultramic.2010.11.019.

[259] L. Yao, B. Gault, J.M. Cairney, S.P. Ringer, On the multiplicity of field evaporation events in atom probe: A new dimension to the analysis of mass spectra, Philosophical Magazine Letters 90 (2010) 121–129. https://doi.org/10.1080/09500830903472997.

[260] F. Meisenkothen, D.V. Samarov, I. Kalish, E.B. Steel, Exploring the accuracy of isotopic analyses in atom probe mass spectrometry, Ultramicroscopy 216 (2020) 113018. https://doi.org/10.1016/j.ultramic.2020.113018.

[261] D.W. Saxey, Correlated ion analysis and the interpretation of atom probe mass spectra, Ultramicroscopy 111 (2011) 473–479.

[262] I. Blum, L. Rigutti, F. Vurpillot, A. Vella, A. Gaillard, B. Deconihout, Dissociation dynamics of molecular ions in high DC electric field, The Journal of Physical Chemistry A 120 (2016) 3654–3662. https://doi.org/10.1021/acs.jpca.6b01791.

[263] Y.H. Chang, I. Mouton, L. Stephenson, M. Ashton, G.K. Zhang, A. Szczpaniak, W.J. Lu, D. Ponge, D. Raabe, B. Gault, Quantification of solute deuterium in titanium deuteride by atom probe tomography with both laser pulsing and high-voltage pulsing: Influence of the surface electric field, New Journal of Physics 21 (2019) 053025. https://doi.org/10.1088/1367-2630/ab1c3b.

[264] Z. Peng, D. Zanuttini, B. Gervais, E. Jacquet, I. Blum, P.P. Choi, D. Raabe, F. Vurpillot, B. Gault, Unraveling the Metastability of Cn2+ (n = 2-4) Clusters, Journal of Physical Chemistry Letters 10 (2019) 581–588. https://doi.org/10.1021/acs.jpclett.8b03449.

[265] B. Gault, D.W. Saxey, M.W. Ashton, S.B. Sinnott, A.N. Chiaramonti, M.P. Moody, D.K. Schreiber, Behavior of molecules and molecular ions near a field emitter, New Journal of Physics 18 (2016) 33031. https://doi.org/10.1088/1367-2630/18/3/033031.

[266] D. Zanuttini, I. Blum, L. Rigutti, F. Vurpillot, J. Douady, E. Jacquet, P.-M. Anglade, B. Gervais, Simulation of field-induced molecular dissociation in atom-probe tomography: Identification of a neutral emission channel, Physical Review A 95 (2017) 61401. https://doi.org/10.1103/PhysRevA.95.061401.

[267] B. Gault, M.P. Moody, F.D. Geuser, A.L. Fontaine, L.T. Stephenson, D. Haley, S.P. Ringer, Spatial Resolution in Atom Probe Tomography, Microscopy and Microanalysis 16 (2010) 99–110. https://doi.org/10.1017/S1431927609991267.

[268] F. Vurpillot, G. Da Costa, A. Menand, D. Blavette, Structural analyses in three-dimensional atom probe : a Fourier approach, Journal of Microscopy 203 (2001) 295–302.

[269] E. Cadel, F. Vurpillot, R. Larde, S. Duguay, B. Deconihout, Depth resolution function of the laser assisted tomographic atom probe in the investigation of semiconductors, Journal of Applied Physics 106 (2009) 44908.

[270] A.J.W. Moore, COMPUTER SIMULATION OF FIELD ION EMISSION PATTERNS OF SOLID SOLUTION ALLOYS, Philosophical Magazine 16 (1967) 739–747.

[271] A.J.W. Moore, The Simulation of FIM Desorption Patterns, Philosophical Magazine A-Physics of Condensed Matter Structure Defects and Mechanical Properties 43 (1981) 803–814.

[272] A.R. Waugh, E.D. Boyes, M.J. Southon, INVESTIGATIONS OF FIELD EVAPORATION WITH A FIELD-DESORPTION MICROSCOPE, Surface Science 61 (1976).

[273] F. Vurpillot, A. Bostel, D. Blavette, The shape of field emitters and the ion trajectories in three-dimensional atom probes, Journal of Microscopy 196 (1999) 332–336. https://doi.org/10.1046/j.1365-2818.1999.00637.x.

[274] C. Oberdorfer, S.M.S.M. Eich, G. Schmitz, A full-scale simulation approach for atom probe tomography, Ultramicroscopy 128 (2013) 55–67. https://doi.org/10.1016/j.ultramic.2013.01.005.

[275] F. Vurpillot, C. Oberdorfer, Modeling Atom Probe Tomography: A review, Ultramicroscopy 159 (2015) 202–216. https://doi.org/10.1016/j.ultramic.2014.12.013.

[276] N. Rolland, D.J. Larson, B.P. Geiser, S. Duguay, F. Vurpillot, D. Blavette, An analytical model accounting for tip shape evolution during atom probe analysis of heterogeneous materials., Ultramicroscopy (2015). https://doi.org/10.1016/j.ultramic.2015.03.010.

[277] C. Hatzoglou, F. Vurpillot, A Mesoscopic Field Evaporation Model, Microscopy and Microanalysis 25 (2019) 286–287. https://doi.org/10.1017/s1431927619002162.

[278] C. Fletcher, M.P. Moody, D. Haley, Fast modelling of field evaporation in atom probe tomography using level set methods, Journal of Physics D: Applied Physics 52 (2019) 435305. https://doi.org/10.1088/1361-6463/ab3703.

[279] M.A. Fortes, Shape of field-evaporated metal tips, Surface Science 28 (1971) 95–116.

[280] P.J. Birdseye, D.A. Smith, G.D.W. Smith, Analog Investigations Of Electric-Field Distribution And Ion Trajectories In Field-Ion Microscope, Journal of Physics D-Applied Physics 7 (1974) 1642–1651.

[281] L. Rousseau, A. Normand, F.F. Morgado, H.-S. Marie Scisly Søreide, L.T. Stephenson, C. Hatzoglou, G. Da Costa, K. Tehrani, C. Freysoldt, B. Gault, F. Vurpillot, Introducing field evaporation energy loss spectroscopy, Commun Phys 6 (2023) 1–8. https://doi.org/10.1038/s42005-023-01203-2.

[282] F. Vurpillot, C. Hatzoglou, B. Klaes, L. Rousseau, J.-B. Maillet, I. Blum, B. Gault, A. Cerezo, Crystallographic Dependence of Field Evaporation Energy Barrier in Metals Using Field Evaporation Energy Loss Spectroscopy Mapping, Microscopy and Microanalysis (2024) ozae083. https://doi.org/10.1093/mam/ozae083.

[283] F. Vurpillot, M. Gruber, G. Da Costa, I. Martin, L. Renaud, A. Bostel, Pragmatic reconstruction methods in atom probe tomography., Ultramicroscopy 111 (2011) 1286–1294. https://doi.org/10.1016/j.ultramic.2011.04.001.

[284] N. Rolland, F. Vurpillot, S. Duguay, D. Blavette, A Meshless Algorithm to Model Field Evaporation in Atom Probe Tomography, Microscopy and Microanalysis 21 (2015) 1649–1656. https://doi.org/10.1017/S1431927615015184.

[285] P. Panayi, P.H. Clifton, G. Lloyd, G. Shellswell, A. Cerezo, A Wide Angle Achromatic Reflectron for the Atom Probe, in: IVNC 2006 / IFES 2006, 2006: p. 63.

[286] F. De Geuser, B. Gault, Reflections on the Projection of Ions in Atom Probe Tomography, Microscopy and Microanalysis 23 (2017) 238–246. https://doi.org/10.1017/S1431927616012721.

[287] O. Nishikawa, Atomic level analysis of surfaces by a scanning atom probe (SAP), Zairyo to Kankyo/ Corrosion Engineering 48 (1999) 414–420.

[288] A. Cerezo, Development of the scanning atom probe, in: Microscopy and Microanalysis, 2003: pp. 562–563. http://www.scopus.com/inward/record.url?eid=2-s2.0-0042923088&partnerID=tZOtx3y1.

[289] F. Vurpillot, B. Gault, B.P. Geiser, D.J. Larson, Reconstructing atom probe data: A review, Ultramicroscopy 132 (2013) 19–30. https://doi.org/10.1016/j.ultramic.2013.03.010.

[290] D.J. Larson, B.P. Geiser, T.J. Prosa, S.S.A. Gerstl, D.A. Reinhard, T.F. Kelly, Improvements in planar feature reconstructions in atom probe tomography., Journal of Microscopy 243 (2011) 15–30. https://doi.org/10.1111/j.1365-2818.2010.03474.x.

[291] C.M.C. de Castilho, D.R. Kingham, Resolution of the field-ion microscope, Journal of Physics D-Applied Physics 20 (1987) 116–124.

[292] B. Gault, M. Müller, A. La Fontaine, M.P. Moody, A. Shariq, A. Cerezo, S.P. Ringer, G.D.W. Smith, Influence of surface migration on the spatial resolution of pulsed laser

atom probe tomography, Journal of Applied Physics 108 (2010) 44904. https://doi.org/10.1063/1.3462399.

[293] B. Gault, Y.M. Chen, M.P. Moody, T. Ohkubo, K. Hono, S.P. Ringer, Influence of the wavelength on the spatial resolution of pulsed-laser atom probe, Journal of Applied Physics 110 (2011) 94901. https://doi.org/10.1063/1.3657846.

[294] T. Tsong, Pulsed-laser-stimulated field ion emission from metal and semiconductor surfaces: A time-of-flight study of the formation of atomic, molecular, and cluster ions, Physical Review B 30 (1984) 4946–4961. https://doi.org/10.1103/PhysRevB.30.4946.

[295] Z. Vager, R. Naaman, E.P. Kanter, Coulomb Explosion Imaging of Small Molecules, Science 244 (1989) 426–431. https://doi.org/10.1126/science.244.4903.426.

[296] E. Di Russo, I. Blum, I. Rivalta, J. Houard, G. Da Costa, F. Vurpillot, D. Blavette, L. Rigutti, Detecting Dissociation Dynamics of Phosphorus Molecular Ions by Atom Probe Tomography, J. Phys. Chem. A 124 (2020) 10977–10988. https://doi.org/10.1021/acs.jpca.0c09259.

[297] B.W. Caplins, A.N. Chiaramonti, J.M. Garcia, L. Miaja-Avila, K.H. Yano, D.K. Schreiber, J.H. Bunton, On the instrument-dependent appearance of ion dissociation events in atom probe tomography mass spectra, Ultramicroscopy 267 (2024) 114061. https://doi.org/10.1016/j.ultramic.2024.114061.

[298] L. Arnoldi, E.P. Silaeva, F. Vurpillot, B. Deconihout, E. Cadel, I. Blum, A. Vella, Role of the resistivity of insulating field emitters on the energy of field-ionised and field-evaporated atoms, Ultramicroscopy 159 (2015) 139–146. https://doi.org/10.1016/j.ultramic.2014.11.018.

[299] S.V. Krishnaswamy, S.B. McLane, E.W. Müller, Aiming performance of the atom probe, Review of Scientific Instruments 46 (1975) 1237–1240.

[300] B. Gault, B. Klaes, F.F. Morgado, C. Freysoldt, Y. Li, F. De Geuser, L.T. Stephenson, F. Vurpillot, Reflections on the Spatial Performance of Atom Probe Tomography in the Analysis of Atomic Neighborhoods, Microsc Microanal (2021) 1–11. https://doi.org/10.1017/S1431927621012952.

[301] F. Vurpillot, A. Gaillard, G. Da Costa, B. Deconihout, A model to predict image formation in Atom probeTomography, Ultramicroscopy http://dx. (2013). http://dx.doi.org/10.1016/j.ultramic.2012.12.007.

[302] C. Fletcher, M.P. Moody, D. Haley, Towards model-driven reconstruction in atom probe tomography, Journal of Physics D: Applied Physics 53 (2020) 475303. https://doi.org/10.1088/1361-6463/abaaa6.

[303] D.J. Larson, P.P. Camus, J.L. Vargas, T.F. Kelly, M.K. Miller, Specimen preparation and atom probe field ion microscopy of BSCCO-2212 superconductors, Journal De Physique Iv 6 (1996) 271–276. https://doi.org/10.1051/jp4:1996544.

[304] M.K. Miller, The effects of local magnification and trajectory aberrations on atom probe analysis, Journal De Physique 48 (1987) 565–570.

[305] J. Perrin Toinin, C. Hatzoglou, J. Voronkoff, H. Montigaud, D. Guimard, M. Wuttig, F. Vurpillot, O. Cojocaru-Mirédin, A Quantitative Investigation of Functionalized Glazing

Stacks by Atom Probe Tomography, Advanced Materials Technologies 8 (2023) 2200922. https://doi.org/10.1002/admt.202200922.

[306] C. Fletcher, M.P. Moody, C. Fleischmann, M. Dialameh, C. Porret, B. Geiser, D. Haley, Automated calibration of model-driven reconstructions in atom probe tomography, J. Phys. D: Appl. Phys. 55 (2022) 375301. https://doi.org/10.1088/1361-6463/ac7986.

[307] C. Hatzoglou, B. Klaes, F. Delaroche, G.D. Costa, B. Geiser, M. Kühbach, P.B. Wells, F. Vurpillot, Mesoscopic modeling of field evaporation on atom probe tomography, J. Phys. D: Appl. Phys. 56 (2023) 375301. https://doi.org/10.1088/1361-6463/acd649.

[308] G. Sha, A. Cerezo, G.D.W. Smith, Field evaporation behavior during irradiation with picosecond laser pulses, Applied Physics Letters 92 (2008) 43503. https://doi.org/043503 10.1063/1.2837626.

[309] M.N. Bachhav, R. Danoix, F. Vurpillot, B. Hannoyer, S.B. Ogale, F. Danoix, Evidence of lateral heat transfer during laser assisted atom probe tomography analysis of large band gap materials, Applied Physics Letters 99 (2011) 84101. https://doi.org/10.1063/1.3622647.

[310] R.G. Forbes, Seeing atoms: the origins of local contrast in field-ion images, Journal of Physics D: Applied Physics 18 (1985) 973–1018. https://doi.org/10.1088/0022-3727/18/6/006.

[311] E.R. McMullen, J.P. Perdew, Theory of field evaporation of the surface layer in jellium and other metals, Physical Review B 36 (1987) 2598.

[312] J. Neugebauer, M. Scheffler, Theory of adsorption and desorption in high electric-fields, Surface Science 287/288 (1993) 572–576.

[313] E.R. McMullen, J.P. Perdew, J.H. Rose, Effects of an intense electric field on metal surface geometry, Solid State Communications 44 (1982) 945–949. https://doi.org/10.1016/0038-1098(82)90310-6.

[314] C. Oberdorfer, T. Withrow, L.-J.J. Yu, K. Fisher, E.A. Marquis, W. Windl, Influence of surface relaxation on solute atoms positioning within atom probe tomography reconstructions, Materials Characterization 146 (2018) 324–335. https://doi.org/10.1016/J.MATCHAR.2018.05.014.

[315] B.P. Geiser, D.J. Larson, S.S.A. Gerstl, D.A. Reinhard, T.F. Kelly, T.J. Prosa, J.D. Olson, A System for Simulation of Tip Evolution Under Field Evaporation, Microscopy and Microanalysis 15 (suppl (2009).

[316] X. Wang, C. Hatzoglou, B. Sneed, Z. Fan, W. Guo, K.K. Jin, D.D. Chen, H. Bei, Y. Wang, W.J.W.J. Weber, F. Vurpillot, J.D.J.D. Poplawsky, Y. Zhang, B. Gault, K.L. More, F. Vurpillot, J.D.J.D. Poplawsky, Interpreting nanovoids in atom probe tomography data for accurate local compositional measurements, Nature Communications 11 (2020) 1–11. https://doi.org/10.1038/s41467-020-14832-w.

[317] D.J. Rose, Magnification and resolution of the field emission electron microscope, Physical Review 27 (1955) 1169.

[318] M. Gruber, F. Vurpillot, A. Bostel, B. Deconihout, A Kinetic Monte Carlo approach on the influence of temperature, Surface Science 605 (2011) 2025–2031. https://doi.org/10.1016/j.susc.2011.07.022.

[319] C. Oberdorfer, G. Schmitz, On the Field Evaporation Behavior of Dielectric Materials in Three-Dimensional Atom Probe: A Numeric Simulation, Microscopy and Microanalysis 17 (2011) 15–25. https://doi.org/doi:10.1017/S1431927610093888.

[320] B. Gault, M.P. Moody, F. de Geuser, D. Haley, L.T. Stephenson, S.P. Ringer, Origin of the spatial resolution in atom probe microscopy, Applied Physics Letters 95 (2009) 034103. https://doi.org/10.1063/1.3182351.

[321] Aspects of the performance of a femtosecond laser-pulsed 3-dimensional atom probe, Ultramicroscopy 107 (2007) 720–725. https://doi.org/10.1016/j.ultramic.2007.02.025.

[322] Y.C. Chen, D.N. Seidman, Field ionization characteristics of individual atomic planes, Surface Science 27 (1971) 231–255.

[323] R.K.W. Marceau, A.V. Ceguerra, A.J. Breen, D. Raabe, S.P. Ringer, Quantitative chemical-structure evaluation using atom probe tomography: Short-range order analysis of Fe-Al, Ultramicroscopy 157 (2015) 12–20. https://doi.org/10.1016/j.ultramic.2015.05.001.

[324] M. He, W.J. Davids, A.J. Breen, S.P. Ringer, Quantifying short-range order using atom probe tomography, Nat. Mater. 23 (2024) 1200–1207. https://doi.org/10.1038/s41563-024-01912-1.

[325] B. Gault, B. Klaes, F.F. Morgado, C. Freysoldt, Y. Li, F. De Geuser, L.T. Stephenson, F. Vurpillot, Reflections on the spatial performance of atom probe tomography in the analysis of atomic neighbourhoods, Microscopy and Microanalysis 28 (2022) 1116–1126. https://doi.org/10.1017/S1431927621012952.

[326] Y. Li, Y. Wei, Z. Wang, X. Liu, T. Colnaghi, L. Han, Z. Rao, X. Zhou, L. Huber, R. Dsouza, Y. Gong, J. Neugebauer, A. Marek, M. Rampp, S. Bauer, H. Li, I. Baker, L.T. Stephenson, B. Gault, Quantitative three-dimensional imaging of chemical short-range order via machine learning enhanced atom probe tomography, Nat Commun 14 (2023) 7410. https://doi.org/10.1038/s41467-023-43314-y.

[327] Y. Li, T. Colnaghi, Y. Gong, H. Zhang, Y. Yu, Y. Wei, B. Gan, M. Song, A. Marek, M. Rampp, S. Zhang, Z. Pei, M. Wuttig, S. Ghosh, F. Körmann, J. Neugebauer, Z. Wang, B. Gault, Machine Learning-Enabled Tomographic Imaging of Chemical Short-Range Atomic Ordering, Advanced Materials n/a (n.d.) 2407564. https://doi.org/10.1002/adma.202407564.

[328] M.K. Miller, An atom probe study of the anomalous field evaporation of alloys containing silicon, Journal of Vacuum Science and Technology 19 (1981) 57. https://doi.org/10.1116/1.571017.

[329] B. Gault, F. Danoix, K. Hoummada, D. Mangelinck, H. Leitner, Impact of directional walk on atom probe microanalysis, Ultramicroscopy 113 (2012) 182–191. https://doi.org/10.1016/j.ultramic.2011.06.005.

[330] S.C. Wang, T.T. Tsong, Field and Temperature-Dependence of the Directional Walk of Single Adsorbed W-Atoms on the W(110) Plane, Physical Review B 26 (1982) 6470–6475.

[331] K.D. Rendulic, E.W. Müller, Elastic Deformation Of Field-Ion-Microscope Tips, Journal of Applied Physics 38 (1967) 2070–2072.

[332] K.D. Rendulic, Mechanical twinning of platinum and iridium in a field-ion microscope, Journal of the Less Common Metals 12 (1967) 441–448. https://doi.org/10.1016/0022-5088(67)90016-1.

[333] T.T. Tsong, R.J. Walko, Measurements of Polarizability of Tungsten Adatoms on Tungsten (110) Planes, Physica Status Solidi A-Applied Research 12 (1972) 111–117.

[334] F. Djurabekova, S. Parviainen, A. Pohjonen, K. Nordlund, Atomistic modeling of metal surfaces under electric fields: Direct coupling of electric fields to a molecular dynamics algorithm, Phys. Rev. E 83 (2011) 026704. https://doi.org/10.1103/PhysRevE.83.026704.

[335] S. Parviainen, F. Djurabekova, S.P. Fitzgerald, A. Ruzibaev, K. Nordlund, Atomistic simulations of field assisted evaporation in atom probe tomography, Journal of Physics D: Applied Physics 49 (2016) 45302. https://doi.org/10.1088/0022-3727/49/4/045302.

[336] S. Parviainen, M. Dagan, S. Katnagallu, B. Gault, M. Moody, F. Vurpillot, Atomistic Simulations of Surface Effects Under High Electric Fields, Microscopy and Microanalysis 23 (2017) 644–645. https://doi.org/10.1017/s1431927617003889.

[337] D. Melkonyan, ATOMIC SCALE OBSERVATION OF ATOM DISTRIBUTIONS IN 3D DEVICES USING ATOM PROBE TOMOGRAPHY, 2019. https://lirias.kuleuven.be/2850181?limo=0.

[338] P.J.P.J. Felfer, B. Gault, G. Sha, L.T. Stephenson, S.P.S.P. Ringer, J.M.J.M. Cairney, A new approach to the determination of concentration profiles in atom probe tomography., Microscopy and Microanalysis : The Official Journal of Microscopy Society of America, Microbeam Analysis Society, Microscopical Society of Canada 18 (2012) 359–364. https://doi.org/10.1017/S1431927611012530.

[339] A. Devaraj, R. Colby, F. Vurpillot, S. Thevuthasan, Understanding Atom Probe Tomography of Oxide-Supported Metal Nanoparticles by Correlation with Atomic-Resolution Electron Microscopy and Field Evaporation Simulation, The Journal of Physical Chemistry Letters 5 (2014) 1361–1367. https://doi.org/10.1021/jz500259c.

[340] M. Bachhav, G. Pawar, F. Vurpillot, R. Danoix, F. Danoix, B. Hannoyer, Y. Dong, E. Marquis, Interpreting the Presence of an Additional Oxide Layer in Analysis of Metal Oxides–Metal Interfaces in Atom Probe Tomography, J. Phys. Chem. C 123 (2019) 1313–1319. https://doi.org/10.1021/acs.jpcc.8b10895.

[341] G.-H. Greiwe, Z. Balogh, G. Schmitz, Z.B. G-H Greiwe G. Schmitz, Atom probe tomography of lithium-doped network glasses., Ultramicroscopy 141 (2014) 51–55. https://doi.org/10.1016/j.ultramic.2014.03.007.

[342] N.D. Lang, FIELD DESORPTION OF A SI ATOM FROM A METAL-SURFACE, Solid State Communications 84 (1992) 155–158.

[343] M.K. Miller, R.G. Forbes, Atom-Probe Tomography: The Local Electrode Atom Probe, 2014. https://doi.org/10.1017/S1431927604881157.

[344] D. Tománek, H.J. Kreuzer, J.H. Block, Tight-binding approach to field desorption: N2 ON Fe(111), Surface Science 157 (1985) L315--L322. https://doi.org/10.1016/0039-6028(85)90623-5.

[345] L.C. Wang, H.J. Kreuzer, Kinetic theory of field evaporation of metals, Surface Science 237 (1990) 337–346. https://doi.org/10.1016/0039-6028(90)90546-K.

[346] H.J. Kreuzer, K. Nath, Field evaporation, Surface Science 183 (1987) 591–608. https://doi.org/10.1016/S0039-6028(87)80230-3.

[347] Y. Suchorski, N. Ernst, W.A. Schmidt, V.K. Medvedev, H.J. Kreuzer, R.L.C. Wang, Field desorption and field evaporation of metals, Progress in Surface Science 53 (1996) 135–153.

[348] Y. Suchorski, W.A. Schmidt, N. Ernst, J.H. Block, H.J. Kreuzer, ELECTROSTATIC FIELDS ABOVE INDIVIDUAL ATOMS, Progress in Surface Science 48 (1995) 121–134.

[349] T. Ono, K. Hirose, First-principles study on field evaporation for silicon atom on Si(001) surface, Journal of Applied Physics 95 (2004) 1568–1571.

[350] T. Ono, T. Sasaki, J. Otsuka, K. Hirose, First-principles study on field evaporation of surface atoms from W(0 1 1) and Mo(0 1 1) surfaces, Surface Science 577 (2005) 42–46. https://doi.org/10.1016/j.susc.2004.12.024.

[351] C.G. Sanchez, A.Y. Lozovoi, A. Alavi, Field-evaporation from first-principles, Molecular Physics 102 (2004) 1045–1055. https://doi.org/10.1080/00268970410001727673.

[352] M. Tsukada, H. Tamura, K.P. McKenna, A.L. Shluger, Y.M. Chen, T. Ohkubo, K. Hono, Mechanism of laser assisted field evaporation from insulating oxides, Ultramicroscopy In Press, (2011) 567–570.

[353] M. Karahka, H.J. Kreuzer, Field evaporation of oxides: a theoretical study., Ultramicroscopy 132 (2013) 54–59. https://doi.org/10.1016/j.ultramic.2012.10.007.

[354] J. Peralta, S.R. Broderick, K. Rajan, Mapping energetics of atom probe evaporation events through first principles calculations., Ultramicroscopy 132 (2013) 143–151. https://doi.org/10.1016/j.ultramic.2013.02.007.

[355] T. Ohnuma, First-Principles Calculation of the Evaporation Field and Roll-up Effect of M (M = Fe, Cu, Si, and Mn) on the Fe (001) and Fe Step Structure, Microscopy and Microanalysis 28 (2022) 1181–1187. https://doi.org/10.1017/S1431927621000155.

[356] T. Ohnuma, Surface Diffusion of Fe and Cu on Fe (001) Under Electric Field Using First-Principles Calculations, Microscopy and Microanalysis 25 (2019) 547–553. https://doi.org/10.1017/S1431927618015738.

[357] M. Ashton, A. Mishra, J. Neugebauer, C. Freysoldt, Ab initio Description of Bond Breaking in Large Electric Fields, Physical Review Letters 124 (2020) 176801. https://doi.org/10.1103/PhysRevLett.124.176801.

[358] J. Peralta, S.R. Broderick, K. Rajan, Mapping energetics of atom probe evaporation events through first principles calculations, Ultramicroscopy 132 (2013) 143–151. https://doi.org/10.1016/j.ultramic.2013.02.007.

[359] M. Ashton, A. Mishra, J. Neugebauer, C. Freysoldt, Ab initio Description of Bond Breaking in Large Electric Fields, Phys. Rev. Lett. 124 (2020) 176801. https://doi.org/10.1103/PhysRevLett.124.176801.

[360] T. Ohnuma, First-Principles Calculation of the Evaporation Field and Roll-up Effect of M (M = Fe, Cu, Si, and Mn) on the Fe (001) and Fe Step Structure, Microsc Microanal (2021) 1–7. https://doi.org/10.1017/S1431927621000155.

[361] G.L. Kellogg, Measurement of activation energies for field evaporation of tungsten ions as a function of electric field, Phys. Rev. B 29 (1984) 4304–4312. https://doi.org/10.1103/PhysRevB.29.4304.

[362] M. Wada, On the thermally activated field evaporation of surface atoms, Surface Science 145 (1984) 451–465.

[363] X.J. Ge, N.X. Chen, W.Q. Zhang, F.W. Zhu, Selective field evaporation in field-ion microscopy for ordered alloys, Journal of Applied Physics 85 (1999) 3488–3493. https://doi.org/10.1063/1.369706.

[364] E.A. Marquis, F. Vurpillot, Chromatic aberrations in the field evaporation behavior of small precipitates., Microscopy and Microanalysis 14 (2008) 561–570. https://doi.org/10.1017/S1431927608080793.

[365] F. Vurpillot, J. Houard, A. Vella, B. Deconihout, Thermal response of a field emitter subjected to ultra-fast laser illumination, Journal of Physics D-Applied Physics 42 (2009) 125502. https://doi.org/125502 10.1088/0022-3727/42/12/125502.

[366] J. Houard, A. Vella, F. Vurpillot, B. Deconihout, Three-dimensional thermal response of a metal subwavelength tip under femtosecond laser illumination, Physical Review B 84 (2011) 33405. https://doi.org/10.1103/PhysRevB.84.033405.

[367] U. Rolander, H.-O. Andrén, Statistical correction for pile-up in the atom-probe detector system, Journal de Physique Colloques 50 (1989) C8--529-- C8--534.

[368] W. Sha, L. Chang, G.D.W. Smith, C. Liu, E.J.J. Mittemeijer, Some aspects of atom-probe analysis of Fe-C and Fe-N systems, Surface Science 266 (1992) 416–423. https://doi.org/10.1016/0039-6028(92)91055-G.

[369] M. Thuvander, A. Kvist, L.J.S. Johnson, J. Weidow, H.-O. Andrén, Reduction of multiple hits in atom probe tomography., Ultramicroscopy 132 (2013) 81–85. https://doi.org/10.1016/j.ultramic.2012.12.005.

[370] P. Ronsheim, P. Flaitz, M. Hatzistergos, C. Molella, K. Thompson, R. Alvis, Impurity measurements in silicon with D-SIMS and atom probe tomography, Applied Surface Science 255 (2008) 1547–1550. https://doi.org/10.1016/j.apsusc.2008.05.247.

[371] D. Haley, A.J. London, M.P. Moody, Processing APT Spectral Backgrounds for Improved Quantification, (2020). https://doi.org/10.1017/S1431927620024290.

[372] Y. Zhou, C. Booth-Morrison, D.N. Seidman, On the field evaporation behavior of a model Ni-Al-Cr superalloy studied by picosecond pulsed-laser atom-probe tomography., Microscopy and Microanalysis : The Official Journal of Microscopy Society of America, Microbeam Analysis Society, Microscopical Society of Canada 14 (2008) 571–580. https://doi.org/10.1017/S1431927608080963.

[373] L. Yao, J.M. Cairney, C. Zhu, S.P. Ringer, Optimisation of specimen temperature and pulse fraction in atom probe microscopy experiments on a microalloyed steel, Ultramicroscopy 111 (2011) 648–651.

[374] A.J.W. Moore, J.A. Spink, Influence of Surface Coordination on Field Evaporation Processes in Tungsten, Surface Science 44 (1974) 198–212.

[375] T.J. Wilkes, G.D.W. Smith, D.A. Smith, On the quantitative analysis of Field Ion Micrographs, Metallography 7 (1974) 403–430.

[376] B. Gault, A. La Fontaine, M.P.P.M.P. Moody, S.P.P.S.P. Ringer, E.A.A.E.A. Marquis, Impact of laser pulsing on the reconstruction in an atom probe tomography., Ultramicroscopy 110 (2010) 1215–1222. https://doi.org/10.1016/j.ultramic.2010.04.017.

[377] T.F. Kelly, B.P. Geiser, D.J. Larson, Definition of Spatial Resolution in Atom Probe Tomography, Microscopy and Microanalysis 13 (S02) (2007) 1604–1605.

[378] B.P. Geiser, J. Schneir, J.P. Roberts, S. Wiener, D.J. Larson, T.F. Kelly, D.J. Larson, J. Schneir, J.P. Roberts, Spatial Distribution Maps for Atom Probe Tomography, 2006 19th International Vacuum Nanoelectronics Conference 13 (2007) 437–447. https://doi.org/10.1017/S1431927607070948.

[379] B. Gault, M.P.M.P. Moody, F. De Geuser, D. Haley, L.T.L.T. Stephenson, S.P.S.P. Ringer, Origin of the spatial resolution in atom probe microscopy, Applied Physics Letters 95 (2009) 34103. https://doi.org/10.1063/1.3182351.

[380] B. Gault, X.Y. Cui, M.P. Moody, F. de Geuser, C. Sigli, S.P. Ringer, A. Deschamps, Atom probe tomography investigation of Mg site occupancy within delta’ precipitates in an Al-Mg-Li alloy, Scripta Materialia 66 (2012) 903–906.

[381] H.J. Im, S.K. Makineni, B. Gault, F. Stein, D. Raabe, P.-P. Choi, Elemental partitioning and site-occupancy in γ/γ′ forming Co-Ti-Mo and Co-Ti-Cr alloys, Scripta Materialia 154 (2018) 159–162. https://doi.org/10.1016/j.scriptamat.2018.05.041.

[382] Y. Li, Y. Wei, Z. Wang, X. Liu, T. Colnaghi, L. Han, Z. Rao, X. Zhou, L. Huber, R. Dsouza, Y. Gong, J. Neugebauer, A. Marek, M. Rampp, S. Bauer, H. Li, I. Baker, L.T. Stephenson, B. Gault, Quantitative three-dimensional imaging of chemical short-range order via machine learning enhanced atom probe tomography, Nat Commun 14 (2023) 7410. https://doi.org/10.1038/s41467-023-43314-y.

[383] B. Gault, M.P. Moody, J.M. Cairney, S.P. Ringer, Atom Probe Microscopy, Springer New York, New York, NY, 2012. https://doi.org/10.1007/978-1-4614-3436-8.

[384] D.J. Larson, B. Gault, B.P. Geiser, F. De Geuser, F. Vurpillot, Atom probe tomography spatial reconstruction: Status and directions, Current Opinion in Solid State and Materials Science 17 (2013) 236–247. https://doi.org/10.1016/j.cossms.2013.09.002.

[385] Y. Wei, Z. Peng, M. Kühbach, A. Breen, M. Legros, M. Larranaga, F. Mompiou, B. Gault, 3D nanostructural characterisation of grain boundaries in atom probe data utilising machine learning methods, PLOS ONE 14 (2019) e0225041. https://doi.org/10.1371/journal.pone.0225041.

[386] D. Blavette, F. Vurpillot, P. Pareige, A. Menand, A model accounting for spatial overlaps in 3D atom-probe microscopy, Ultramicroscopy 89 (2001) 145–153. https://doi.org/10.1016/S0304-3991(01)00120-6.

[387] X. Sauvage, P. Jessner, F. Vurpillot, R. Pippan, Nanostructure and properties of a Cu-Cr composite processed by severe plastic deformation, Scripta Materialia 58 (2008) 1125–1128. https://doi.org/10.1016/j.scriptamat.2008.02.010.

[388] B. Gault, F. de Geuser, L. Bourgeois, B.M.M.M. Gabble, S.P.P.P. Ringer, B.C.C.C. Muddle, Atom probe tomography and transmission electron microscopy characterisation of precipitation in an Al-Cu-Li-Mg-Ag alloy., Ultramicroscopy 111 (2011) 683–689. https://doi.org/10.1016/j.ultramic.2010.12.004.

[389] P. Sofronis, I.M. Robertson, Viable mechanisms of hydrogen embrittlement - A review, AIP Conference Proceedings 837 (2006) 64–70. https://doi.org/10.1063/1.2213060.

[390] X. Li, J. Zhang, Y. Cui, M.B. Djukic, H. Feng, Y. Wang, Review of the hydrogen embrittlement and interactions between hydrogen and microstructural interfaces in metallic alloys: Grain boundary, twin boundary, and nano-precipitate, International Journal of Hydrogen Energy 72 (2024) 74–109. https://doi.org/10.1016/j.ijhydene.2024.05.257.

[391] G.L. Kellogg, J.K.G. Panitz, A direct observation of the trapping of deuterium ions at a grain boundary in tungsten, Applied Physics Letters 37 (1980) 625. https://doi.org/10.1063/1.91999.

[392] J. Takahashi, K. Kawakami, Y. Kobayashi, T. Tarui, The first direct observation of hydrogen trapping sites in TiC precipitation-hardening steel through atom probe tomography, Scripta Materialia 63 (2010) 261–264.

[393] R. Gemma, T. Al-Kassab, R. Kirchheim, A. Pundt, Studies on hydrogen loaded V–Fe8at% films on Al2O3 substrate, Journal of Alloys and Compounds 446–447 (2007) 534–538. https://doi.org/10.1016/j.jallcom.2007.01.099.

[394] I. Mouton, A.J. Breen, S. Wang, Y. Chang, A. Szczepaniak, P. Kontis, L.T. Stephenson, D. Raabe, M. Herbig, T.B.B. Britton, B. Gault, Quantification challenges for atom probe tomography of hydrogen and deuterium in Zircaloy-4, Microscopy and Microanalysis 25 (2018) 481–488. https://doi.org/10.1017/S143192761801615X.

[395] A.J. Breen, L.T. Stephenson, B. Sun, Y. Li, O. Kasian, Solute hydrogen and deuterium observed at the near atomic scale in high - strength steel, Acta Materialia (2020). https://doi.org/10.1016/j.actamat.2020.02.004.

[396] Y.S. Chen, H. Lu, J. Liang, A. Rosenthal, H. Liu, G. Sneddon, I. McCarroll, Z. Zhao, W. Li, A. Guo, J.M. Cairney, Observation of hydrogen trapping at dislocations, grain boundaries, and precipitates, Science 367 (2020) 171–175. https://doi.org/10.1126/science.aaz0122.

[397] A.J. Breen, L.T. Stephenson, B. Sun, Y. Li, O. Kasian, D. Raabe, M. Herbig, B. Gault, Solute hydrogen and deuterium observed at the near atomic scale in high-strength steel, Acta Materialia 188 (2020) 108–120. https://doi.org/10.1016/j.actamat.2020.02.004.

[398] J. Takahashi, K. Kawakami, Y. Kobayashi, Origin of hydrogen trapping site in vanadium carbide precipitation strengthening steel, Acta Materialia 153 (2018) 193–204. https://doi.org/10.1016/j.actamat.2018.05.003.

[399] A.J. Breen, I. Mouton, W. Lu, S. Wang, A. Szczepaniak, P. Kontis, L.T.T. Stephenson, Y. Chang, A.K.K. da Silva, C.H.H. Liebscher, M. Herbig, B. Gault, A. Kwiatkowski da Silva,

C.H.H. Liebscher, D. Raabe, T.B.B. Britton, M. Herbig, B. Gault, Atomic scale analysis of grain boundary deuteride growth front in Zircaloy-4, Scripta Materialia 156 (2018) 42–46. https://doi.org/10.1016/j.scriptamat.2018.06.044.

[400] Y. Chang, A.J.A.J. Breen, Z. Tarzimoghadam, P. Kürnsteiner, H. Gardner, A. Ackerman, A. Radecka, P.A.J. Bagot, W. Lu, T. Li, E.A. Jägle, M. Herbig, L.T. Stephenson, M.P. Moody, D. Rugg, D. Dye, D. Ponge, D. Raabe, B. Gault, Characterizing solute hydrogen and hydrides in pure and alloyed titanium at the atomic scale, Acta Materialia 150 (2018) 273–280. https://doi.org/10.1016/j.actamat.2018.02.064.

[401] Steam Instruments – Pursuing high spatial resolution protein mapping through imaging mass spectrometry., (n.d.). https://steaminstruments.com/ (accessed December 20, 2020).

[402] H. Keller, G. Klingelhöfer, E. Kankeleit, A position sensitive microchannelplate detector using a delay line readout anode, Nuclear Inst. and Methods in Physics Research, A 258 (1987) 221–224. https://doi.org/10.1016/0168-9002(87)90059-3.

[403] S. Katnagallu, C. Freysoldt, B. Gault, J. Neugebauer, Ab initio vacancy formation energies and kinetics at metal surfaces under high electric field, Phys. Rev. B 107 (2023) L041406. https://doi.org/10.1103/PhysRevB.107.L041406.

[404] F.F. Morgado, S. Katnagallu, C. Freysoldt, B. Klaes, F. Vurpillot, J. Neugebauer, D. Raabe, S. Neumeier, B. Gault, L.T. Stephenson, Revealing atomic-scale vacancy-solute interaction in nickel, Scripta Materialia 203 (2021) 114036. https://doi.org/10.1016/j.scriptamat.2021.114036.

[405] C. Bacchi, G. Da Costa, F. Vurpillot, Development of an Energy Sensitive Detector for Atom Probe Tomography, in: Atom Probe Tomography and Microscopy 2020, Oxford, 2020: p. 12.

[406] F. Vurpillot, R. LARDE, B. KLAES, G.D. COSTA, Automated tomography field ion microscope, US11791129B2, 2023. https://patents.google.com/patent/US11791129B2/en (accessed February 14, 2024).

[407] B. Klaes, R. Lardé, F. Delaroche, S. Parviainen, N. Rolland, S. Katnagallu, B. Gault, F. Vurpillot, A model to predict image formation in the three-dimensional field ion microscope, Computer Physics Communications 260 (2021) 107317. https://doi.org/10.1016/j.cpc.2020.107317.

[408] S. Katnagallu, B. Gault, B. Grabowski, J. Neugebauer, D. Raabe, A. Nematollahi, Advanced data mining in field ion microscopy, Materials Characterization 146 (2018) 307–318. https://doi.org/10.1016/j.matchar.2018.02.040.

[409] M. Dagan, B. Gault, G.D.W. Smith, P.A.J. Bagot, M.P. Moody, Automated Atom-By-Atom Three-Dimensional (3D) Reconstruction of Field Ion Microscopy Data, Microscopy and Microanalysis 23 (2017) 255–268. https://doi.org/10.1017/S1431927617000277.

[410] T.F. Kelly, O. Nishikawa, J.A. Panitz, T.J. Prosa, Prospects for Nanobiology with Atom-Probe Tomography, Mrs Bulletin 34 (2009) 744–749.

[411] K. Grandfield, C. Micheletti, J. Deering, G. Arcuri, T. Tang, B. Langelier, Atom probe tomography for biomaterials and biomineralization, Acta Biomaterialia 148 (2022) 44–60. https://doi.org/10.1016/J.ACTBIO.2022.06.010.

[412] L.M. Gordon, M.J. Cohen, K.W. MacRenaris, J.D. Pasteris, T. Seda, D. Joester, Amorphous intergranular phases control the properties of rodent tooth enamel, Science 347 (2015) 746–750. https://doi.org/10.1126/science.1258950.

[413] L.M. Gordon, D. Joester, Nanoscale chemical tomography of buried organicg-inorganic interfaces in the chiton tooth, Nature 469 (2011) 194–198. https://doi.org/10.1038/nature09686.

[414] K.A. DeRocher, P.J.M. Smeets, B.H. Goodge, M.J. Zachman, P.V. Balachandran, L. Stegbauer, M.J. Cohen, L.M. Gordon, J.M. Rondinelli, L.F. Kourkoutis, D. Joester, Chemical gradients in human enamel crystallites, Nature 583 (2020) 66–71. https://doi.org/10.1038/s41586-020-2433-3.

[415] O. Nishikawa, M. Taniguchi, M. Ushirozawa, Scanning atom probe study of carbon nanotubes and graphite nanofibers with hydrogen terminated defects, Journal of Physics: Conference Series 100 (2008) 52084. https://doi.org/10.1088/1742-6596/100/5/052084.

[416] L.R.C. Wang, H.J. Kreuzer, O. Nishikawa, Polythiophene in strong electrostatic fields, Organic Electronics 7 (2006) 99–106. https://doi.org/10.1016/j.orgel.2005.11.006.

[417] T. Prosa, S. Kostrna Keeney, T.F. Kelly, Local electrode atom probe analysis of poly(3-alkylthiophene)s, Journal of Microscopy 237 (2010) 155–167.

[418] B. Gault, W. Yang, K.R.R.K.R. Ratinac, R. Zheng, F. Braet, S.P.P.S.P. Ringer, Atom probe microscopy of self-assembled monolayers: preliminary results., Langmuir : The ACS Journal of Surfaces and Colloids 26 (2010) 5291–5294. https://doi.org/10.1021/la904459k.

[419] K. Eder, P.J.J. Felfer, B. Gault, A.V.V. Ceguerra, A. La Fontaine, A.F.F. Masters, T. Maschmeyer, J.M.M. Cairney, A New Approach to Understand the Adsorption of Thiophene on Different Surfaces: An Atom Probe Investigation of Self-Assembled Monolayers, Langmuir 33 (2017) 9573–9581. https://doi.org/10.1021/acs.langmuir.7b01820.

[420] A. Stoffers, C. Oberdorfer, G. Schmitz, Controlled Field Evaporation of Fluorinated Self-Assembled Monolayers, Langmuir 28 (2012) 56–59. https://doi.org/10.1021/la204126x.

[421] K.A.K. Rusitzka, L.T. Stephenson, A. Szczepaniak, L. Gremer, D. Raabe, D. Willbold, B. Gault, A near atomic-scale view at the composition of amyloid-beta fibrils by atom probe tomography, Scientific Reports 8 (2018) 1–10. https://doi.org/10.1038/s41598-018-36110-y.

[422] S.C. Lam, R.J. Needs, Imaging atoms in the field-ion microscope: Tunneling calculations using realistic potentials, Physical Review B 48 (1993) 14698–14701. https://doi.org/10.1103/PhysRevB.48.14698.

[423] H.J. Kreuzer, Physics and chemistry in high electric fields, Surface and Interface Analysis 36 (2004) 372–379. https://doi.org/10.1002/sia.1985.

[424] S. Bhatt, S. Katnagallu, J. Neugebauer, C. Freysoldt, Accurate computation of chemical contrast in field ion microscopy, Phys. Rev. B 107 (2023) 235413. https://doi.org/10.1103/PhysRevB.107.235413.

[425] J.M. Cairney, K. Rajan, D. Haley, B. Gault, P.A.J. Bagot, P.-P. Choi, P.J. Felfer, S.P. Ringer, R.K.W. Marceau, M.P. Moody, Mining information from atom probe data, Ultramicroscopy 159 (2015) 324–337. https://doi.org/10.1016/j.ultramic.2015.05.006.

[426] G.B. Vincent, A.P. Proudian, J.D. Zimmerman, Three dimensional cluster analysis for atom probe tomography using Ripley's K-function and machine learning, Ultramicroscopy 220 (2021) 113151. https://doi.org/10.1016/j.ultramic.2020.113151.

[427] R.A. Bennett, A.P. Proudian, J.D. Zimmerman, Cluster characterization in atom probe tomography: Machine learning using multiple summary functions, Ultramicroscopy 247 (2023) 113687. https://doi.org/10.1016/j.ultramic.2023.113687.

[428] A. Saxena, N. Polin, N. Kusampudi, S. Katnagallu, L. Molina-Luna, O. Gutfleisch, B. Berkels, B. Gault, J. Neugebauer, C. Freysoldt, A Machine Learning Framework for Quantifying Chemical Segregation and Microstructural Features in Atom Probe Tomography Data, Microscopy and Microanalysis (2023) ozad086. https://doi.org/10.1093/micmic/ozad086.

[429] S. Srinivasan, K. Kaluskar, S. Dumpala, S. Broderick, K. Rajan, Automated voxelization of 3D atom probe data through kernel density estimation, Ultramicroscopy 159 (2015) 381–386. https://doi.org/10.1016/j.ultramic.2015.03.012.

[430] S. Samudrala, O. Wodo, S.K. Suram, S. Broderick, K. Rajan, B. Ganapathysubramanian, A graph-theoretic approach for characterization of precipitates from atom probe tomography data, Computational Materials Science 77 (2013) 335–342. https://doi.org/10.1016/j.commatsci.2013.04.038.

[431] S.R. Broderick, A. Bryden, S.K. Suram, K. Rajan, Data mining for isotope discrimination in atom probe tomography., Ultramicroscopy 132 (2013) 121–128. https://doi.org/10.1016/j.ultramic.2013.02.001.

[432] M.D. Wilkinson, M. Dumontier, Ij.J. Aalbersberg, G. Appleton, M. Axton, A. Baak, N. Blomberg, J.-W. Boiten, L.B. da Silva Santos, P.E. Bourne, J. Bouwman, A.J. Brookes, T. Clark, M. Crosas, I. Dillo, O. Dumon, S. Edmunds, C.T. Evelo, R. Finkers, A. Gonzalez-Beltran, A.J.G. Gray, P. Groth, C. Goble, J.S. Grethe, J. Heringa, P.A.C. 't Hoen, R. Hooft, T. Kuhn, R. Kok, J. Kok, S.J. Lusher, M.E. Martone, A. Mons, A.L. Packer, B. Persson, P. Rocca-Serra, M. Roos, R. van Schaik, S.-A. Sansone, E. Schultes, T. Sengstag, T. Slater, G. Strawn, M.A. Swertz, M. Thompson, J. van der Lei, E. van Mulligen, J. Velterop, A. Waagmeester, P. Wittenburg, K. Wolstencroft, J. Zhao, B. Mons, The FAIR Guiding Principles for scientific data management and stewardship, Sci Data 3 (2016) 160018. https://doi.org/10.1038/sdata.2016.18.